

---

*Probing Lipid Diffusion  
in Curved & Planar Membranes  
with Fluorescence Microscopy*

---

Dissertation for the award of the degree  
“Doctor rerum naturalium”  
of the Georg-August-Universität Göttingen  
within the doctoral program  
Physics of Biological and Complex Systems  
of the Göttingen Graduate School of Neurosciences,  
Biophysics, and Molecular Biosciences (GGNB)  
of the Georg-August-University School of Science (GAUSS)

submitted by  
Jan Thiart from Mettingen, Germany

Georg-August-Universität Göttingen  
Göttingen, June 2017



## **Members of the examination board:**

**Prof. Dr. Jörg Enderlein (Referee)**

III. Physikalisches Institut – Biophysik

Georg-August-Universität Göttingen

**Prof. Dr. Claudia Steinem (Co-referee)**

Institut für Organische und Biomolekulare Chemie

Georg-August-Universität Göttingen

**Dr. Jochen S. Hub**

Computational Molecular Biophysics Group

Department of Molecular Structural Biology

Georg-August-Universität Göttingen

**Prof. Dr. Stefan Klumpp**

Institut für Nichtlineare Dynamik

Georg-August-Universität Göttingen

**Dr. Florian Rehfeldt**

III. Physikalisches Institut – Biophysik

Georg-August-Universität Göttingen

**Prof. Dr. Fred Wouters**

Institut für Neuropathologie – Labor für molekulare und zelluläre Systeme

Universitätsmedizin Göttingen

Date of oral examination: 31<sup>st</sup> August 2017.

## Affidavit

Hereby, I declare that the presented thesis has been written independently and with no other sources and aids than quoted.

Parts of this thesis have been published in:

S. C. Stein and J. Thiart. 'TrackNTrace: A simple and extendable open-source framework for developing single-molecule localization and tracking algorithms'. *Scientific Reports* **6** (1) 2016 [1].

F. Savić, T.-T. Kliesch, S. Verbeek, C. Bao, J. Thiart, A. Kros, B. Geil and A. Janshoff. 'Geometry of the Contact Zone between Fused Membrane-Coated Beads Mimicking Cell-Cell Fusion'. *Biophysical Journal* **110** (10) 2016, pp. 2216–2228 [2].

The research leading to this thesis was supported with funding from the German Research Foundation (DFG) via the Collaborative Research Centre SFB 803 "Functionality controlled by organization in and between membranes" through project A10.

Göttingen, 23<sup>rd</sup> June 2017.



## ABSTRACT

Diffusion is the most important transport mechanism in biological membranes and essential for processes such as signalling or trafficking. Many different techniques have given insight into this matter, most of which are based on fluorescence microscopy. Applying these to synaptic vesicles or nanoscopic membrane domains, which are much smaller than the diffraction-limited resolution of a light microscope, is an ambitious task. In this thesis, two methods based on fluorescence correlation spectroscopy (FCS) are presented which circumvent the resolution limit and enable diffusion coefficient estimations in vesicles less than 200 nm in diameter. At this scale, the influence of membrane curvature on viscosity, diffusion speed, or lipid composition becomes dominant.

The first approach, dynamicMIET, exploits the interaction energy transfer of a fluorescent lipid in close proximity to a thin metal sheet. The resulting fluctuation in fluorescence intensity strongly depends on their distance to each other, which can in turn be obtained by FCS, making it possible to extract the membrane diffusion coefficient of a surface-tethered vesicle of arbitrary size. A robust and highly specific binding assay has been developed, but the organic dyes used for labelling were neither bright nor stable enough to obtain proper correlation curves. A detailed analysis revealed drastically increased dark state transitions and photo-bleaching of the lipid-conjugated dyes compared to their free counterparts.

The second technique is based on measuring the polarisation-resolved rotational diffusion of a fluorescent lipid within a vesicle bilayer. By fixing the dye-to-membrane orientation, rotational and translational diffusion components can be measured and extracted separately. A 3D diffusion model incorporating the vesicle size distribution fits the correlation curves very well, but the obtained diffusion coefficients are biased towards higher values, especially for larger liposomes. However, the fluorophore used in these experiments was found to have excellent photo-physical characteristics which could help to resolve the issues encountered in the dynamicMIET measurements.

To handle the data evaluation for many of the control experiments, I developed TrackNTrace, an open-source framework for fluorescence microscopy image analysis. TNT was originally designed as a localisation microscopy and particle tracking tool, but is extendible through a simple plugin system. It provides many state-of-the-art implementations of important algorithms and is aimed at novices as well as experienced researchers. An extensive visual feedback mechanism allows inspecting the program's output at all times, facilitating parameter optimisation and error recognition. These concepts were validated by comparing TrackNTrace against similar programs. The software has been a great help in analysing many of the experiments presented in this thesis and will hopefully turn out to be similarly beneficial for other scientists.

---

## Abbreviations and acronyms

BLM	Black lipid membrane
FCS	Fluorescence correlation spectroscopy
FRAP	Fluorescent recovery after photo-bleaching
FRET	Förster resonance energy transfer
GUV	Giant unilamellar vesicle
IMP	Integral membrane protein
MAP	Membrane-associated protein
MSD	Mean-squared displacement
SLB	Supported lipid bilayer
SPT	Single particle tracking
STED	Stimulated emission-depletion
STORM	Stochastic optical reconstruction microscopy
SUV	Small unilamellar vesicle
TNT	TrackNTrace
BPE	1,2-dioleoyl- <i>sn</i> -glycero-3-phosphoethanolamine-N-(biotinyl) salt
CCF	Cross-correlation function
DEPC <sub>18</sub>	1,2-dielaidoyl- <i>sn</i> -glycero-3-phosphocholine
DiD	1,1'-Dioctadecyl-3,3,3,3'-tetramethylindodicarbocyanine perchlorate
DLS	Dynamic light scattering
DPPE	1,2-dipalmitoyl- <i>sn</i> -glycero-3-phosphoethanolamine
MDF	Molecular detection function
MIET	Metal-induced energy transfer
NA	Numerical aperture
PBS	Phosphate buffered saline
PEG	Polyethylene glycol
PIE	Pulsed interleaved excitation
PSF	Point spread function
SPAD	Single-photon avalanche diode
TCSPC	Time-correlated single photon counting
cAMP	cyclic adenosine monophosphate
FRC	Fourier ring correlation
GAP	GTPase-activating proteins

---

GDP	Guanosine diphosphate
GEF	Guanine nucleotide exchange factors
GFP	Green fluorescent protein
GTP	Guanosine triphosphate
GUI	Graphical user interface
NNT	Nearest-neighbour tracking/tracker
SMLM	Single-molecule localisation microscopy
SNR	Signal-to-noise ratio
SOFI	Super-resolution optical fluctuation imaging
vbSPT	variational Bayes single particle tracking

# Contents

<b>1</b>	<b>Introduction</b>	<b>1</b>
1.1	Membrane structure & composition . . . . .	4
1.2	Artificial membranes . . . . .	7
1.3	Diffusion in lipid membranes . . . . .	10
1.4	Measuring lipid membrane diffusion with fluorescence microscopy . . . . .	12
<b>2</b>	<b>Diffusion measurements in vesicles</b>	<b>17</b>
2.1	Materials & Methods . . . . .	19
2.1.1	Fluorescence correlation spectroscopy (FCS) . . . . .	19
2.1.2	Dynamic metal-induced energy transfer (dynaMIET) . . . . .	22
2.1.3	Rotational diffusion . . . . .	26
2.1.4	Dynamic light scattering . . . . .	30
2.1.5	Chemicals & reagents . . . . .	30
2.1.6	Vesicle sample preparation . . . . .	31
2.1.7	Surface coating & vesicle immobilisation . . . . .	32
2.1.8	Experimental data acquisition & evaluation . . . . .	34
2.2	Results . . . . .	36
2.2.1	Preliminary experiments . . . . .	36
2.2.2	Dynamic MIET in small unilamellar vesicles . . . . .	39
2.2.3	Rotational diffusion of small unilamellar vesicles . . . . .	45
<b>3</b>	<b>TrackNTrace</b>	<b>53</b>
3.1	Materials & Methods . . . . .	55
3.1.1	Framework composition & plugin system . . . . .	55
3.1.2	Algorithms & developed plugins . . . . .	57
3.1.3	Performance evaluation . . . . .	66
3.1.4	Biological examples . . . . .	68
3.2	Results . . . . .	71
3.2.1	Performance evaluation . . . . .	71



3.2.2	Experimental examples . . . . .	73
3.3	Additional plugin development & experiments . . . . .	75
3.3.1	Diffusion on membrane-coated silica beads . . . . .	75
3.3.2	On-/off-state distribution in carbon nanodots . . . . .	76
3.3.3	Membrane signalling protein activation in <i>Dictyostelium discoideum</i> . . . . .	78
<b>4</b>	<b>Conclusion &amp; outlook</b>	<b>83</b>
	<b>Appendix A</b>	<b>86</b>
A.1	Additional figures and tables . . . . .	86
A.2	Rotational diffusion FCS functions . . . . .	88
	<b>List of Figures</b>	<b>91</b>
	<b>Bibliography</b>	<b>93</b>
	<b>Acknowledgements</b>	<b>105</b>
	<b>Curriculum vitæ</b>	<b>107</b>



# CHAPTER 1

## Introduction

The lipid membrane is a sheet-like barrier that separates biological compartments from their environment and organises into distinct functional domains according to its composition and surroundings. It envelopes virtually all living cells and viruses as well as organelles within a cell such as the nucleus or mitochondria, and encapsulates fluids in the form of vesicles which are then transported where needed [3–5].

Generally, it consists of a lipid bilayer and a variety of different proteins which fulfil a large number of fundamental tasks. They serve as anchors for a cell's actin and microtubule cytoskeleton [6] or form porous channels which regulate ion and water flux [7, 8]. Binding sites for antibodies, signalling proteins or other macromolecules form the basis of inter- and intra-cellular communication, trafficking, and sensing – processes which also involve (un-)binding and fusion of lipid vesicles [9–11]. For this delicate network of interactions to work, both lipids and proteins have to be able to move and react together in spite of the crowded environment they permeate. This is necessary for the formation of fusion pores [12], the oligomerisation of monomeric subunits [13], or for allowing structural changes of the cytoskeleton [14]. As directed transport is reserved to a smaller number of interactions, the most important mechanism of motion is diffusion. Therefore, characterising and quantifying lipid and protein diffusion in membranes is essential for understanding the biological processes they are involved in.

In 1975, Saffman and Delbrück published a membrane diffusion model describing proteins as large cylinders moving through a “sea of lipids” imagined as an infinitely wide, homogeneous plane [15]. Despite its simplicity, the model has been highly successful throughout the decades since its introduction and is still in wide use today [16]. However, there are some shortcomings which become relevant especially when moving from *in vitro* experiments with artificial membranes to biological samples. Functions to be maintained by real cell membranes differ greatly between their cytosolic and outer halves. They are asymmetrical and highly heterogeneous [17, 18], with typically several

dozen kinds of lipids and up to a thousand proteins in a simple *E.coli* prokaryote cell partitioned to the bilayer's two leaflets [19]. In addition to long-range forces initiated by binding partners on both sides of the membrane, these conditions make it difficult or even impossible to define diffusion model parameters which accurately describe the bilayer both locally and globally.

Another quality not accounted for in the Saffman-Delbrück-model (SD-model) is curvature. Undulations present in any membrane are restricted to the micrometre length scale and thus not relevant for the motion of a single lipid. In vesicles and fusion pores with diameters on the order of 10 nm however, the local particle density changes drastically between both leaflets or patches of lipids only a few molecules in length, thus making curvature the dominant influence on diffusion speed [20–23]. In the brain, for example, neurotransmitter carrying vesicles detach from the synaptic membrane of one neuron, traverse the synaptic cleft, and eventually fuse with the receiving neuron's membrane. This fusion process is mediated by so-called SNARE proteins responsible for membrane disruption, bending, and reorganisation [24, 25]. How do proteins and lipids operate in such a highly curved environment? What influence does such a high curvature have on their molecular interactions and distribution within the membrane? While theoretical calculations and molecular dynamics simulations have given some insight into this matter [26–28], experimental verification is scarce as the size of such vesicles, usually about 30 nm, is well below the resolution of typical microscopes which is fundamentally limited by diffraction to about 200 nm. Super-resolution fluorescence microscopy techniques such as stochastic optical reconstruction microscopy (STORM [29]), photo-activated localisation microscopy (PALM [30]), and stimulated emission-depletion (STED [31]) microscopy have pushed far beyond this boundary, but are still constrained by their low temporal resolution [32]. Dynamic processes such as diffusion, which occur at the sub-ms scale, require different techniques. Nuclear magnetic resonance (NMR) spectroscopy is one such method and has been employed to obtain membrane diffusion coefficients from vesicles in solution since the early 1970s [33]. Unfortunately, the large sample concentrations or measurement times required by an NMR experiment limit its applicability in scenarios where biological samples can only be purified in small amounts, are difficult to stabilise, or require unique labelling strategies.

In this thesis, I introduce two novel methods based on fluorescence correlation spectroscopy (FCS) which are capable of measuring diffusion coefficients in small unilamellar vesicles (SUV). With diameters between 50 nm and 200 nm, they are comparable in size to synaptic vesicles and thus a perfect model system for highly curved bilayers. The first approach exploits the interaction of a fluorescent dye with a thin metal sheet leading to an energy transfer between the two. The resulting fluctuation in fluores-

---

cence intensity strongly depends on their distance to each other, which can in turn be obtained by FCS. This makes it possible to extract the membrane diffusion coefficient of a metal-surface-tethered vesicle containing dye-tagged lipids. The second technique is based on the realisation that the movement of a fluorescently labelled molecule in the bilayer of a freely diffusing vesicle can be decomposed into vesicle rotation and bilayer diffusion components. If the vesicle radius is known, which is simple to measure, the rotational part can be subtracted. Although both procedures were initially designed to study membrane motion, the great temporal resolution of FCS could be used to study any kind of fast dynamic process.

Furthermore, I am presenting TrackNTrace (TNT), an open-source program for fluorescence imaging data analysis. Parts of TNT were initiated as a side project to complement fluorescence imaging measurements necessary for control experiments. It was eventually developed into a fully featured software suite together with my colleague Simon Christoph Stein. TNT takes a different approach than most other applications in this field in that it combines a simple but versatile user interface and visualisation mechanism with a powerful and highly flexible plugin add-on system. The visualiser allows quick inspections of preview results and greatly facilitates parameter adjustment that way. Being programmed in MATLAB, which is especially popular in the life sciences, TrackNTrace allows for easy modification of existing and development of new routines. Although originally conceived as a single-molecule particle tracking (SPT) tool to study membrane diffusion, it is also equipped for localisation microscopy, defocused imaging, drift correction, image filtering, and related procedures.

The following introductory chapter will give an overview of the membrane model systems employed in this work and explore the physics of lipid diffusion which serve as the foundation of this research.

## 1.1 Membrane structure & composition

The concept of biological membranes as a bilayer made up of lipids and proteins was fully conceived for the first time by Singer and Nicolson [3] based on decades of research started in the early 20th century. Although this so-called fluid mosaic model has been gradually revised over time [4, 14, 34], it remains largely intact and continues to be in use today. At the model's core, the lipid bilayer is described as a two-dimensional fluid which can exist in either a solid, gel-like phase or as a disordered, viscous liquid made up of lipids. In this picture, proteins are regarded as associated or inserted units which define the membrane's function with respect to its environment and the degree of compartmentalisation necessary to fulfil this role. The bilayer's physical characteristics – such as thickness, phase, viscosity, polarity, curvature, or bending rigidity – are primarily defined by its lipid make-up.

Common to all membranes is the ability to self-assemble in solution owing to the amphiphilic nature of all lipids. The hydrophilic headgroups are exposed to the aqueous solvent, keeping the hydrophobic fatty acid residue backbone free from water, thus minimising the entropic forces. The bilayer's structure and composition are highly diverse: Lipids differ by number of residues, chain length, number and form (cis/trans) of double bonds – the degree of unsaturation – headgroup type and charge, or polarity. Fig. 1.1 gives a broad overview of the different classes.

Mammalian cellular membranes consist of approximately 65% glycerophospholipids and up to 10% sphingolipids, with sterols, mainly cholesterol, accounting for the remaining percentage [35]. The distribution can vary by orders of magnitude even within a single cell as an organelle such as the endoplasmic reticulum requires a very different lipid composition than the nucleus, the mitochondria, or the Golgi apparatus.

The same principle also holds for the two leaflets of each bilayer which can be highly asymmetric in terms of their lipid content. Cells need to recruit different proteins on the cytoplasmic and the outer-leaflet side, requiring contrasting malleability, viscosity, or adhesiveness. Curvature can be non-existent in the outer leaflet while the inner one maintains a negative curvature [36], which is possible due to the vast size and shape differences of lipids. Phosphatidylcholine (PC) and phosphatidylethanolamine (PE) molecules, the most abundant sub-classes of phospholipids in eukaryotes, for example, are distinctly cylindrical and cone-shaped, respectively [37]. Despite this diversity, total lipid concentration and membrane thickness are relatively homogeneous across different cells and their compartments. With a hydrophobic tail length of roughly 1.5 nm to 2.0 nm and a headgroup area of 0.25 nm<sup>2</sup> to 1.0 nm<sup>2</sup>, a 1 μm<sup>2</sup> membrane patch typically reaches a thickness of 4 nm to 5 nm and contains several million lipids [35, 38].

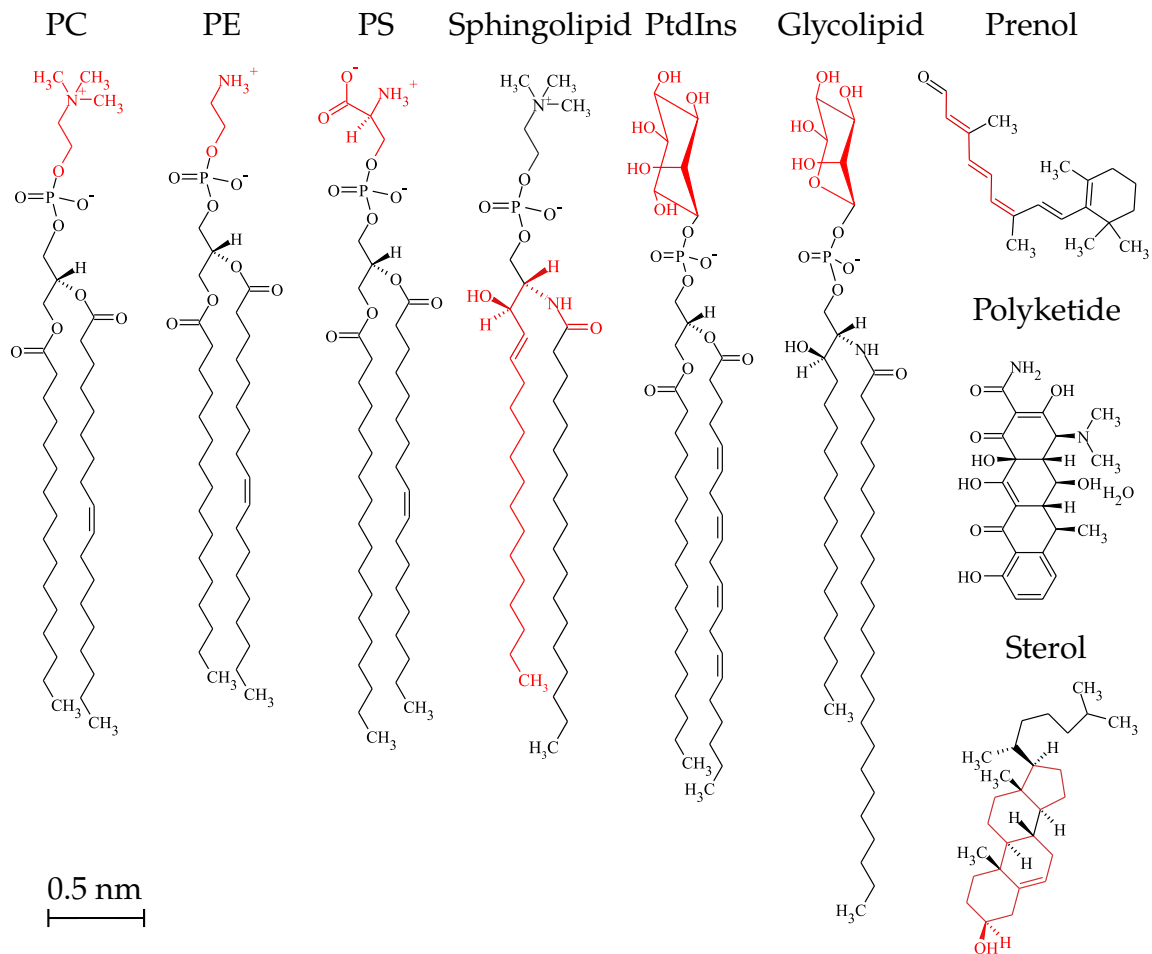


**Figure 1.1:** Categories of cellular membrane lipids (examples): Phosphatidylcholine (POPC), Phosphatidylethanolamine (POPE), Phosphatidylserine (Brain-PS), Phosphosphingolipid (Sphingomyelin), Phosphatidylinositol (Liver-PI), Glycolipid (Glyco-Cer(d18:1/22:0)), Prenol (Vitamin A), Polyketide (Doxycyclin), and Sterol (Cholesterol). The suffix-giving functional group is highlighted in red. Adapted and extended from [39].

Providing a unified view of a typical cell bilayer becomes even more complicated when membrane proteins are included into the picture. Two classes of proteins are defined based on their proximity to the membrane and their significance to its make-up. The most important type is the integral membrane protein (IMP) which is permanently bound to the bilayer. IMPs not only perform the most crucial tasks necessary for the survival of the cell, they can also associate with certain types of lipids, forming micro-domains in the process, and are essential to the preservation of the bilayer's structure. Examples of integral proteins include ion channels, signal receptors, adhesion molecules, or proteases. Most but not all IMPs are transmembrane proteins containing a globular main unit connected to one or several  $\alpha$ -helices which span across the whole height of the bilayer in a loop-like fashion.

Extrinsic, or peripheral membrane proteins are either weakly linked to the lipid bilayer or frequently attach and re-attach as is the case with signalling proteins. They are closely associated with the membrane but can nevertheless be removed from it without disturbing the bilayer's integrity or the stability of any other micro-domains such as the ones formed by IMPs. Tethering and scaffolding, curvature inducement, as well as enzyme regulation are typical functions executed by these proteins. As they are not permanently bound to one of the leaflets, they do not share a common structure, although many possess either lipid binding sites or fatty acid residues for brief insertion [40].

Some authors define a third class, the membrane associated proteins (MAP), composed of cytoskeletal anchors, glycoproteins, and similar molecules. Although important, and in some cases essential for cell regulation, MAPs usually couple to other membrane proteins and do not directly interact with the membrane at all, therefore having far less influence on the bilayer's dynamics.

The complex network of interactions between lipids, proteins, cytoskeleton, and extracellular objects naturally restricts the mobility of all membrane constituents in many different ways. Aside from direct coupling to the intra- and extracellular matrix, the most significant modification of the fluid mosaic model in terms of diffusive confinement is the discovery of micro- and nano-domains [14, 41]. A large portion of lipids and transmembrane proteins are suspected to partition into clusters either by mutual attraction or confinement by membrane-associated anchors. Within these patches, fluidity is lowered and molecules can become contained by oligomerised obstacles, temporarily fenced off, or immobilised altogether. While the exact size, survival time, and origin of these corral meshes and lipid rafts is still hotly debated, no other concept has been advanced in the same way to explain all the different experimental evidence gathered in the last decades [42].

Fig. 1.2 tries to give an overview of a typical cellular membrane, depicting some of the microscopic assembly which was previously described. Apart from the micromolecular composition of the membrane, the most important influence on structure and diffusivity is the temperature which determines the liquid phase. At low temperatures  $\ll 0^\circ\text{C}$ , the bilayer assumes a solid, lamellar crystalline phase  $L_c$  which transforms into a highly viscous gel phase  $L_\beta$  upon heating. After passing a certain temperature threshold  $T_m$ ,  $L_\beta$  undergoes a melting transition into the liquid-crystalline – or liquid-disordered –  $L_{\alpha,d}$  phase, the most relevant one in biological systems. Here, the membrane behaves like a viscous fluid ( $\eta_m \sim 10^2 \text{ mPa} \cdot \text{s}$ ) and lipids can freely diffuse within the bilayer.  $T_m$  increases with chain length due to the larger van-der-Waals forces, and with the degree of trans-unsaturation which causes denser chain packing. Depending on the lipid mixture, intermediate phases such as a tilted or rippled  $L_\beta$  gel can also occur. Cholesterol is a key player in this regard as it inserts into the membrane in between the head-



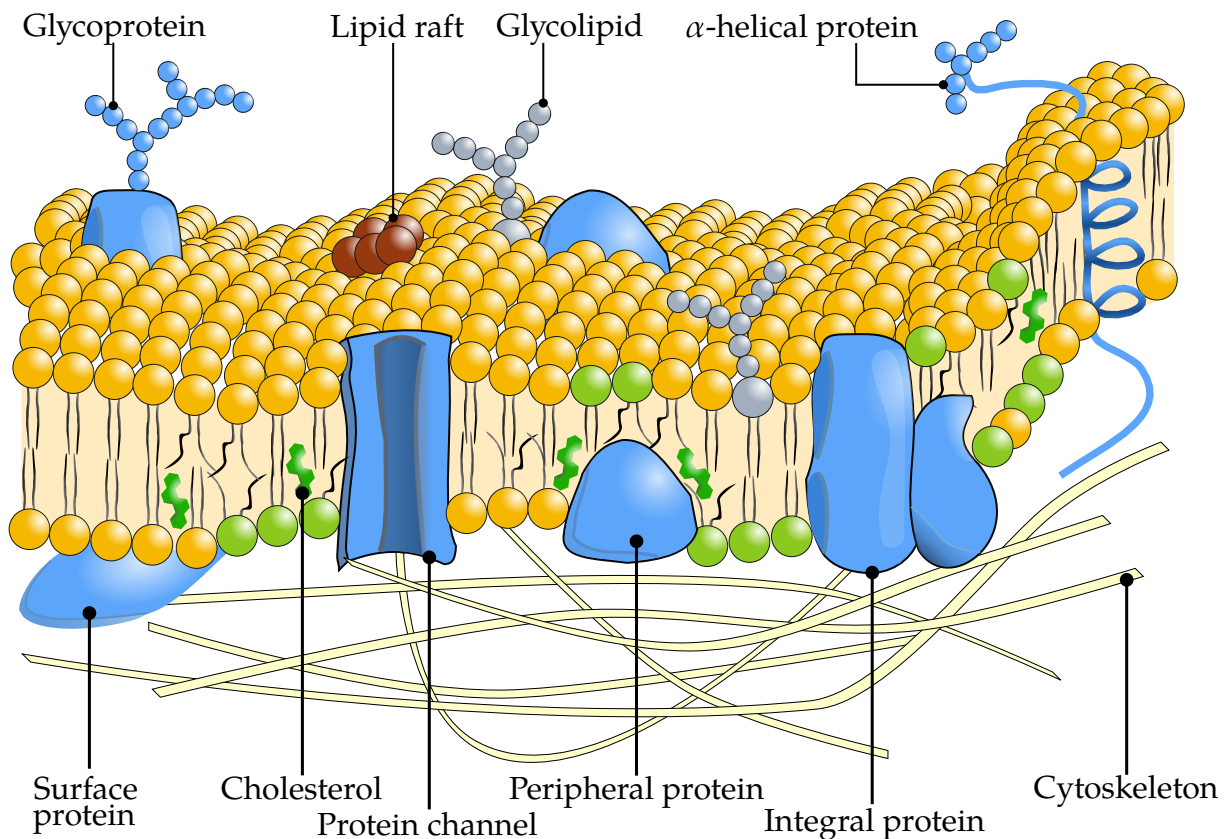


**Figure 1.2:** Model view of cellular membrane with major intra- and extracellular matrix components.

groups, thereby decreasing the fluidity in most cases. The so-called liquid-ordered  $L_o$  phase produced in this manner is immiscible with liquid-disordered bilayers, making researchers suspecting cholesterol to be the main element in lipid rafts [43, 44].

In summary, the cellular membrane is a very complex object produced and maintained by a vast array of interconnected reactions and forces. Isolating a particular property such as the local curvature and studying its relation to the network of dynamics is a very challenging task. For this reason, model bilayer systems are employed in this work instead.

## 1.2 Artificial membranes

*In vitro* membrane experiments are less cumbersome to set up, highly reproducible, and allow direct manipulation of important control parameters such as lipid mixture, viscosity, membrane phase, or curvature [45]. The most commonly employed model system in this scenario is the supported lipid bilayer (SLB). SLBs are formed by spreading lipid vesicles onto a glass substrate or slowly dragging the substrate through an aqueous solution with a lipid monolayer on top. The planar membrane created this

way is stable, highly resistant to shear flow, and can be studied with invasive probing experiments such as atomic force microscopy. While not completely flat due to substrate defects causing bilayer deformation, SLBs are immobile and do not undulate, an important requirement for some fluorescence and scattering microscopy techniques sensitive to movements along the optical axis. The SLBs' close proximity to the surface, while useful in some scenarios, is also its biggest disadvantage. Membrane-substrate interactions lead to a decrease in diffusion speed by a factor of  $\sim 10$  compared to free-standing bilayers. As the majority of membrane proteins span the whole bilayer's height, their function can be significantly perturbed by surface coupling. Although passivation schemes such as polymer cushioning can alleviate these issues to some degree, care must be taken when interpreting and comparing results gained solely from SLB experiments [46].

Free-standing bilayers, also called black lipid membranes (BLM), could be regarded as a counterpart to SLBs. BLMs are typically created by flushing solubilised lipids through an aperture submerged in an appropriate buffer solution. The hydrophobic solvent partitions to the edge of the polymer aperture, leaving behind a spontaneously formed, single lipid bilayer. BLMs are much less stable than SLBs and susceptible to undulation, but are not hindered by any interactions with their surroundings, with the exception of the solvent annulus [47]. Both fluid channels above and below the bilayer are independently accessible, enabling straightforward protein incorporation as well as electroporation experiments or asymmetric labelling. Instead of using one single, larger aperture, BLMs can also be created by spreading a lipid film on a functionalised micropore array chip. The free-standing bilayers painted over the micropore cavities are solvent-free, less prone to rupture, and can therefore be more easily manipulated. Hundreds of pores can be imaged at the same time in a multiplexing fashion [48].

The third important asset of a membrane experimentalist's toolbox are unilamellar vesicles. Vesicles can be fabricated in sizes ranging from  $10^1$  nm (SUVs) to  $10^2$   $\mu$ m (giant unilamellar vesicle, GUV), either mimicking the various types of cellular liposomes or the planar cell membrane itself. GUVs are created by electroformation; a lipid film is deposited on an electrode surface, rehydrated, and topped off by another electrode before applying a sinusoidal current. The film swells, single lamellae are budding off and eventually cleaved into solution. The finished GUVs can be collected and later tethered to a surface to avoid drift during data acquisition [49]. GUVs provide inexpensive, interaction-free planar membranes and do not require any organic solvents or elaborate equipment as is the case with BLMs. Owing to their nearly spherical shape, GUV bilayers can be probed in a polarisation-dependent manner and are particularly suited for the study of lipid mixtures. Their stability is comparatively high, facilitating protein incorporation and permitting experiments involving high amounts of mechanic stress, e.g. optical tweezer studies. Their only significant drawback is the difficulty of exchan-

ging the buffer without causing major osmotic stress, formation of pores, and collapse. However, this property can also be exploited to fine-tune the inclusion of transmembrane proteins [50]. In this thesis, GUVs are utilised as solvent- and interaction-free planar membranes for control measurements.

The main model system used here are SUVs. SUVs are synthesised by lipid extrusion or sonication, both of which start from a rehydrated lipid film vigorously shaken to form multilamellar vesicles. The lamellae are then sheared off by flushing the solution through a polycarbonate membrane or disrupting them with ultrasound. Both processes yield unilamellar vesicles with a narrow size distribution ( $\sigma_d \sim 15$  nm) around a mean diameter of 30 nm to 200 nm [51]. This is also the size range where the largest changes in diffusive speed due to increasing curvature are expected, making SUVs the ideal study object for this thesis. Apart from serving as an *in vitro* imitation of cellular liposomes such as synaptic vesicles, SUVs are essential for membrane fusion assays and mainly employed as a protective environment to be used for protein incorporation or drug delivery. Care must be taken when handling SUVs near a surface instead of in solution as they quickly adsorb to and spread on both hydrophilic and hydrophobic substrates, creating an SLB in the process. If the surface is mostly passivated and then functionalised at low density, vesicles can be anchored and used to study single-molecule events, as can be seen in chapter 2.

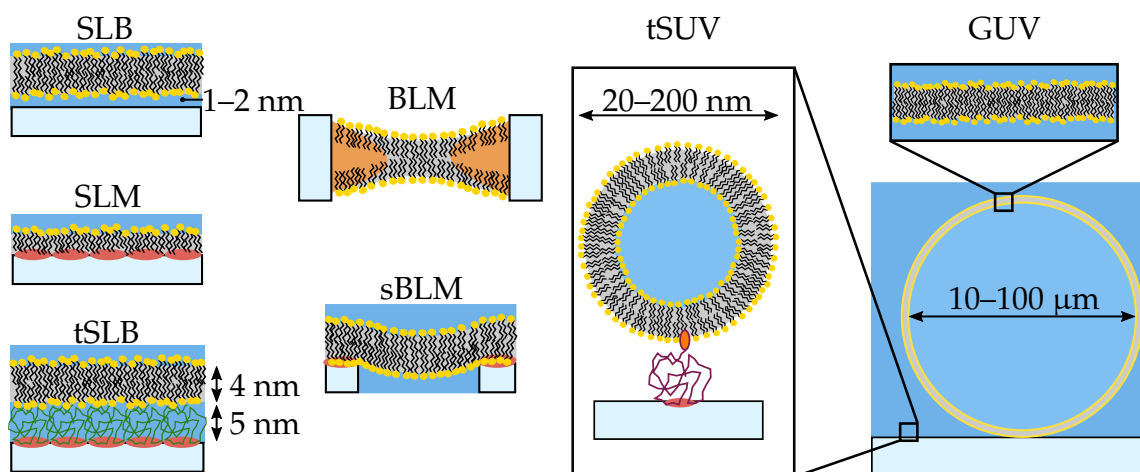


**Figure 1.3:** Common membrane model systems: Supported lipid bilayer (SLB), supported lipid monolayer (SLM), tethered/cushioned SLB (tSLB), black lipid membrane (BLM), tethered/supported BLM (sBLM), small unilamellar vesicle (SUV), giant unilamellar vesicle (GUV).

A higher degree of control over the physical characteristics of model membranes and their reduced complexity with respect to cell membranes make it easier to understand the dynamics within these sophisticated biological structures. This allows us to

describe, model, and measure the diffusive behaviour of fluorescent probes within a lipid bilayer, as laid out in the next section.

### 1.3 Diffusion in lipid membranes

Diffusion typically describes the random movement of a molecule or atom within a surrounding fluid due to collisions with the medium's particles caused by thermal motion. Also known as Brownian motion named after its discoverer, diffusion can be described by a probabilistic differential equation,

$$\frac{\partial}{\partial t} p(\mathbf{r}, t) = D \underline{\Delta} p(\mathbf{r}, t) \quad , \quad (1.1)$$

with the Laplace operator  $\underline{\Delta} = \partial^2/\partial x^2 + \partial^2/\partial y^2 + \partial^2/\partial z^2$  and the diffusion coefficient  $D$  which is given by the Einstein relation

$$D = \mu k_B T \quad . \quad (1.2)$$

A special case of the fluctuation dissipation theorem, it relates the amplitude of the random thermal impact force to the dissipative friction caused by hydrodynamic drag. In solution, a spherical particle experiencing conventional Stokes drag with mobility  $\mu = 1/(6\pi\eta R)$  has a diffusion coefficient of

$$D = \frac{k_B T}{6\pi\eta R} \quad , \quad (1.3)$$

with dynamic viscosity  $\eta$ , temperature  $T$ , Boltzmann coefficient  $k_B$  and particle radius  $R$  [52]. The thermal motion observed in a lipid bilayer is more difficult to quantify: The target particles are constrained to two-dimensional movement in a highly viscous sheet while experiencing a traction force from the outside liquid which is usually much more fluid. Saffman and Delbrück first predicted a logarithmic dependence on the particle radius, giving

$$D = \frac{1}{4\pi\eta_m h} \left( \log \left( \frac{\eta_m h}{\eta R} \right) - \gamma_E \right) \quad , \quad (1.4)$$

where  $h$  is the bilayer height,  $\eta_m$  the membrane viscosity<sup>1</sup>, and  $\gamma_E$  the Euler-Mascheroni constant [15]. The model is valid for smaller inclusions having  $2R\eta/(\eta_m h) = R/l_{SD} \ll 1$  which is the case for nanometre-sized lipids and proteins. The Saffman-Delbrück length  $l_{SD}$  is the characteristic length scale where the 2D-like hydrodynamical approximation begins to break down.

---

<sup>1</sup>Some authors denote  $\eta' = \eta_m h$  as the membrane viscosity, usually in units of cP · nm.

In the case of larger inclusions, and especially in highly curved membranes, lipid-protein height mismatch, lipid chain stretching, and in-plane viscous stress can drastically alter the diffusion speed further. Experiments on tethered bilayer cylinders have proven that curvature not only slows down the bulk diffusion but also leads to lipid and protein sorting [22]. Depending on charge, size, or chain unsaturation, cone- and cylinder-shaped lipids will associate into patches of different curvature as well as raft-like nanodomains in the case of lipid mixtures [53]. For spherical bilayers, i.e. vesicles, an analytical expression for the hydrodynamic drag in the limit of high curvature  $R\eta/(\eta_m h) = R/l_c \ll 1$  was given by Henle and Levine [54]:

$$D = \frac{k_B T}{4\pi\eta_m h} \left( \log\left(\frac{R}{a}\right) - \frac{11}{12} \right) \quad (1.5)$$

Here,  $R$  and  $a$  are the radii of the vesicle and the membrane inclusion, respectively, and  $l_c$  is analogous to the previously mentioned SD-length. Notably, the diffusion still scales logarithmically with the inclusion size but is now solely determined by the bilayer's fluidity; instead of contributing to the particle diffusion itself, an outside traction force leads to a rotation of the vesicle as a whole. As it turns out, this rotation is energetically favourable compared to a deformation of the inclusion-associated membrane patch within the highly strained bilayer. Cancelling out the rotation term in a co-rotating frame of reference then leads to eq. (1.5).

Assuming a lower limit of  $10^2 \text{ mPa} \cdot \text{s}$  for  $\eta_m$  in the  $L_d$ -phase, a buffer viscosity of  $1 \text{ mPa} \cdot \text{s}$ , and a membrane height of  $4 \text{ nm}$  [55], the cutoff radius  $R_{\text{cut}}/l_c \sim 0.3$  above which the model begins to break down is  $R_{\text{cut}} \sim 120 \text{ nm}$ . Thus, curvature studies in this thesis are limited to SUVs and LUVs with  $R \leq 100 \text{ nm}$ . In another simplification, the membrane viscosity  $\eta_m$  is approximated as constant. In small vesicles, this will certainly not be the case as the lipid-packing density is radius-dependent and differs between the compressed inner and the more disordered outer monolayer. This behaviour has only recently been explored by molecular dynamics simulations [56], however, and has not been verified experimentally.

Evidently, curvature is a very important property and its influence is assumed to be especially relevant in the case of vesicle budding, docking, and fusion, as has been mentioned already. A thorough treatment based on accurate and precise measurements is absolutely vital for the understanding of these physiological processes. However, experimental evidence is scarce and almost exclusively drawn from nuclear magnetic resonance studies [57] which are expensive, require rather high sample concentrations, and suffer from poor temporal resolution and precision. For this reason, fluorescence microscopy is presented as a viable alternative.

## 1.4 Measuring lipid membrane diffusion with fluorescence microscopy

To observe the motion of membrane lipids or proteins and estimate their diffusion speed, these molecules obviously have to be detected or visualised first. Fluorescence microscopy is the foremost choice in this regard [58–60]. In fluorescence microscopy, an object of interest is labelled with a chromophore which can be excited by the light of a laser or arc lamp. After absorbing a photon of wavelength  $\lambda_{\text{abs}}$ , and spending a certain time  $\tau_F \sim 10^0$  ns in an excited state, another photon is emitted at a wavelength  $\lambda_{\text{em}} > \lambda_{\text{abs}}$ . The energy loss resulting from vibrational relaxations, the so-called Stokes-shift, makes it possible to separate and filter excitation and emission light. Since the first detection of single fluorescent molecules at room temperature almost 30 years ago [61], technological advances in filter quality, camera sensitivity and speed, laser excitation, chromophore design, and labelling efficiency have helped fluorescence microscopy to an unprecedented level of contrast and specificity unmatched by any other imaging technique. Three principal methods have established themselves over the years to determine diffusion coefficients in biological samples: Fluorescence recovery after photobleaching (FRAP, [62]), the aforementioned single particle tracking [63, 64], and fluorescence correlation spectroscopy.

The basic idea behind FRAP is very simple: Instead of imaging diffusing fluorescent probes directly, the time it takes for fluorophores to fill a previously depleted area is measured. In practice, a second laser beam with a defined but smaller excitation area and very high intensity is used to bleach all fluorophores in a region of known size. The original laser beam excites the complete field of view throughout the experiment and a camera records the remaining fluorophores diffusing into the bleached spot. The fluorescence recovery rate can be fitted with an appropriate model to extract the diffusion coefficient. FRAP works well in two-dimensional, densely labelled, homogeneous systems if the fluorescence recovery is diffusion-limited and the bleaching is instantaneous. These pre-requisites are usually met for synthetic planar bilayers but quickly break down when transitioning to slightly more complex systems. Axial motion in three-dimensional environments is difficult to account for, as is diffusion out of the region of interest during bleaching. In the presence of several diffusing species or at faster diffusion speeds, FRAP curve fitting becomes unreliable. While the bleaching spot can be reduced down to the diffraction limit in theory, determining the fluorescence recovery in such a case is much less accurate. Thus, FRAP is essentially an ensemble-averaging technique without single-molecule sensitivity or high spatial resolution. As both covalent fluorescent labelling itself and the high labelling density required in these

## 1.4. Measuring lipid membrane diffusion with fluorescence microscopy

experiments negatively impact lipid diffusion [65], the method's applicability to more delicate membrane structures is debatable. A similar argument can also be made against the influence of the bleaching pulse on the sample. Combined with FRAP's inability to determine diffusion coefficients in sub-diffraction-sized objects like SUVs, it is clear that such an approach is unsuitable for the type of study conducted in this work.

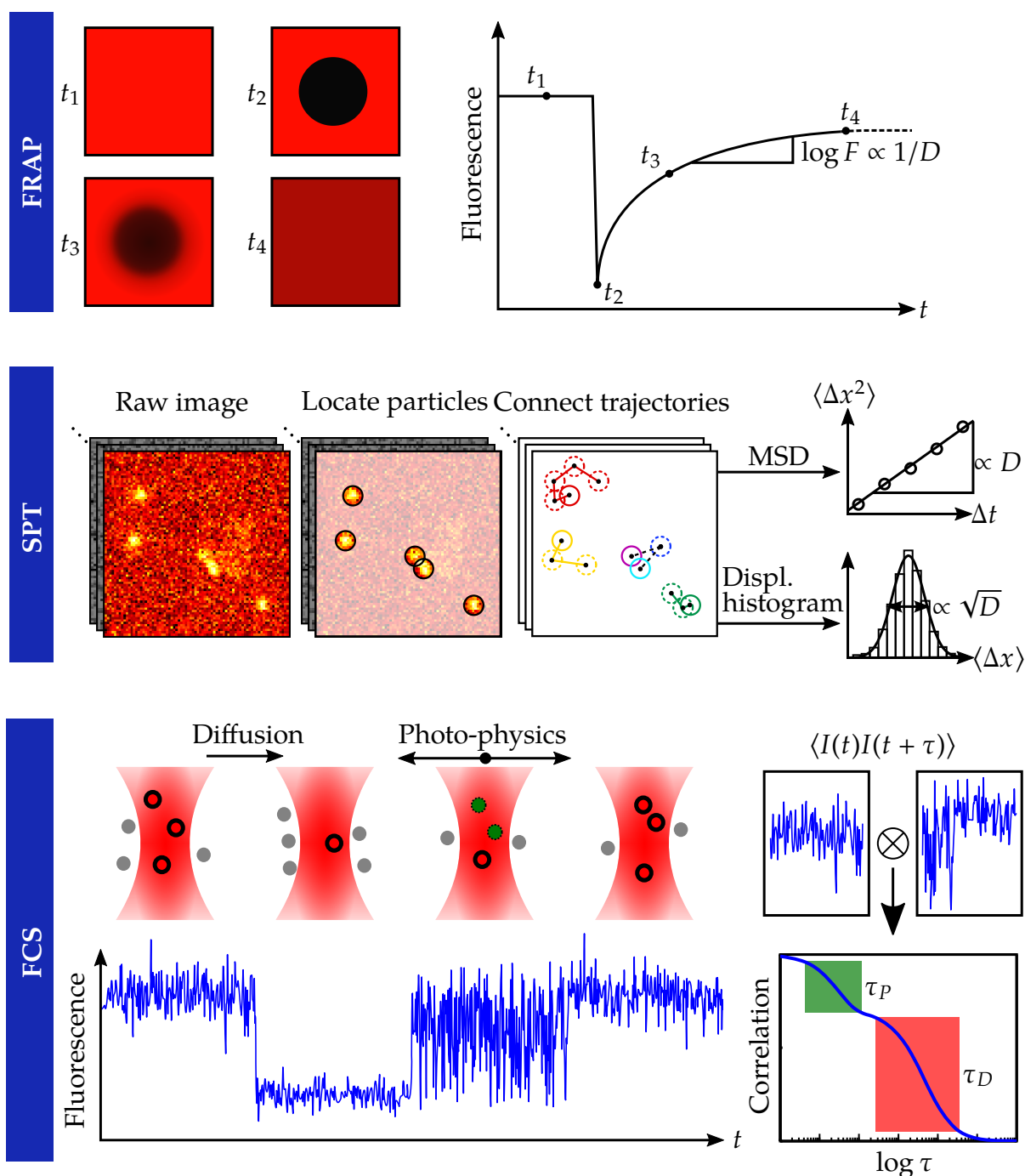


**Figure 1.4:** Fluorescence microscopy methods for diffusion measurements. From top to bottom: Fluorescence recovery after photo-bleaching (FRAP), single particle tracking (SPT), and fluorescence correlation spectroscopy (FCS).

Single particle tracking on the other hand is capable of both ensemble averaging and single-molecule sensitivity based on the experimenter's preferences. Here, single fluorescently labelled molecules are recorded while diffusing through solution. The resulting movie is analysed by localising the particles in all frames and subsequently linking these positions in time to form trajectories. These trajectories represent the random walks the probes undergo, where the size of the cleared area after a certain time  $t$  – the mean-squared displacement (MSD) – is  $2Dt \cdot d$ ,  $d$  being the dimensionality. The MSD can be calculated for one single molecule or for all of them together, meaning that SPT can reveal the averaged dynamics of a whole system or just one small part of it. As the centre of a fluorophore's image can be determined with much higher accuracy than its width, a fact exploited to great success in single-molecule localisation microscopy, SPT can achieve a very high spatial accuracy given sufficient signal quality. Instead of imaging emitters in a fixed field of view, particles can also be actively tracked [66] which allows following molecules for minutes and is especially beneficial in live-cell experiments. The capacity of SPT to directly image changes in kinetics at the single-molecule level without needing to model or cross-check them using different methods has led to the discovery of non-Brownian motion and non-ergodicity [67] in complex biological systems, specifically the cell membrane.

The main limitations of particle tracking are sample concentration and temporal resolution. At densities  $\gtrsim 1 \mu\text{m}^{-2}$ , orders of magnitude below physiological conditions, algorithms used to link particle positions in time begin to break down, making careful labelling strategies essential or prohibiting the use of SPT altogether. Furthermore, although SPT could in principle be used to resolve molecular motion within diffraction-limited structures such as SUVs, this would necessitate integrating the signal for longer durations, making the sub-millisecond time domain inaccessible. For the study of lipid diffusion in planar membranes such as GUVs, however, particle tracking is an excellent tool and is extensively used for control experiments in this thesis.

Whereas both FRAP and SPT are, in the most general sense, imaging-based techniques, fluorescence correlation spectroscopy extracts information from the temporal dynamics of a fluorescence signal. In FCS, a laser beam is focused on the sample, typically in solution, and the fluorescence intensity  $I(t)$  is recorded with picosecond accuracy using a single-photon counting detector. The signal is then correlated in time to measure how fast the fluorescence signal fluctuates which is related to the time-scale of the underlying physical processes:

$$g(\tau) = \langle I(t)I(t + \tau) \rangle_t \quad (1.6)$$

The correlation function  $g$  denotes the probability of detecting photons at times  $t$  and  $t + \tau$  from the same molecule. It contains information about any spatial and temporal dy-



namics encoded in the fluorescence intensity fluctuation. These include concentration changes due to diffusion in and out of the focus, photo-physical transitions, chemical reactions, aggregation, or energy transfer events such as Förster resonance energy transfer (FRET) [68–72]. While FCS can be performed on a single emitter, correlation curves are typically obtained from an ensemble average over many signal sources. In the optimal case, a diffraction-limited focus should contain only one molecule in a femtolitre-sized volume which makes fluorescence correlation spectroscopy ideal for dealing with concentrations closer to physiological values. As a result of the tremendous temporal resolution, an FCS experiment can give access to a large range of parameters in the period of a single measurement. Simultaneously determining the diffusion coefficient, folding time, and binding or unbinding rates of a protein is a typical example of this, provided the time-scales do not overlap completely. Additionally, the picosecond to nanosecond regime informs about fluorescence lifetime, dipole orientation, or photon antibunching, among other properties. Fluorescence lifetime imaging (FLIM [73]) and rotational anisotropy [74] are two prominent applications based on such measurements.

Although a versatile technique, FCS does have weaknesses. Most importantly, the size and shape of the excitation and detection volumes have to be precisely known to correctly model and quantify the relationship between intensity fluctuations and spatial changes. Careful calibration is paramount to reduce the margin of error, but only modified FCS methods such as two-focus FCS (2f-FCS [75]) or scanning FCS [76] possessing an in-built calibration standard can succeed in this regard. Similar to FRAP, the diffraction-limited focal size imposes a lower limit on the achievable spatial resolution. For a near-infrared dye and a high-numerical-aperture (NA) objective, the diffraction-limited point spread function (PSF) size is roughly 300 nm. While methods such as STED-FCS [77] mitigate this issue to some degree, resolving the diffusion dynamics within a 30 nm liposome is still out of reach. In the following chapter, two new FCS techniques are introduced which circumvent most of these problems and enable diffusion measurements in sub-diffraction-sized vesicles.



## Diffusion measurements in vesicles

When performing fluorescence spectroscopy experiments on sub-diffraction-sized samples, there are two strategies to circumvent the resolution limit if a manipulation of the PSF has already been ruled out. One is to have the fluorescence intensity fluctuation depend on principles other than the location within the excitation volume, the other is to use the magnificent temporal resolution of FCS. These same principles also apply to the methods introduced in this thesis.

The first technique exploits the fluorescence lifetime change of a dye in close proximity to a metal surface due to energy transfer between excited molecule and surface plasmons. This so-called metal-induced energy transfer (MIET [78, 79]) leads to a decrease of the fluorescence lifetime which monotonically depends on the distance of the fluorophore to the surface. Single-molecule studies by Karedla et al. [80] have shown that a lifetime-to-distance conversion can be realised to nanometre accuracy. As it is not possible to make such a “lifetime snapshot” of a lipid dye at the temporal resolution required for diffusion measurements, the fluorescence intensity can be used instead of the lifetime, as both are related by a simple linear transform. The experiment is realized by recording intensity traces from several surface-bound, labelled SUVs and calculating their individual correlation functions according to (1.6). By averaging over all vesicles to achieve sufficient statistics, the diffusion coefficient can be determined from the decay curves which represent the axial fluorophore movement resulting from the spherical surface diffusion. The complete particle dynamics are recovered in the process and the technique is dubbed dynamic MIET, or dynaMIET for short.

The second method uses rotational diffusion FCS measurements of SUVs in solution. A fluorescent label attached to a lipid molecule in such a vesicle could itself rotate, co-diffuse with its binding partner, and co-rotate with the entire vesicle lab-frame. The first mechanism happens on a completely different time-scale while the latter two are not discernible due to the diffraction limit. The situation changes if the fluorophore’s

orientation with respect to the bilayer is fixed, i.e. by using a lipophilic dye such as BODIPY. Though the vesicle rotation remains the same, the dye rotation is now directly coupled to the lateral diffusion, all of which take place in the  $\mu\text{s}$ -range. By measuring the total rotational diffusion with FCS and determining the vesicle radius, the translational component can be extracted by simply subtracting the lab frame rotational component.

Before showing the outcome of both approaches, the chapter will begin by laying out the theory behind them.

## 2.1 Materials & Methods

### 2.1.1 Fluorescence correlation spectroscopy (FCS)

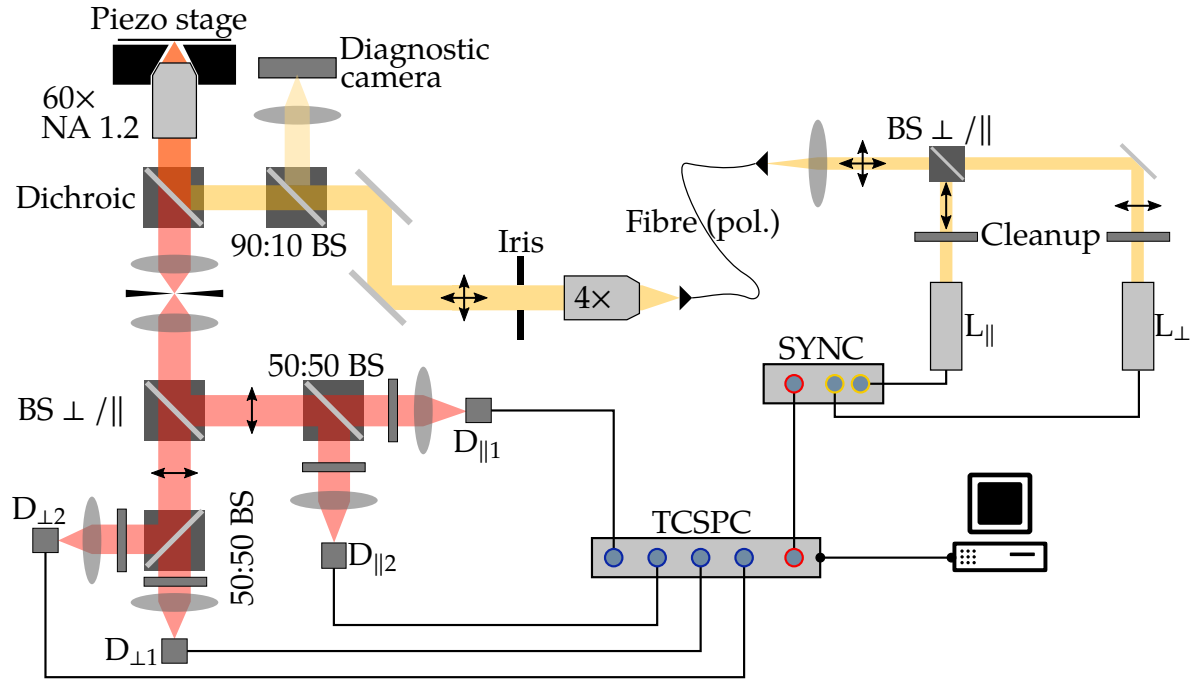


**Figure 2.1:** Schematic of the Microtime 200 setup. The two linearly polarised, pulsed diode lasers (pulse length 50 ps,  $\lambda_{\text{ex}} = 640$  nm) are rotated  $90^\circ$  with respect to each other, combined with a polarising beam splitter and coupled into a polarisation-maintaining fibre. They are operated in pulsed-interleaved-excitation mode (PIE) at a repetition rate of 40 MHz per pulse. After collimation, the beam can be narrowed with an iris aperture to expand the focus in the sample plane and is then reflected by a dichroic mirror (FITC/TRITC, *Chroma Technology, USA*) onto the objective which uses either water (UPLSAPO 60 $\times$  NA 1.2) or oil (UAPON 100 $\times$  NA 1.49, both *Olympus, Germany*) as an immersion medium. The latter is only used for surface measurements which also depend on a piezo-electric  $xyz$ -scanning stage from *Physik Instrumente GmbH, Germany*. The back-reflection of the coverslip surface is imaged onto a CCD camera (FC-25C, *Ganz, USA*) for alignment purposes.

The emission light is collected, directed through the dichroic mirror, and focused onto a pinhole aperture 150  $\mu\text{m}$  in diameter. After collimation with a second lens, the emission light is split either by a 50/50 non-polarising or a polarising beam splitter and collected by two sets of one or two detectors (two  $\tau$ -SPAD and two SPCM-AQR-13, *PerkinElmer Optoelectronics, Germany*). In the latter case, the beam is split again with a 50/50 splitter. Each SPAD is equipped with a 679/41 emission filter (BrightLine HC, *AHF, Germany*). The signals are recorded with a HydraHarp 400 module connected to the main unit which also controls the Sepia II module responsible for laser operation. All parts and hardware are provided by *PicoQuant GmbH, Germany* if not mentioned otherwise.

The setup used in this thesis for all FCS experiments is built on top of a standard confocal microscope attached to a commercial MicroTime 200 FCS system as pictured in fig. 2.1. The excitation unit is composed of two collimated, linearly polarised, pulsed diode lasers coupled into a polarisation-maintaining fibre. Their light is reflected by a quad-band dichroic mirror onto the back-focal-plane of a water-immersion objective with an NA of 1.2, creating an ideal, diffraction-limited focus in the sample plane with a dimension of roughly  $(0.5 \mu\text{m})^2 \times 2 \mu\text{m}$ . Collected by the same objective, the emission light is transmitted through the dichroic and focused onto a pinhole which cuts off out-of-plane light, greatly reducing background fluorescence. After collimation, the beam is either focused onto a single-photon avalanche diode (SPAD), or directed through multiple beam splitters to several SPADs operating in tandem.

The SPADs are connected to a photon-counting unit which records the arrival time of every detected photon in time-tagged, time-resolved mode. Here, the SPADs are synced to the laser pulses and both the time of excitation, and the time between an incoming signal and the next pulse is recorded with picosecond accuracy. Before further processing, these arrival times can be binned to create a time-correlated single photon counting (TCSPC) histogram as detailed in fig. 2.2 from which the fluorescence lifetime  $\tau_F$  can be extracted, among other variables.

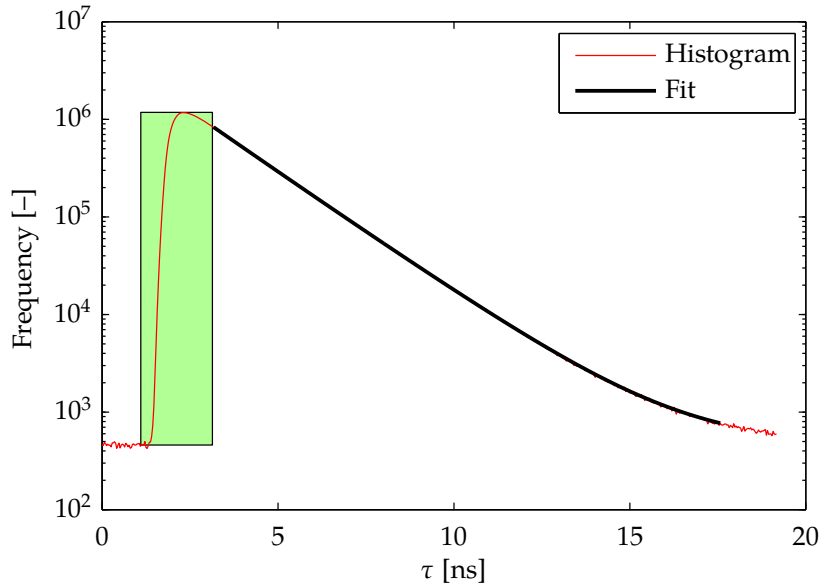


**Figure 2.2:** Exemplary TCSPC histogram of Atto655 in PBS. The complete histogram is a convolution of the exponential fluorescence decay curve, including background, and the instrument response function (IRF) which has a FWHM of typically 200 ps. An exponential tail fit excluding the IRF region (shaded) gives a fluorescence lifetime of  $\tau_F = 1.78(2)$  ns.

In conventional FCS, only one laser and SPAD are employed which reduces the available correlation functions to one as stated in eq. (1.6). This auto-correlation function,

however, always contains artefacts related to the detector hardware. The electronics can falsely report an additional photon resulting from spurious charge following an actual event and, in rare cases, the silicon chips themselves are excited by the incident light which is later re-emitted in the form of fluorescence or phosphorescence. These effects are known as after-pulsing and after-glow, respectively, and cause an artificial correlation spike in the (sub-) $\mu\text{s}$ -domain. While both can be mitigated through careful data analysis and use of proper emission filters, electronic dead-times on the order of  $10^{2..3}$  ns ultimately limit such an ordinary FCS setup to the study of slow-moving molecules.

For this reason, modern FCS systems use at least two detectors, enabling the calculation of cross-correlations (CCF)

$$g_{\alpha\beta}(\tau) = \langle I_{\alpha}(t)I_{\beta}(t + \tau) \rangle_t \quad , \quad (2.1)$$

where  $\alpha$  and  $\beta$  denote the detector index. After-pulsing is an entirely independent, uncorrelated noise source and thus vanishes from the CCF and the dead-time issue is resolved completely.

In such a configuration, FCS can be used to investigate the diffusion of small fluorophores ( $D \approx 400 \mu\text{m}^2 \text{s}^{-1}$ ) [75] or fast photo-physical processes like singlet-triplet inter-system crossing ( $\tau_T \approx 10^0 \mu\text{s}$ ) and cis-trans isomerisation ( $\tau_C \approx 10^2$  ns) [81]. However, this is only valid as long as the intensity fluctuation is solely dependent on properties inherent to the molecule of interest. In rotational diffusion or FRET experiments, changes in fluorescence intensity are related to excitation polarisation or wavelength which depend on the laser. It is therefore necessary to record traces for multiple laser sources at the same time. The simplest way of doing this is pulsed interleaved excitation (PIE). Here, all  $n$  laser sources are pulsed one after the other, reducing the original repetition or cycling rate  $f_0$  to  $f_{\text{PIE}} = f_0/n$ . If  $f_0$  is chosen so that  $f_{\text{PIE}}^{-1} \gg \tau_F$ , the fluorescence intensity will have decayed almost completely before the next laser pulse arrives. This makes it possible to associate each photon with its respective excitation source via time-gating, as seen in fig. 2.3.

The full correlation function is then given as

$$g_{\alpha\beta}^{\gamma\delta}(\tau) = \langle I_{\alpha}^{\gamma}(t)I_{\beta}^{\delta}(t + \tau) \rangle_t \quad , \quad (2.2)$$

denoting the laser pulses with  $\gamma$  and  $\delta$ . With  $n_l$  lasers and  $n_d$  detectors, a total of  $(n_l \times n_d)^2$  correlation functions can be calculated,  $2n_l n_d$  of which are ACFs and therefore not used. Extracting all relevant parameters  $\mathbf{M}$  from the CCFs requires developing a theoretical model for all fluorescence transitions of each molecular species present. For a single molecule,  $g$  would represent the probability  $U(\theta')$  of detecting the molecule

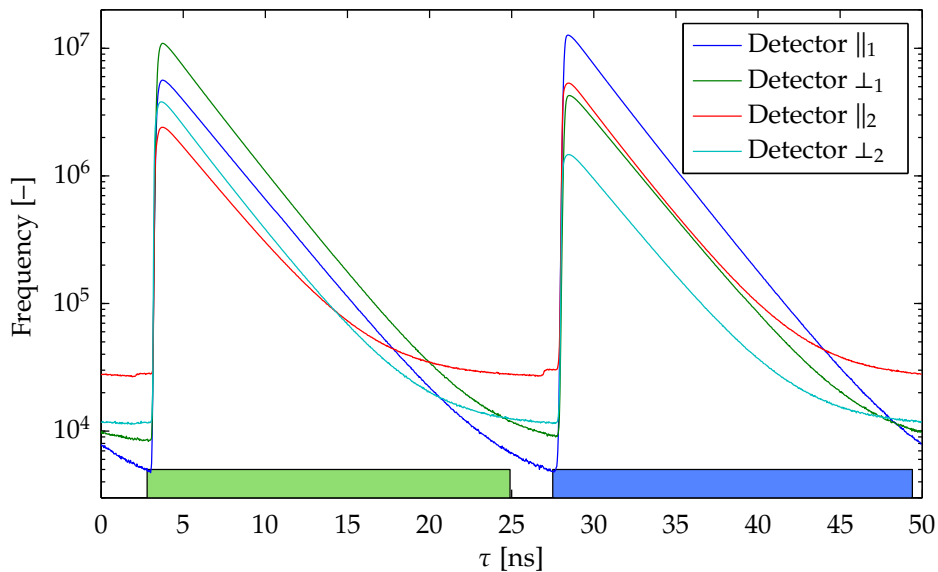


**Figure 2.3:** Pulsed interleaved excitation scheme. After calculating the TCSPC histogram for a rotational diffusion experiment, time gates for each pulse (green and blue shade) can be set automatically and every photon is attributed to a laser-detector pair according to its time channel. In this instance, detectors  $\parallel_1$  and  $\parallel_2$  show a higher signal for the second laser pulse, which has a parallel polarisation, as they lie in the parallel detection path.

in a state  $\theta'$ , multiplied by the probability  $G(\mathbf{M}, \theta', \theta)$  to transition to another state  $\theta$ , and finally the possibility of detecting it in said state. While FCS is essentially a single-molecule technique, one usually averages over an ensemble of all  $N$  molecules within the detection volume  $V$ , expressed by a volume integral over all possible states:

$$g_{\alpha\beta}^{\gamma\delta}(\tau, \mathbf{M}) = g(\infty) + c \int_V d\theta \int_V d\theta' \varepsilon_{\beta}^{\delta} U_{\beta}^{\delta}(\theta) \cdot G(\mathbf{M}, \theta', \theta, \tau) \cdot \varepsilon_{\alpha}^{\gamma} U_{\alpha}^{\gamma}(\theta') \quad (2.3)$$

$c$  is the concentration  $N/V$  and  $\varepsilon$  is a measure for the molecular brightness and detection efficiency.  $U(\theta_i)$  is also known as the molecular detection function (MDF) and  $G$  is typically Green's function for the general Fokker-Planck equation in the case of diffusion. The exact correlation models relevant to this work are laid out in the subsequent sections.

### 2.1.2 Dynamic metal-induced energy transfer (dynaMIET)

A direct application of MIET to FCS for lipid diffusion measurements in vesicles is a challenging task. In addition to translational and rotational diffusion of the vesicle, and spherical diffusion of the fluorophore inside the bilayer, energy transfer in proximity to the surface has to be taken into account. As the energy transfer depends both on the fluorophore's axial distance to the surface and its orientation, an analytical expression of (2.3) is difficult to obtain without a few important approximations.



First, the vesicles investigated here are roughly 30 nm to 100 nm in diameter. In this range, the relative change in fluorescence lifetime due to MIET can be well expressed by a linear function as seen in fig 2.4. As the vesicles are much smaller than the PSF both laterally and axially and are anchored to the coverslip, the excitation intensity is constant. All fluorescence fluctuations therefore depend solely on the distance between fluorophore and surface. Second, while the orientation of the lipid anchor within the bilayer is fixed, the fluorophore can rotate freely and does so on a time-scale much faster than the diffusion. Hence, neither the detection efficiency nor the MIET efficiency relate to the dipole orientation. Thus, the task of determining the CCF for dynaMIET in surface-anchored SUVs is reduced to finding Green's function for the axial component of a spherically diffusing particle.

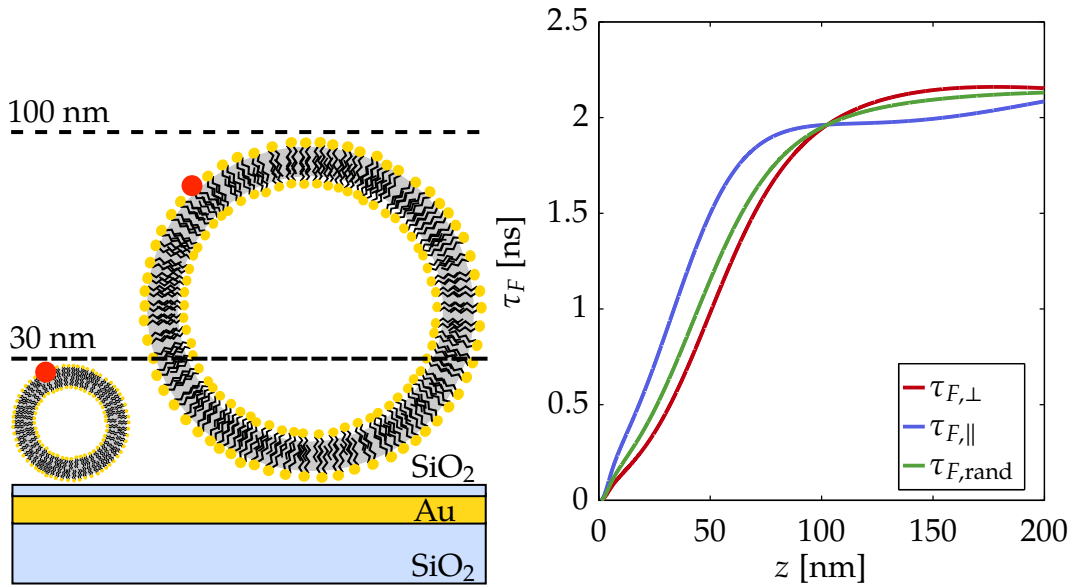


**Figure 2.4:** DynaMIET scheme for SUVs and fluorescence lifetime calibration curve. The silica spacer height can be adjusted such that the complete bilayer shell is still within the linear regime of the fluorescence intensity curve. For the calibration curves, a fluorophore with lifetime  $\tau_F = 2$  ns, quantum yield  $\Phi = 0.7$ , and emission wavelength  $\lambda_{em} = 670$  nm is considered, the Au thickness is 10 nm.

Let us start from the advection-free three-dimensional diffusion equation:

$$\frac{\partial}{\partial t} p(\mathbf{r}, t) = D \left( \frac{\partial^2}{\partial x^2} + \frac{\partial^2}{\partial y^2} + \frac{\partial^2}{\partial z^2} \right) p(\mathbf{r}, t) = D \underline{\Delta} p(\mathbf{r}, t) \quad , \quad (2.4)$$

where  $p(\mathbf{r}, t)$  is the probability density of finding the particle at position  $\mathbf{r}$  at a time  $t$  and  $D$  is the isotropic, time-independent diffusion coefficient. Transforming to spherical coordinates  $(r, \varphi, \theta)$  and keeping the vesicle radius  $r = R$  constant, one finds:

$$\left[ \frac{1}{\sin \theta} \frac{\partial}{\partial \theta} \left( \sin \theta \frac{\partial}{\partial \theta} \right) + \frac{1}{\sin^2 \theta} \frac{\partial^2}{\partial \varphi^2} \right] p(\varphi, \theta, t) = \underline{\Delta}_s p(\varphi, \theta, t) = \frac{R^2}{D} \frac{\partial}{\partial t} p(\varphi, \theta, t) \quad (2.5)$$

Using a product ansatz  $p(\varphi, \theta, t) = \Phi(\varphi, \theta)T(t)$ , the solution can be easily expressed in terms of the Laplace operator's eigenfunctions in spherical coordinates, the spherical harmonics  $Y_l^m$ :

$$\underline{\Delta}_S Y_l^m(\varphi, \theta) = -l(l+1)Y_l^m(\varphi, \theta) \quad \text{with} \quad (2.6)$$

$$Y_l^m(\varphi, \theta) = \sqrt{\frac{2l+1}{4\pi} \frac{(l-m)!}{(l+m)!}} P_l^m(\cos \theta) \exp(im\varphi)$$

$$P_l^m(x) = \frac{(-1)^m}{2^l l!} (1-x^2)^{m/2} \frac{d^{l+m}}{dx^{l+m}} (x^2-1)^l$$

$P_l^m$  are associated Legendre polynomials. In this new basis,  $p(\varphi, \theta, t)$  is expressed as

$$p(\varphi, \theta, t) = \sum_{l=0}^{\infty} \sum_{|m| \leq l} a_l^m(t) Y_l^m(\varphi, \theta) \quad , \quad (2.7)$$

and the time-dependent coefficients  $a_l^m(t)$  can be obtained by separation of variables,

$$a_l^m(t) = b_l^m(t_0) \exp(-l(l+1)qt) \quad , \quad (2.8)$$

so that

$$p(\varphi, \theta, t) = \sum_{l=0}^{\infty} \sum_{|m| \leq l} b_l^m(t_0) \exp(-l(l+1)qt) Y_l^m(\varphi, \theta) \quad , \quad (2.9)$$

where the abbreviation  $q = DR^{-2}$  was used. At  $t_0 = 0$ , the start of the particle's random walk,  $p$  should be  $\delta$ -distributed, that is,

$$\begin{aligned} p(\varphi, \theta, 0) &= \delta(\varphi - \varphi', \theta - \theta') \\ &= \sum_{l=0}^{\infty} \sum_{|m| \leq l} Y_l^{m*}(\varphi', \theta') Y_l^m(\varphi, \theta) \end{aligned} \quad (2.10)$$

The second identity follows from the fact that spherical harmonics form a complete orthonormal basis in Hilbert space. Inserting into eq. (2.9) and comparing coefficients for  $t = 0$ , one finally finds

$$p(\varphi, \theta, t) = \sum_{l=0}^{\infty} \sum_{|m| \leq l} \exp(-l(l+1)qt) Y_l^{m*}(\varphi', \theta') Y_l^m(\varphi, \theta) \quad . \quad (2.11)$$

With this result, the dynaMIET correlation curve can be calculated by inserting eq. (2.11) into eq. (2.3) and integrating over all possible angles  $\mathbf{\Omega} = (\varphi, \theta)$  and  $\mathbf{\Omega}'$ . As excitation and detection intensity scale with the axial dimension only, the MDFs can be expressed as  $\varepsilon_i R(1 + \cos \theta_i)$  up to a constant factor  $\varepsilon_i$ . We thus obtain:

$$\begin{aligned} g(\tau) &= R^2 \int d\mathbf{\Omega} \varepsilon_2(1 + \cos \theta) \int d\mathbf{\Omega}' \varepsilon_1(1 + \cos \theta') \times \\ &\quad \sum_{l=0}^{\infty} \sum_{|m| \leq l} Y_l^{m*}(\mathbf{\Omega}') Y_l^m(\mathbf{\Omega}) \exp(-l(l+1)q\tau) \end{aligned} \quad (2.12)$$

By exploiting the fact that  $1 + \cos \theta = \sqrt{4\pi} Y_0^0(\Omega) + \sqrt{4\pi/3} Y_1^0(\Omega)$ , a real function, the integrals are easy to carry out due to the orthonormality criterion

$$\int d\Omega Y_l^{m*} Y_{l'}^{m'} = \delta_{mm'} \delta_{ll'} \quad , \quad (2.13)$$

which leads to

$$g(\tau) = \varepsilon_1 \varepsilon_2 R^2 \sum_{l=0}^{\infty} \sum_{|m| \leq l} (4\pi \delta_{m0} \delta_{l0} + 4\pi/3 \delta_{m0} \delta_{l1}) \exp(-l(l+1)q\tau) \quad , \quad (2.14)$$

and subsequently

$$\begin{aligned} g(\tau) &= 4\pi R^2 \varepsilon_1 \varepsilon_2 \left( 1 + \frac{1}{3} \exp(-1 \cdot (1+1)q\tau) \right) \\ &= 4\pi R^2 \varepsilon_1 \varepsilon_2 \left( 1 + \frac{1}{3} \exp\left(-\frac{2D\tau}{R^2}\right) \right) \quad . \end{aligned} \quad (2.15)$$

This remarkably simple result tells us that the lipid diffusion in a spherical layer will lead to a single exponential decay in the correlation curve which scales with the square of the vesicle radius. Fig. 2.5 shows a theoretical plot for typical ranges of diffusion constants and radii. With the radius measured in a different experiment, the diffusion constant can be extracted directly as  $D_{\text{exp}} = R_{\text{exp}}^2 / (2\tau_{\text{fit}})$ .

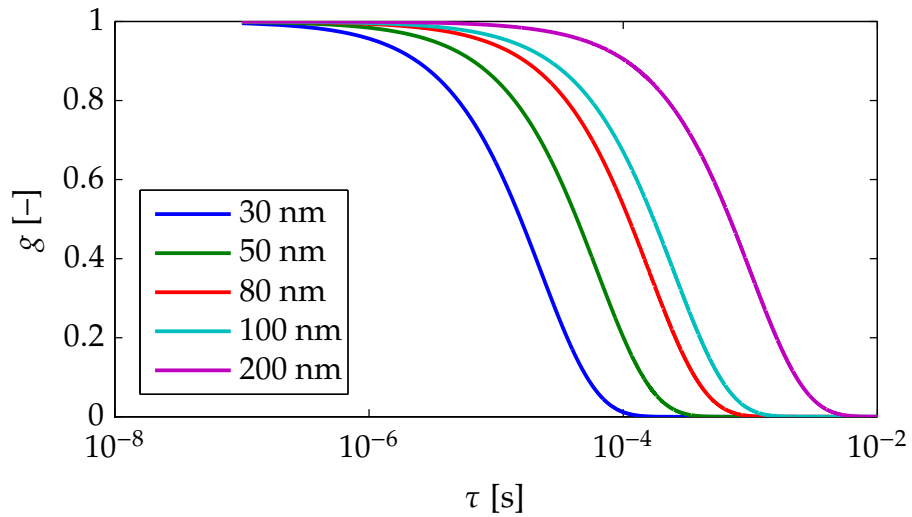


**Figure 2.5:** Theoretical dynaMIET correlation curves for spherical diffusion (normalised) for different radii.

### 2.1.3 Rotational diffusion

In a dynaMIET experiment, the vesicles can neither rotate nor diffuse, and the fast rotation of the fluorophore can be disregarded compared to the slower lipid diffusion. For a freely diffusing vesicle, all of these mechanics have to be taken into account both in finding Green's function and in calculating the MDFs due to the polarisation-dependent detection.

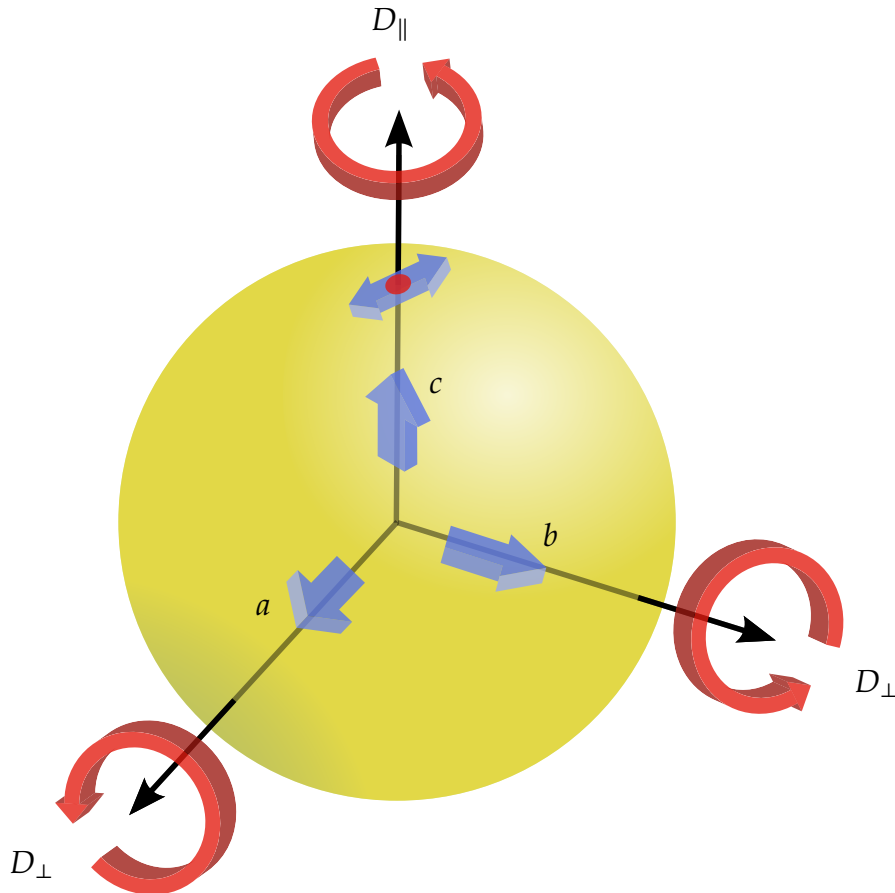


**Figure 2.6:** Complete rotational diffusion of a fluorophore within a vesicle bilayer. The fluorophore's dipole axis is tangential to the vesicle surface and can rotate with rotational diffusion coefficient  $D_{\parallel}$ . Perpendicular to this axis, the fluorophore's motion is a linear combination of translational diffusion of the fluorophore through the bilayer and rotational diffusion of the vesicle as a whole denoted by  $D_{\perp}$ .

If the vesicle is illuminated in the axial direction with a plane wave, the electric field vectors are oriented in the  $xy$ -plane ( $ab$ -plane in vesicle rest frame) parallel to the equatorial plane. Thus, for two opposite spots at the equator, the field vectors are exactly perpendicular to the dipole axis and the fluorophore cannot be excited.

Consider a completely spherical, dye-tagged vesicle as depicted in fig 2.6 which is excited by a linearly polarised laser. The fluorophore is inserted tangentially with its dipole axis oriented parallel to the bilayer surface. Assuming complete orthogonality between molecular rotation and dipole axis, three diffusion modes are present in the

vesicle's rest frame  $\mathbf{r} = (a, b, c)$ : A fast motion representing in-plane rotation of the fluorophore perpendicular to the dipole axis, and two slower components which stem from lipid diffusion and rotation of the whole vesicle. The latter two are indistinguishable and both add to a compound diffusion component around the axes  $a$  and  $b$ , respectively. This symmetric-top rotor can be described analogous to eq. (2.4), following earlier derivations for rotating proteins in solution [81]:

$$\frac{\partial}{\partial t} p = - (D_{\perp} \hat{J}_a^2 + D_{\perp} \hat{J}_b^2 + D_{\parallel} \hat{J}_c^2) p \quad , \quad (2.16)$$

where  $a, b$ , and  $c$  denote the principal axes of rotation,  $\hat{J}_i$  are their angular momentum operators,  $p = p(\varphi, \theta, \psi)$  is the probability density of finding the molecule rotated by Euler's angles  $\varphi, \theta$ , and  $\psi$  with respect to the lab frame, and  $D_{\perp}$  and  $D_{\parallel}$  are the rotational diffusion coefficients<sup>1</sup>. It is assumed here that the electric field travels along the axial direction  $c$  and is polarised along  $a$  and  $b$ . To simplify matters, one can express  $p$  in terms of the lab frame coordinates, that is

$$p(\varphi, \theta, \psi) = \hat{R} |l, m\rangle = R_z(\varphi) R_y(\theta) R_z(\psi) |l, m\rangle \quad . \quad (2.17)$$

$R_i$  are Cartesian rotation matrices using the  $z$ - $y$ - $z$  convention and  $|l, m\rangle$  are eigenfunctions of the angular momentum operator obeying the following relations:

$$\hat{\mathbf{J}}^2 |l, m\rangle = l(l+1) |l, m\rangle \quad (2.18)$$

$$\hat{J}_z |l, m\rangle = m |l, m\rangle \quad (2.19)$$

Inserting into eq. (2.16) yields

$$\frac{\partial}{\partial t} \hat{R} |l, m\rangle = -\hat{R} [D_{\perp} (\hat{\mathbf{J}}^2 - \hat{J}_z^2) + D_{\parallel} \hat{J}_z^2] |l, m\rangle \quad (2.20)$$

$$= - [D_{\perp} (l(l+1) - m^2) + D_{\parallel} m^2] \hat{R} |l, m\rangle \quad . \quad (2.21)$$

The transformed eigenfunctions  $\hat{R} |l, m\rangle$  are Wigner rotation matrices defined by:

$$D_{km}^l(\varphi, \theta, \psi) = \langle l, k | \hat{R}(\varphi, \theta, \psi) | l, m \rangle = \exp(ik\varphi + im\psi) d_{km}^l(\theta) \quad \text{with} \quad (2.22)$$

$$d_{km}^l(\theta) = \langle l, k | R_y(\theta) | l, m \rangle = \frac{\sqrt{(l+k)!(l-k)!(l+m)!(l-m)!}}{k!} \times \sum_n \frac{(-1)^{l+k-n} [\cos(\theta/2)]^{2n-m-k} [\sin(\theta/2)]^{2l+m+k-2n}}{(l+m-n)!(l+k-n)!(n-m-k)!} \quad (2.23)$$

They are closely associated with the spherical harmonics introduced in the last section, forming an orthogonal basis represented by the relation

$$\int_0^{\pi} d\theta \sin \theta \int_0^{2\pi} d\varphi \int_0^{2\pi} d\psi D_{km}^l{}^*(\varphi, \theta, \psi) D_{k'm'}^l(\varphi, \theta, \psi) = \frac{8\pi^2}{2l+1} \delta_{ll'} \delta_{kk'} \delta_{mm'} \quad . \quad (2.24)$$

<sup>1</sup>Note that the signs of eqn. (2.16) and (2.18) are reversed w.r.t. the previous section in accordance with the quantum mechanical definition of angular momentum used in this derivation.

As shown in the previous section, applying  $\langle l, k |$  to eq. (2.21), solving for  $t$ , and comparing coefficients for  $t = 0$ , returns Green's function. In this case, it represents the probability that a molecule has rotated from its initial orientation  $\mathbf{\Omega}' = (\varphi', \theta', \psi')$  to a new orientation  $\mathbf{\Omega}$  during a time  $t$ , given as

$$G(\mathbf{\Omega}, \mathbf{\Omega}', t) = \sum_{l=0}^{\infty} \sum_{|m|, |k| \leq l} \frac{2l+1}{8\pi^2} \exp(-\lambda_m^l t) D_{km}^l(\mathbf{\Omega}) D_{km}^{l*}(\mathbf{\Omega}') \quad , \quad (2.25)$$

where  $\lambda_m^l = D_{\perp} l(l+1) + (D_{\parallel} - D_{\perp}) m^2$ .

To calculate the MDFs  $U_i$ , the dipole orientation is the most important quantity to consider. In the vesicle lab frame, the symmetric-top rotor's dipole axis  $\mathbf{v}'$  is always parallel to the surface. After a rotation by Euler's angles, the new orientation will be

$$\mathbf{v} = R_z(\varphi) R_y(\theta) R_z(\psi) \mathbf{v}' \quad . \quad (2.26)$$

The dipole is excited by two lasers which are linearly polarised along the  $x$ - and  $y$ -direction, subsequently denoted  $\parallel$  and  $\perp$ . If depolarisation effects of the high-NA objective are neglected,  $U_{\text{exc}}$  can be expressed as

$$U_{\parallel}(\varphi, \theta, \psi) = \varepsilon_1 v_x^2, \quad U_{\perp}(\varphi, \theta, \psi) = \varepsilon_2 v_y^2 \quad , \quad (2.27)$$

assuming the vesicles are much smaller than the PSF volume and the vesicle translational diffusion is much slower than its rotation speed. In good approximation, emission and detection dipoles are co-linear, and the same definitions hold for the detection MDFs, with  $\varepsilon_1$  and  $\varepsilon_2$  being proportionality constants.

Equations (2.25) and (2.27) are sufficient to calculate the full two-photon polarisation-resolved correlation curve  $g_{\alpha\beta}^{\gamma\delta}$  for detection channels  $\alpha, \beta$  and excitation pulses  $\gamma, \delta$  for the first and the second photon, respectively. For a single event, the probability of exciting the molecule with pulse  $\gamma$  in orientation  $\mathbf{\Omega}'$ , letting it rotate into a new orientation  $\mathbf{\Omega}$  after time  $t$ , and detecting a photon in channel  $\alpha$  after the same time is given by

$$Q_{\alpha}^{\gamma}(\mathbf{\Omega}) = U_{\alpha}(\mathbf{\Omega}) \int_0^{\infty} dt \int d\mathbf{\Omega}' p(t) G(\mathbf{\Omega}, \mathbf{\Omega}', t) U_{\gamma}(\mathbf{\Omega}') \quad . \quad (2.28)$$

The integral over  $t$  ensures that all possible rotation times are accounted for, with the fluorescence decay curve  $p(t)$  used as a weighting function. The full correlation function is represented by the product of two detection event probabilities and an intermittent rotation, integrated over all possible orientations:

$$g_{\alpha\beta}^{\gamma\delta}(\tau) = \left\langle I_{\alpha}^{\gamma}(t) I_{\beta}^{\delta}(t + \tau) \right\rangle_t \quad (2.29)$$

$$= \int d\mathbf{\Omega} \int d\mathbf{\Omega}' Q_{\beta}^{\delta}(\mathbf{\Omega}) G(\mathbf{\Omega}, \mathbf{\Omega}', \tau) Q_{\alpha}^{\gamma}(\mathbf{\Omega}') \quad (2.30)$$

The correlation curves are calculated analytically in Mathematica (*Wolfram Research, USA*), given in explicit form in the appendix (see sec. A.2). Out of the  $(2 + 2)^2$  possible curves, only six unique ones remain after symmetry considerations:

$$g_{\parallel\parallel}^{\parallel\parallel} = g_{\perp\perp}^{\perp\perp} \quad (2.31)$$

$$g_{\perp\parallel}^{\parallel\parallel} = g_{\parallel\perp}^{\parallel\parallel} = g_{\perp\parallel}^{\perp\perp} = g_{\parallel\perp}^{\perp\perp} \quad (2.32)$$

$$g_{\parallel\parallel}^{\perp\perp} = g_{\parallel\parallel}^{\parallel\perp} = g_{\perp\perp}^{\parallel\perp} = g_{\perp\perp}^{\perp\parallel} \quad (2.33)$$

$$g_{\perp\parallel}^{\perp\perp} = g_{\parallel\perp}^{\perp\perp} \quad (2.34)$$

$$g_{\perp\perp}^{\parallel\parallel} = g_{\parallel\parallel}^{\perp\perp} \quad (2.35)$$

$$g_{\parallel\perp}^{\perp\perp} = g_{\perp\parallel}^{\perp\perp} \quad (2.36)$$

The translational vesicle diffusion happens on a slower time-scale and can be fitted and subtracted from the correlation curves before fitting eq. (2.30). An example is given in fig. 2.7.

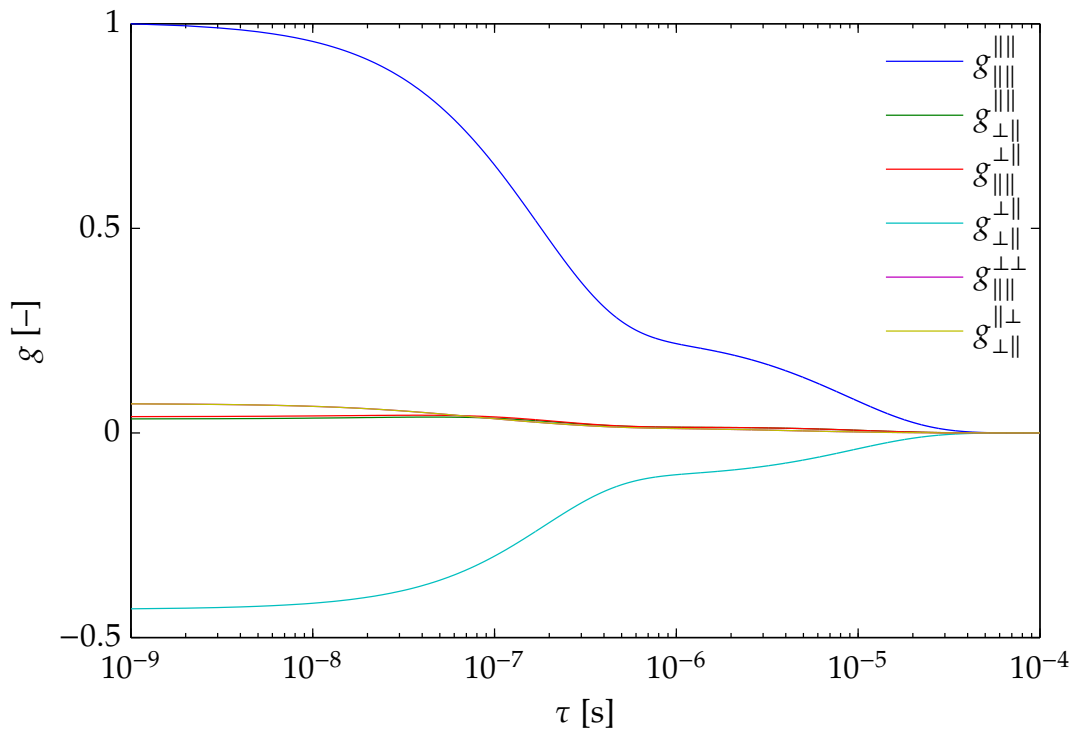


**Figure 2.7:** Theoretical polarisation-resolved FCS curves for vesicle rotational diffusion. The chosen parameters are  $\tau_F = 2.5$  ns,  $D_{\parallel} = 1.4 \cdot 10^6$  s $^{-1}$ , and  $D_{\perp} = 1.8 \cdot 10^4$  s $^{-1}$ .  $g_{\parallel\parallel}^{\perp\perp}$  and  $g_{\parallel\perp}^{\perp\perp}$  overlap almost completely in this case. The curves are background-corrected and normalised w.r.t.  $g_{\parallel\parallel}^{\parallel\parallel}(\tau = 0)$ .

### 2.1.4 Dynamic light scattering

In an actual experiment, the correlation curves represent an average over all molecules traversing the detection volume. As both the translational lipid and the rotational vesicle diffusion, as well as the probability to detect a vesicle at all, scale with its diameter, the fit model for the curves has to include the vesicle size distribution  $\varrho(R)$ . One simple way to obtain  $\varrho(R)$  is dynamic light scattering (DLS). Here, the constructive and destructive interference between a laser source focused into a solution of molecules and the back-scattered light collected at some angle  $\theta$  is measured, correlated in time, and the hydrodynamic radius distribution  $\varrho_I(R)$  extracted from it.  $\varrho_I(R)$  scales with the scattering intensity which depends on the scattering volume  $V$  and a form factor  $F_q$  representing the particle geometry. The true number distribution  $\varrho_N(R)$  can be back-calculated using the expression

$$\varrho_N(R) = \frac{\varrho_I(R)}{|V(R)F_q(q, R)|^2} \quad \text{with} \quad q = \frac{4\pi n}{\lambda} \sin \theta \quad , \quad (2.37)$$

where  $q$  is the scattering factor,  $n$  is the vesicle index of refraction, and  $\lambda$  is the laser wavelength [82]. The vesicles can be approximated as thin spherical shells of thickness  $\zeta$  having a volume of  $V = 4\pi\zeta(R - \zeta/2)^2$  and a form factor of

$$F_q = \frac{3}{x^3(1 - \gamma^3)} \sin x - \sin \gamma x - x \cos x + \gamma x \cos \gamma x \quad (2.38)$$

with  $x = qR$  and  $\gamma = (R - \zeta/2)/R$  [83].

The contribution of a vesicle to the correlation depends on the probability of containing at least one fluorescent label which scales with the product of its surface area and is given by  $\varrho_{\text{FCS}}(R) = R^4 \varrho_N(R) / \int R^4 \varrho_N(R) dR$ . Unsurprisingly,  $\varrho_{\text{FCS}}(R) \approx \varrho_I(R)$  as  $\zeta \ll R$ .

### 2.1.5 Chemicals & reagents

1,2-dielaidoyl-*sn*-glycero-3-phosphocholine (18:1  $\Delta^9$ -Trans-PC<sup>2</sup>), 1,2-dioleoyl-*sn*-glycero-3-phosphoethanolamine-N-(biotinyl) sodium salt (BPE), and a Mini-Extruder were bought from *Avanti, USA*. Chloroform, methanol, acetone, pyridine, and (3-glycidyloxypropyl) trimethoxysilane were obtained from *Sigma Aldrich, Germany*. *Atto-Tec, Germany* provided the fluorescent labels Atto647N, Atto655, and their headgroup-labelled 1,2-dihexadecanoyl-*sn*-glycero-3-phosphoethanolamine (DPPE) variants with the exception of KK114-DPPE from *Abberior, Germany*<sup>3</sup>.  $\alpha, \omega$ -bis-amino-polyethylene glycol

<sup>2</sup>The chemical is denoted as DEPC<sub>18</sub> in this thesis, as DEPC usually refers to 1,2-dierucoyl-*sn*-glycero-3-phosphocholine.

<sup>3</sup>Lipid-conjugated dyes are denoted by a <sup>l</sup> superscript.



(PEG, 2 kDa),  $\alpha$ -methoxy- $\omega$ -amino-PEG (MeO-PEG, 2 kDa), and  $\alpha$ -biotinyl- $\omega$ -amino-PEG (Biotin-PEG, 3 kDa) were purchased from *Rapp Polymere, Germany*. NeutrAvidin<sup>4</sup> protein as well as 1,1'-Dioctadecyl-3,3',3'-tetramethylindodicarbocyanine perchlorate (DiD) were acquired from *Thermo Scientific, USA*. dSQ12S dye [84] was kindly provided by Andrey S. Klymchenko and his group (Laboratoire de Biophotonique et Pharmacologie, Université de Strasbourg, France).

Unless stated otherwise, all reactions were performed in phosphate buffered saline (PBS, 137 mM NaCl, 2.7 mM KCl, 1.5 mM KH<sub>2</sub>PO<sub>4</sub>, and 8.1 mM Na<sub>2</sub>HPO<sub>4</sub>, chemicals by *Sigma Aldrich*) at a pH of 7.4 using Milli-Q water (filter system by *Millipore Corp., USA*) as solvent. Coverslips of various sizes and thickness #1.5 were all purchased from *Menzel, Germany* combined with immersion oils Immersol518F and ImmersolW by *Zeiss, Germany* and adhesive strip incubation wells by *Grace Bio-Labs, USA*.

### 2.1.6 Vesicle sample preparation

DEPC<sub>18</sub>, BPE, and all lipid-conjugated organic dyes were dissolved in chloroform at concentrations of 10 mg ml<sup>-1</sup> for DEPC<sub>18</sub> and 0.01 mg ml<sup>-1</sup> for the lipid conjugates while dSQ12S was kept in methanol at 15  $\mu$ M. 60  $\mu$ l DEPC<sub>18</sub> and 0.2  $\mu$ l dye conjugate were mixed in a chloroform-cleaned glass vial. In case of surface tethered SUVs, 0.1  $\mu$ l of 0.1 mg ml<sup>-1</sup> BPE was added beforehand. For GUVs, the BPE volume was increased to 1  $\mu$ l.

Small unilamellar vesicles were prepared by evaporating the solvent in vacuum for 30 min at 30°C and rehydrating the dried lipid film with 500  $\mu$ l of PBS. After 5 min of swelling and 1 min of vortexing, the vial was shaken for 1 h at 1400 rpm and 30°C in a thermomixer (*Eppendorf, Germany*). The multilamellar vesicles obtained this way were then extruded through polycarbonate membranes of various pore sizes (30 nm to 200 nm, *Whatman, USA*), shearing off the different layers until unilamellar vesicles remained and the solution was clear. Extrusion was performed for 31 cycles, sufficient to achieve a mostly uniform size distribution with an average diameter close to the pore size. Using a custom-made motorised extruder, the cycle number could be increased considerably, yielding a more symmetrical distribution which was stable for a longer time. If not used directly, the vesicles were stored at 4°C for up to four days.

In case of the rotational diffusion experiments, 49.5  $\mu$ l PBS with 0.5  $\mu$ l dSQ12S stock solution was vortexed briefly and immediately added to 50  $\mu$ l unlabelled SUV suspension. The mixture was shaken at 1200 rpm and 30°C for 1 h. Due to efficient membrane insertion and negligible fluorescence of dSQ12S outside of membranes, the solution could be applied for further use without additional purification steps. The struc-

<sup>4</sup>NeutrAvidin is a trademark name, the chemical is referred to as neutravidin in the thesis.

tural integrity of any vesicles could be examined by mixing the hydration and extrusion buffer with pyridine. Pyridine is a fluorophore with an emission wavelength of  $\lambda_{em,max} = 542$  nm, well below the near-infrared spectra of the membrane dyes. Lumen and membrane could therefore be imaged simultaneously in two separate colour channels. Only intact vesicles showed a signal in both channels.

Giant unilamellar vesicles were produced in a custom-built electroformation chamber pictured in fig. 2.8. After assembling the chamber, the lipid mixture was pipetted onto the bottom metal plate and the solvent evaporated as detailed above. The suspension was rehydrated in 500  $\mu$ l of 280 mM sucrose (*aq*) and the container closed with the upper electrode. Electroformation was performed for 3 h at 15 Hz AC and a peak-to-peak voltage of 1.2 V. Afterwards, 50  $\mu$ l supernatant was immediately discarded and the remaining solution was drawn into a pipette while simultaneously rinsing the electrode surface. The size of the thus prepared GUVs ranged from 10  $\mu$ m to 50  $\mu$ m.

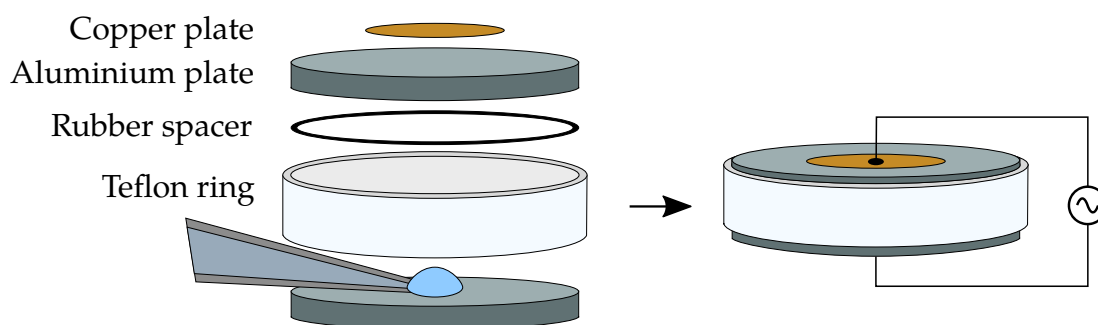


**Figure 2.8:** Electroformation chamber for GUV assembly. Two aluminium electrode surfaces surrounded by a teflon ring are contacted by a copper plate and an aluminium body. The square-wave AC current of  $V_{pp} = 1.2$  V at 15 Hz is supplied by a HM 8030-2 function generator from *Hameg, Germany*.

### 2.1.7 Surface coating & vesicle immobilisation

For the dynaMIET experiment, vesicles had to be selectively bound to a glass surface without interacting with it in any way. The latter was a very important requirement as the spherical shape had to be kept intact for the FCS theory to apply. In the case of rotational diffusion in solution, surface treatment was generally less important. However, due to the length of the measurements, it was beneficial to use passivated coverslips because the vesicles could otherwise accumulate on the surface, depleting the solution until their concentration was too low. A popular strategy for tethering macromolecules to the coverslip is biotinylation. Here, a biotin molecule is attached to the particle of choice and the surface is coated with streptavidin. Streptavidin forms a very strong bond with biotin and possesses four binding pockets in its wild-type form. This makes

it possible to chain-link them in a biotin-streptavidin-biotin (BSB) interaction, allowing for a high degree of flexibility. Passivation against vesicles, on the other hand, is much more difficult owing to their amphiphilic nature. Treating the surface with bovine serum albumin [85], poly-L-lysine [86], or similar compounds can considerably reduce non-specific binding without compromising the BSB scheme. In the final approach, two different PEGylation methods developed in the labs of Ha [87] and Piehler [88] were combined. Here, the coverslip was coated with a monolayer of polyethylene glycols containing a methoxy group at one end. This alkoxy group is neither hydrophilic enough to bind the polar lipid headgroups, nor does it interact with their alkyl chains. A small amount of Biotin-PEG could be added to bind vesicles in a specific way.

Gold-coated coverslips were assembled through vapour deposition of titanium, gold and silica onto a standard #1.5-thickness coverslip using a Univex 350 (*Leybold, USA*). Normal and coated coverslips were cleaned and the surface hydrophilised in a plasma cleaner (PDC-001, *Harrick Plasma, USA*) for 20 and 4 min, respectively. The surfaces were washed in Milli-Q water and dried in a N<sub>2</sub> stream before being incubated in pairs with a drop of silane at 80°C for 60 min. The silanised slides were washed in acetone and blown dry again. The powderised PEG was molten at 80°C and a 25 µl drop was applied to each surface pair. After another incubation period of 4 h at 80°C, they were cleaned thoroughly in water using a sonication bath and stored at 4°C for up to four weeks. Tethering coverslips were prepared through a 90/10 w/w% mix of MeO- and Biotin-PEG instead of pure MeO-PEG and stored for two weeks.

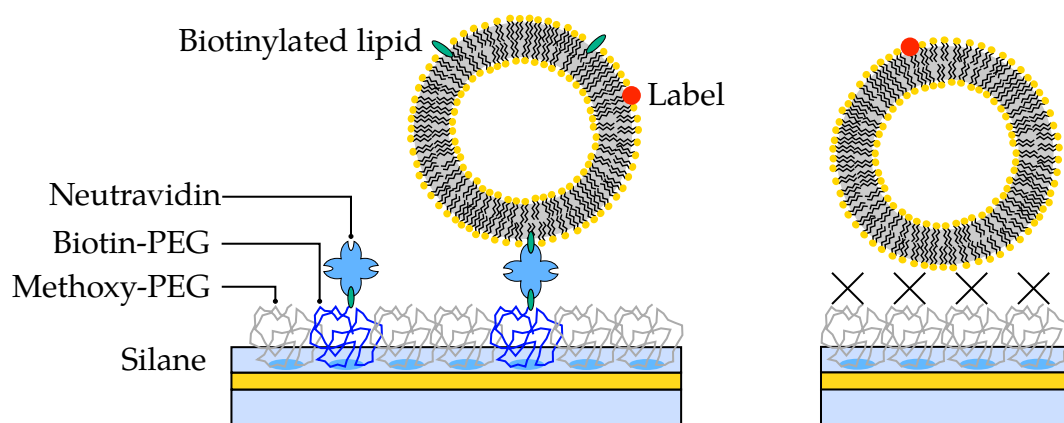


**Figure 2.9:** PEGylated surfaces employed in vesicle FCS experiments.

For control experiments, double-sided adhesive strip wells were attached to the surfaces to contain the sample volume. The biotinylated coverslips were incubated in 0.1 mg ml<sup>-1</sup> neutravidin diluted in PBS for 1 h, rinsed, and then filled with 120 µl GUV solution. For the dynaMIET experiments, a flow chamber was built instead using double-sided tape. After incubation with neutravidin and thorough rinsing, SUVs di-

luted by a factor of 1 to 100 were flushed in and left to incubate for 30 min. Finally, the chamber was rinsed again and the experiment started. Rotational diffusion FCS was performed with passivated slides using the same strip wells mentioned above without adding neutravidin. The final surface configurations are pictured in fig. 2.9.

The advantage of using molten-PEGylated slides is twofold: Exchanging PEGs or silanes allows for a large variety of functional surface groups without having to revise the whole protocol. Furthermore, the application of highly concentrated molten PEG is straightforward, reliable in its complete coverage, and highly reproducible. The surfaces are smooth, stable, and chemically inert except for the functional groups. The protocol is thus very flexible and the coverslips created this way are ideal for dealing with aggressive reagents.

### 2.1.8 Experimental data acquisition & evaluation

Diffusion coefficients of lipid dyes in planar lipid bilayers were determined by imaging GUVs. Fluorescence imaging of GUVs immobilised on the surface was performed on a standard IX71 wide-field fluorescence microscope (*Olympus, Germany*) employing a PhoxX 488 or PhoxX 647 laser (*Omicron-Laserage, Germany*), an iXon Ultra 897 (*Andor, Ireland*), and a UPLSAPO 60× NA 1.2 objective (total magnification  $M = 96$ ). The microscope was focused onto the top of a GUV and 5000 frames were recorded at 200 Hz in fastest-frame mode at an EM-gain of 100 and a laser power of 100 mW. This was repeated for at least 10 different GUVs. Movies of diffusing lipids were analysed by single particle tracking and diffusion coefficients extracted using the TrackNTrace software package as detailed in chap. 3. Photo-physical characteristics of conjugate-free and lipid-bound dyes were recorded on the same setup in the same fashion. Single-molecule intensity traces were extracted with the particle tracking subroutine of TrackNTrace. From these trajectories, distributions of emission intensities, fluorescence on- and off-rates, and photo-bleaching lifetimes could be calculated directly.

DynaMIET measurements were carried out on the MicroTime 200 using the built-in SymphoTime software. The excitation laser was pulsed at 40 MHz with an average energy output of 1  $\mu$ W and a surface scan of a 20  $\mu$ m  $\times$  20  $\mu$ m area was recorded. Bright, circular spots likely to be vesicles and not agglomerated material were marked manually after which the software would perform an automated point scan for 20 s on each spot. This process was continued for several hundred spots. Cross-correlations of all spots were calculated, averaged, and fitted with the use of in-house built software as outlined before [81]. MIET calibration curves were calculated with an analysis suite developed by Daja Ruhlandt and published on Jörg Enderlein's website [89].

Prior to use, SUVs intended for rotational diffusion experiments FCS were charac-

terised by dynamic light scattering to determine the vesicle size distribution. These experiments were made possible with the kind help of Dr. Christian Roßner, Dr. Dennis Hübner and Wentao Peng<sup>5</sup> and were performed on a Zetasizer Nano S (*Malvern Instruments, UK*). Solution measurements were performed on the MicroTime 200 with two lasers and four detectors as explained above, the power was adjusted to 3  $\mu\text{W}$  per laser per pulse. Photon arrival times were recorded for at least 3 h and correlated with the same software used in the dynaMIET experiments. The curves were fitted in MATLAB by a trust-region reflective non-linear least-squares algorithm using the model parameters  $D_{\perp}$  and  $D_{\parallel}$ , and the vesicle size distribution  $\varrho(R)$ :

$$g_{\text{fit}}(\tau) = \int g_{\text{theo}}(\tau, D_{\perp}, D_{\parallel})\varrho(R)dR \quad (2.39)$$

$$D_{\perp} = \frac{D_{\text{trans}}}{R^2} + D_{\text{rot}} = \frac{D_{\text{trans}}}{R^2} + \frac{k_B T}{8\pi\eta R^3} \quad (2.40)$$

$\eta$  is the solvent's dynamic viscosity which is assumed to be the same as that of water. Instead of integrating over the correlation curve, one can also integrate over the diffusion coefficient itself, as done by Yoshii et al. [57]. Both methods are employed in this work.

---

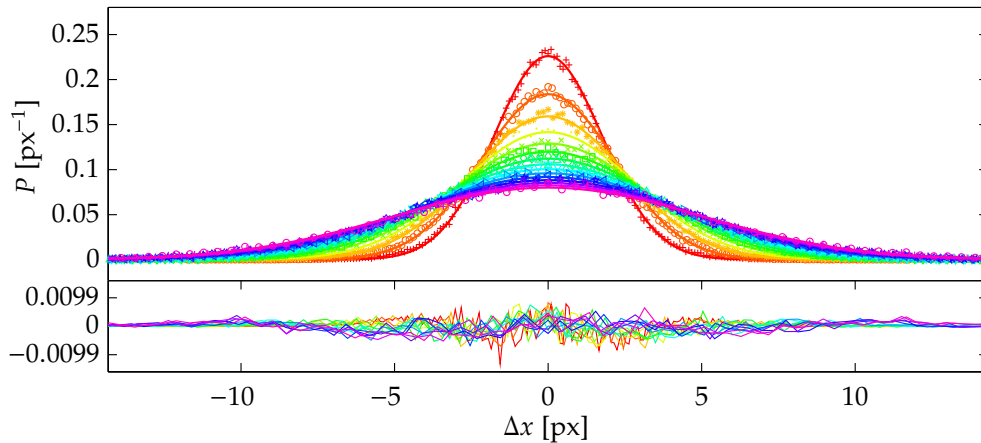
<sup>5</sup>Macromolecular Chemistry Group, Fakultät für Chemie, Universität Göttingen.

## 2.2 Results

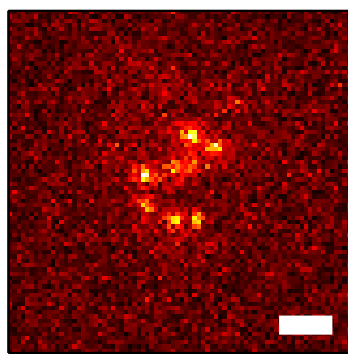
### 2.2.1 Preliminary experiments

#### Free diffusion coefficient

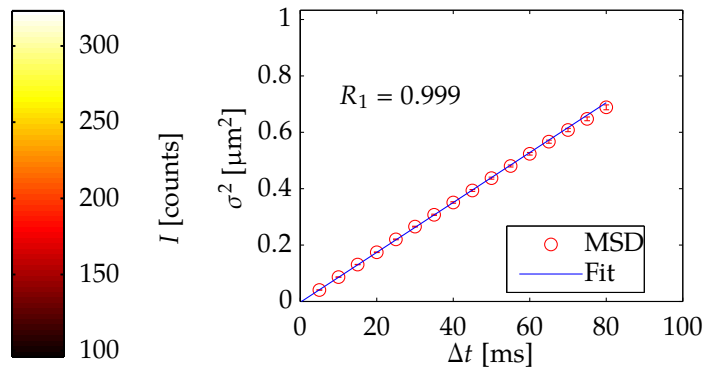
To better quantify the diffusive speed of fluorescent dyes in curved membranes of different compositions or lipid phases, one compares against a known calibration standard, in this case GUVs. Due to their size of  $> 10 \mu\text{m}$ , GUVs are sufficiently planar at the molecular level and free of any surface interaction apart from the contact site. One difficulty in using them for diffusion measurements, however, are membrane undulations resulting from the solvent convection or osmotic pressure differences. In an FCS experiment, they can drastically alter the decay of the correlation curve and thus the estimated diffusion coefficient.



(a) Displacement histograms with residuals.



(b) dSQ12S diffusing in DEPC<sub>18</sub> GUV. Scale bar is  $2 \mu\text{m}$ .



(c) MSD curve with linear fit.

**Figure 2.10:** Single particle tracking in DEPC<sub>18</sub> GUVs for dSQ12S dye. The displacement histograms represent over 22000 trajectories from 10 different movies. The colour shift from red to purple indicates an increase in displacement time. A linear fit of the MSD curve returns  $D_{\text{MSD}} = 4.58(3) \mu\text{m}^2 \text{s}^{-1}$ .

	dSQ12S	DiD	Atto655 <sup>l</sup>
$D$ [ $\mu\text{m}^2 \text{s}^{-1}$ ]	4.58(3)	5.3(3)	6.0(5)

**Table 2.1:** Diffusion coefficients of lipid dyes in GUVs.

For this reason, particle tracking is employed in its stead. Fig. 2.10 displays the result of one such experiment and tab. 2.1 shows the diffusion coefficients for the dSQ12S dye used for rotational FCS, the similar DiD, and the organic dye conjugate Atto655<sup>l</sup>. The diffusion coefficients are slightly lower than would be expected for a poly-unsaturated lipid like DEPC<sub>18</sub> but still agree well with literature values for similar lipids such as 22:1 DEPC or SLPC, as measured by FCS and NMR [90, 91]. DEPC<sub>18</sub> has a much higher phase transition temperature of  $T_c = 12^\circ\text{C}$  than other PC fatty acids with  $T_c$  values usually below  $0^\circ\text{C}$  owing to its mono-trans-unsaturation as depicted in fig. 2.11. This translates into a comparatively high membrane viscosity at room temperature and thus slower diffusion. DiD and Atto655<sup>l</sup> show very similar results in accordance with previous experiments [92, 93]. The notably lower diffusion coefficient of dSQ12S can be attributed to its structure (fig. 2.11).

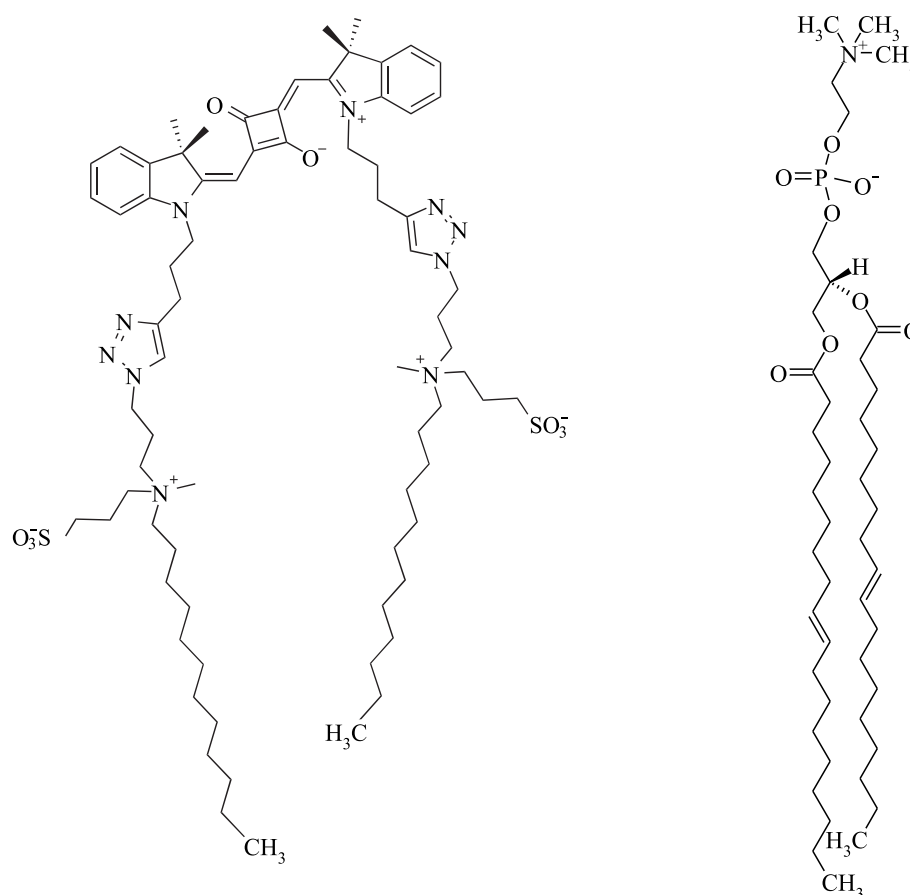


**Figure 2.11:** Chemical structures of dSQ12S (adapted from [84]) and DEPC<sub>18</sub>.

The ammonium sulphate group, a zwitterionic moiety, greatly increases the binding affinity of the dye. It is related to hydrophobic mismatch between lipid backbone and dye and a natural characteristic of slower diffusing membrane compounds [94]. Mixture effects can be ruled out as the dye-to-lipid ratio was kept at 1 : 10000 or lower so as to avoid the formation of any lipid domains.

### Surface preparation

As noted in the methods section, the surfaces employed in all vesicle measurements have to fulfil two roles: Prevent non-specific binding of vesicles to the surface, and tether functionalised lipids in such a way so as not to disturb the spherical shape. In a control assay, a dual-channel flow chamber was constructed from a single biotin-MeO-PEGylised coverslip. Both chambers were filled with pyridine- and Atto655<sup>l</sup>-labelled SUVs and incubated with neutravidin but the control group SUVs lacked biotinylated lipid. After letting the liposomes settle on the surface, the chambers were flushed again with PBS to get rid of any pyridine in solution. Fig. 2.12 shows dual-colour scan images of both channels.

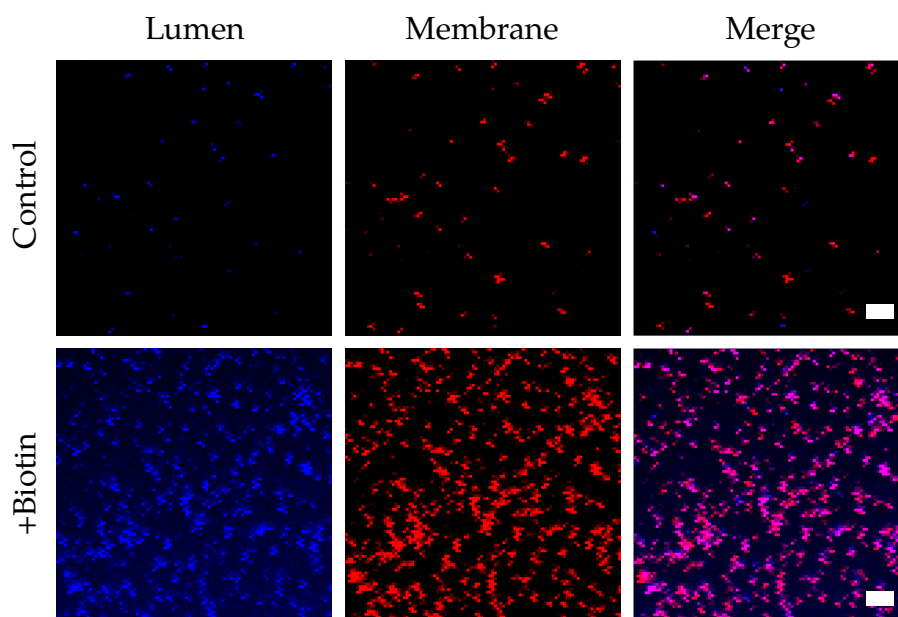


**Figure 2.12:** Dual-colour surface control images of multilabelled SUVs. The intensity was normalised with respect to each individual image for maximum contrast. The actual intensity in the control group is about ten times lower when compared to the biotinylated vesicles. Scale bar is 5  $\mu\text{m}$ .

Adding biotinylated lipid to the SUVs leads to an increase in surface binding by a factor of 10. It is evident that the biotin-neutravidin-biotin scheme does not damage the SUVs as most fluorescent membrane patches correspond to a pyridine signal,



indicating intact vesicles. Furthermore, non-specific binding to the membrane is rare despite neutravidin being slightly hydrophilic in part due to several exposed lysine residues. In most cases, it seems to be limited to lipid aggregates and not vesicles. In a dynaMIET experiment, such intensity traces can be easily identified from their low amplitude and correlation, and discarded. Without the protein, non-specific binding is practically eliminated (data not shown).

The last remaining issue is shape distortion of the liposome. If a vesicle is bound to more than one neutravidin molecule, biotinylated lipids can agglomerate at the contact site. This leads to increased tethering which causes vesicles to get squashed [95]. While both surface and SUV membrane are highly biotinylated, the neutravidin concentration is adjusted to an average of  $10 \mu\text{m}^{-2}$  which should be sufficiently low to prevent such issues.

### 2.2.2 Dynamic MIET in small unilamellar vesicles

Determining the diffusion coefficient of a membrane compound in nanometre-sized vesicles through dynamic MIET is a challenging task, though not obviously so. Conceptually, dynaMIET is relatively simple to set up: Any laboratory equipped with a conventional FCS setup is capable of performing such an experiment. The main difficulties lie in preparing the metal-coated coverslip, preserving the sample during the measurement, and collecting enough photons from the vesicles to calculate a correlation curve with sufficient precision.

Metal-coating of microscopy slides is performed in the faculty's clean-room facilities using a vacuum evaporation machine. The thin gold layer of 10 nm to 15 nm is wedged between 2 nm of titanium which increases adhesion. A top layer of  $\text{SiO}_2$  protects the metals from corrosion and enables the use of silanes during surface treatment. The silica thickness is adjusted such that the maximum distance between fluorophore and metal layer is well within the linear MIET regime.

The second issue is easily tractable by dynaMIET. For every experiment, the vesicles' radii have to be known to extract the diffusion coefficient from the correlation curve as stated in eq. (2.15). They can either be measured by FCS during sample preparation on the same setup or independently by SPT. I am choosing the latter due to the small measurement time of several seconds compared to 30 min for a typical FCS study. The MIET correlation curves are then compiled by scanning the surface for single-vesicle patterns and performing a point scan on each signal source until the fluorophore is photo-bleached. The correlation function is calculated for each vesicle separately and then averaged. Additionally, all photons can also be collected into a single TCSPC curve from which an average lifetime can be determined. This lifetime can then be back-

calculated to an average height of the fluorophores above the surface if their dipole orientations are known. Since the dye can rotate freely, the orientation is assumed to be random. The lifetime-to-height calibration curve is therefore simply the average of the curves of a completely vertically or completely horizontally polarised dipole. Fig. 2.13 illustrates the outcome of such a measurement gathered from 212 intensity traces.

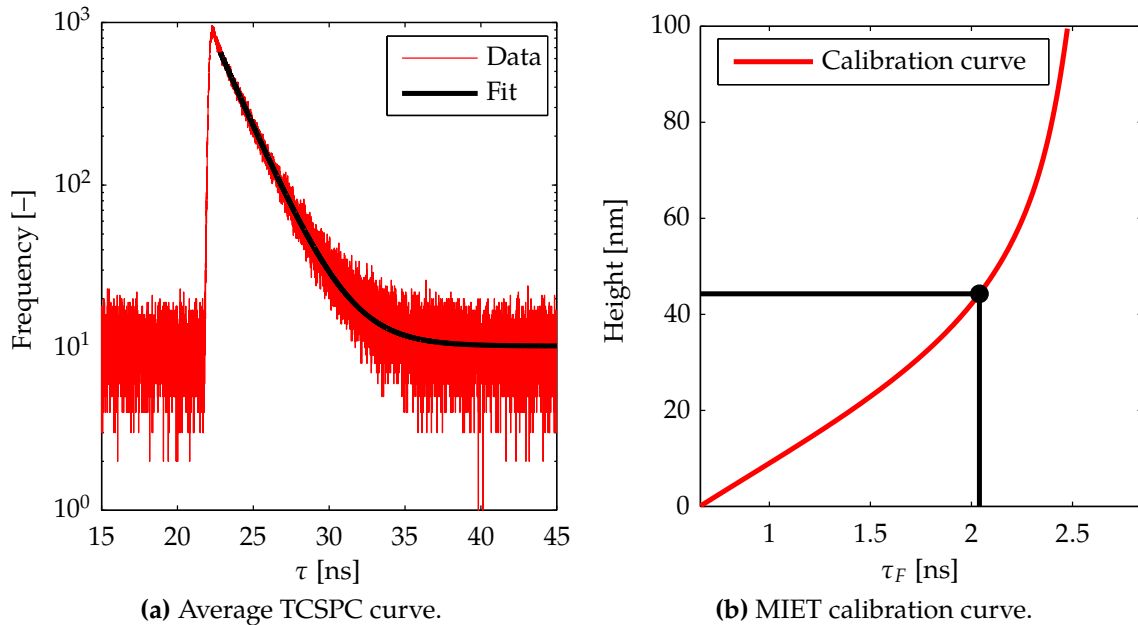


**Figure 2.13:** Vesicle height on Biotin-MeO-PEG surface determined by MIET. An exponential tail-fit of the TCSPC histogram returns a lifetime of  $\tau_F = 2.04(1)$  ns. Assuming a free-space lifetime of  $\tau_{F,0} = 2.9$  ns, and a quantum yield of  $\nu = 0.46$ , this translates to a height of  $43.7(1)$  nm. The MIET calibration curve is given here for a glass coverslip coated in 2/12/2/25 nm Ti/Au/Ti/SiO<sub>2</sub>.

The determined height of  $h_{\text{MIET}} = 43.7(1)$  nm is slightly higher than the hydrodynamic radius  $r_H = 34(1)$  nm measured by SPT. However, the more distant a fluorophore is to the metal layer, the higher its contribution to the average TCSPC curve will be. The two values are thus in very good agreement, confirming that the vesicles indeed retain their spherical shape when being tethered.

The total cross-correlation for the same experiment is shown in fig. 2.14. It is immediately obvious that the average photon count per vesicle is not nearly sufficient to obtain a quantifiable result. In the  $\mu\text{s}$ - to  $\text{ms}$ -time region of lipid diffusion, the cross-correlation is entirely noise-dominated. Although an exponential decay function can be fitted to the data, the converted diffusion coefficient of  $D_{\text{fit}} = 0.13(1) \mu\text{m}^2 \text{s}^{-1}$  is a factor of  $\approx 100$  smaller than expected. Most likely, it represents axial movement of the tethered vesicles or results from intensity fluctuations not caused by diffusion. Fig. 2.15 depicts several typical vesicle timetraces from the same experiment.

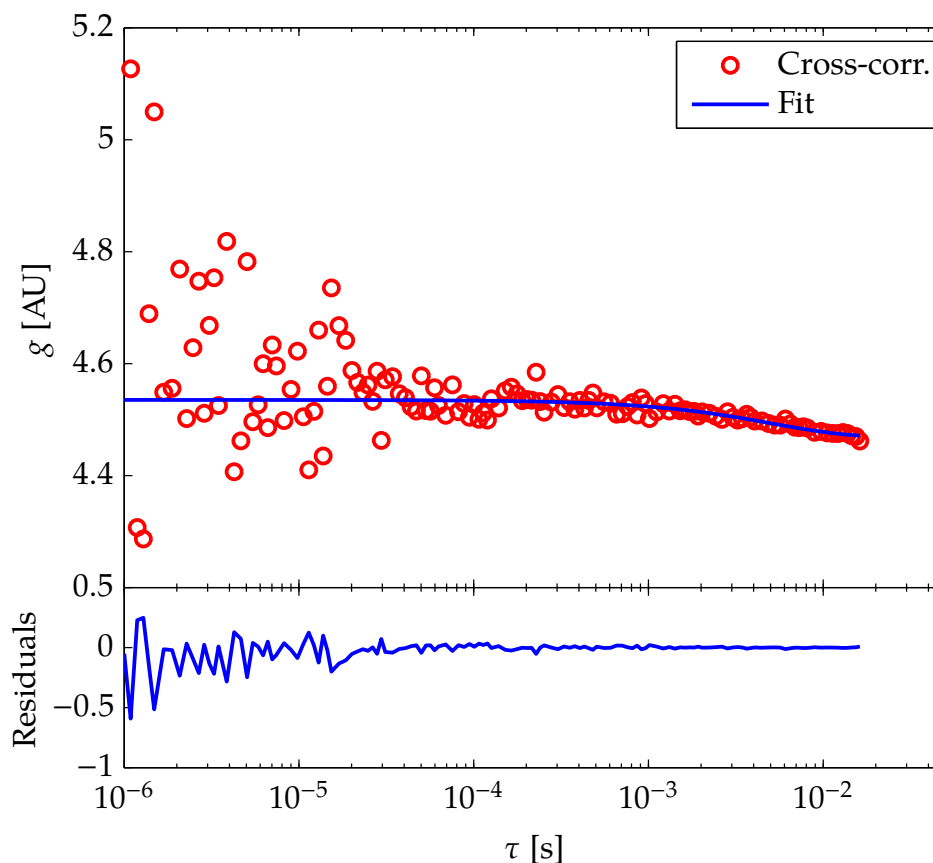


**Figure 2.14:** DynaMIET cross-correlation curves of Atto655<sup>l</sup>-labelled vesicles. The exponential decay time  $\tau_{\text{fit}} = 4.8(1)$  ms would suggest a diffusion coefficient of  $D_{\text{fit}} = 0.13(1) \mu\text{m}^2 \text{s}^{-1}$ .

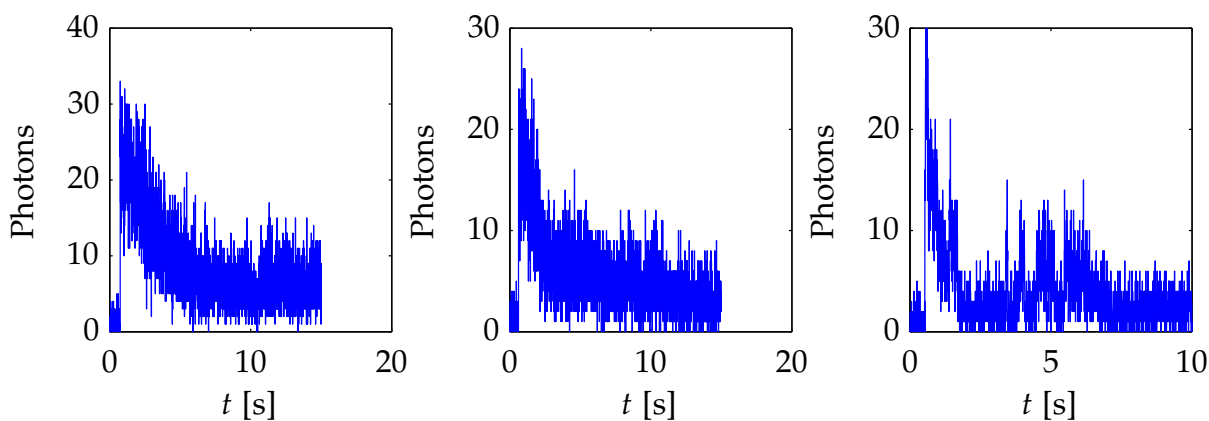


**Figure 2.15:** Timetraces of Atto655<sup>l</sup>-labelled vesicles from dynaMIET measurement.

In addition to the low fluorescence emission rate of  $\Phi \leq 10^3 \text{ s}^{-1}$ , the molecules also seem to bleach unusually fast in an abnormal, linear to exponential fashion. As the vesicles are underlabelled, most traces should show step-wise bleaching with one step. Increasing the excitation intensity only damages the fluorophores faster whereas

doing the opposite to extend the measurement time even further is not feasible. Another behaviour observed in a larger number of traces is fluorescence intensity decay followed by intermittent, spurious bursts as seen in fig. 2.15c. This “blinking” from and into a dark state is common in fluorophores where singlet-triplet inter-system crossing or the formation of a radical ion state are possible. However, these processes usually occur on  $\mu\text{s}$ - to  $\text{ms}$ -time-scales.

To get a better understanding of the underlying photo-physics, bleaching and off-state-switching behaviours of several lipid-conjugated dyes in different environments were examined further. This is achieved by imaging surface-bound fluorophores at low concentration with a wide-field microscope and tracking them. From these trajectories, fluorescence amplitudes, number of emitters and off-state lengths can be histogrammed. One can then fit bleaching times  $\tau_b$  and off-state durations  $\tau_{\text{dark}}$  to these distributions, and calculate mean intensity traces.

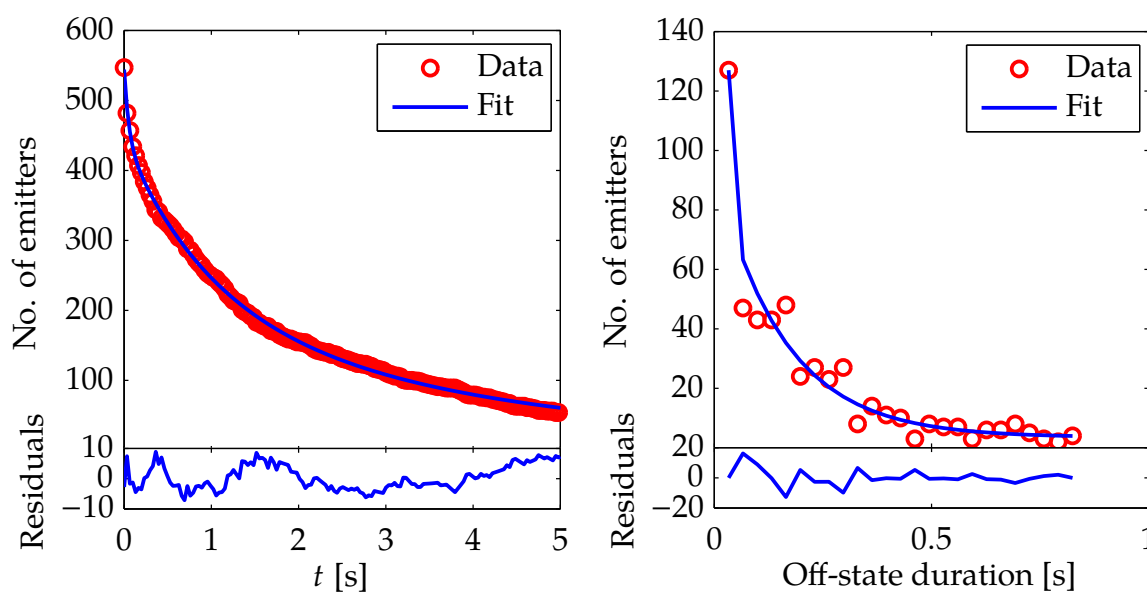


**Figure 2.16:** Bleaching and off-state distributions of Atto647N<sup>l</sup> in PBS. The photo-bleaching curve is fitted with a bi-exponential decay function, returning  $\tau_{b1} = 0.58$  s and  $\tau_{b2} = 3.04$  s. The off-state distribution follows a mono-exponential decay with  $\tau_{\text{dark}} = 0.10$  s.

It has been known for a long time that both bleaching and blinking of most organic dyes can be well described by an exponential decay function [60]. Fig. 2.16 shows that this still holds for the lipid-conjugated variants, in this case Atto647N<sup>l</sup>. The photo-bleaching distribution of all analysed dyes also show a second, short component which accounts for 30% of all emitters in some cases. Neither surface impurities nor buffer could have been responsible as they did not show any fluorescence in separate meas-

measurements. A dependence on surface coating could not be determined, either. Tab. 2.2 gives an overview of all dyes with the photo-bleaching rate averaged over both species.

Dye	Sample	$\langle \tau_b \rangle$ [s]	$\tau_{\text{dark}}$ [s]
Atto655 <sup>l</sup>	PBS	3.25(8)	0.17(2)
	SUV	0.80(3)	0.47(3)
KK114 <sup>l</sup>	PBS	4.30(9)	0.33(3)
	SUV	1.74(3)	0.22(1)
Atto647N <sup>l</sup>	PBS	2.05(4)	0.16(2)
	SUV	0.12(9)	0.56(1)

**Table 2.2:** Average bleaching times  $\langle \tau_b \rangle$  and dark-state durations  $\tau_{\text{dark}}$  of lipid-conjugated dyes. All bleaching curves show a bi-exponential decay, the number given here is the weighted average of both times.

All photo-bleaching survival times are well below 10 s regardless of fluorophore. This is already worrying considering that the same dyes in non-conjugated form can typically survive up to several minutes at higher excitation intensities [80]. Remarkably, the dyes consistently perform even worse when incorporated into SUVs. Both photo-damage and blinking increase substantially with the exception of KK114<sup>l</sup> which is only moderately affected upon bilayer addition. While a rise in bleaching rate simply leads to longer measurement times, the consequence of longer blinking is less obvious.

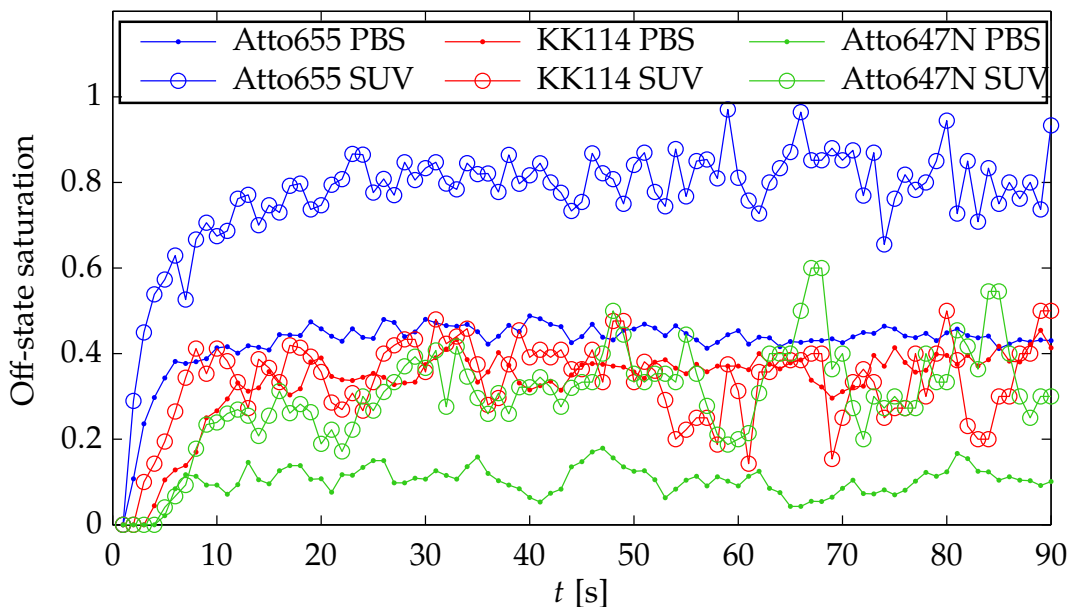


**Figure 2.17:** Off-state saturation of lipid-conjugated dyes.

The advantage of analysing the photo-physics by particle tracking is the possibility of distinguishing between dyes coming back to the on-state or just appearing for the first

time. By setting each trajectory's start to the beginning of the experiment and compiling a list of all emitters' states, it is possible to calculate the off-state saturation  $N_{\text{off}}/N_{\text{tot}}$ :

$$\dot{N}_{\text{off}} = -k_{\text{on}}N_{\text{off}} + k_{\text{off}}N_{\text{on}} \quad \text{where} \quad \dot{N}_{\text{on}} + \dot{N}_{\text{off}} = 0 \quad (2.41)$$

$$\rightarrow \frac{N_{\text{off}}}{N_{\text{tot}}} = \frac{k_{\text{off}}}{k_{\text{on}} + k_{\text{off}}} \cdot [1 - \exp(-t(k_{\text{on}} + k_{\text{off}}))] \quad (2.42)$$

The total number of molecules  $N_{\text{tot}} = N_{\text{off}} + N_{\text{on}}$  is determined for each frame individually and bleaching is not considered. These curves allow for a more balanced comparison of the off-state population dynamics of the dyes. The total switching rate is similar across all dyes and increases for SUVs as could be expected from the dark state durations. In all cases, the steady state equilibrium  $t \rightarrow \infty$  is reached in less than 10 s. The amplitudes differ greatly, starting at 30% with Atto647N<sup>l</sup> and approaching a dark-state saturation of up to 80% in Atto655<sup>l</sup>-labelled vesicles. KK114<sup>l</sup> is again less influenced by a change in environment.

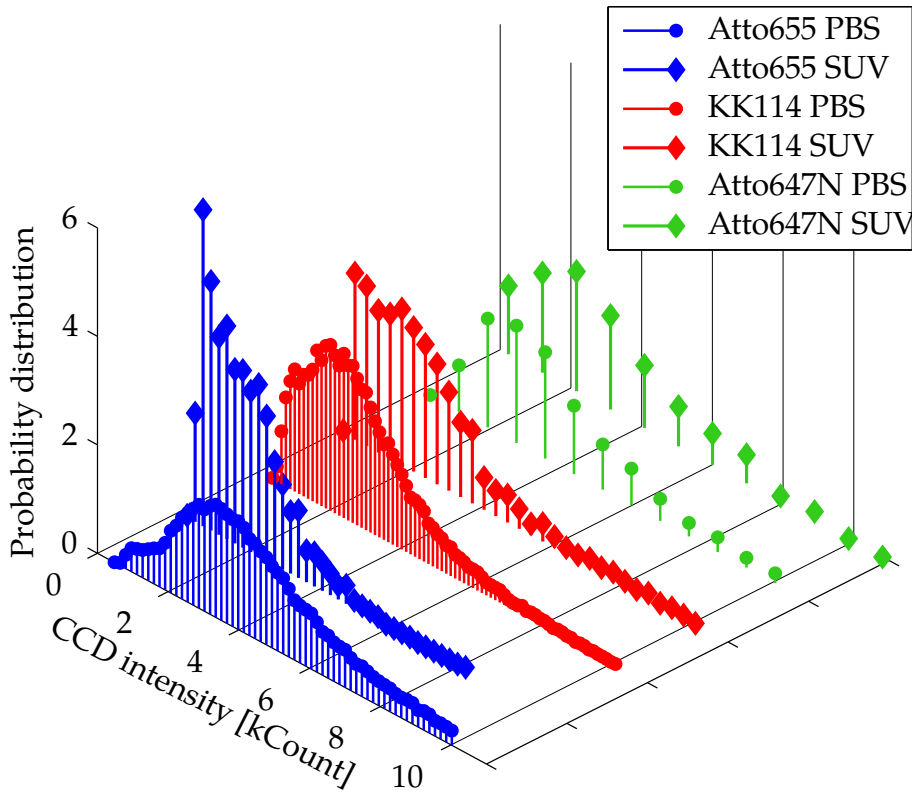


**Figure 2.18:** Intensity distributions of lipid-conjugated dyes.

These findings are consistent with the fact that the fluorescence intensity of the lipid dyes drops sharply at the onset of a dynaMIET experiment. They would also explain how the fluorophores only rarely recover after a few seconds as they would either spend most of the time in the dark state or simply bleach altogether. Normalising all intensity traces and averaging over them shows a brief drop in fluorescence at the beginning

which quickly stabilises (see fig. A.1) in accordance with the saturation curves. The problems caused by increased blinking in liposomes are mirrored by the intensity distributions, as shown in fig. 2.18. In a dynaMIET experiment, the metal layer absorbs an additional 32% of the signal, meaning these curves already represent a best-case scenario.

In summary, organic fluorophores employed with great success in previous single-molecule MIET studies can perform poorly when attached to a phospholipid. Photostability is drastically reduced while dark state switching becomes more prevalent at the same time. The situation deteriorates further when these lipid dyes are inserted into a bilayer. Due to the necessity of performing time-consuming surface pre-scans and single-molecule point scans together with these photo-physical issues, the signal collectible in one measurement is simply too low. All dynaMIET experiments were conceived under the assumption that only the most bright, stable dyes commonly used in localisation microscopy would provide an adequate signal-to-noise ratio. Membrane dyes frequently used in biology such as BODIPY-derived fluorophores, Texas Red, plasma membrane stains like CellMask Deep Red, or DiI and its variants were ruled out from the start due to low extinction coefficients, high bleaching rates, or presence of, sometimes several, triplet states. With no alternatives to turn to at the time of the experiments, I shifted to rotational diffusion as an alternative to measure membrane diffusion in liposomes.

### 2.2.3 Rotational diffusion of small unilamellar vesicles

#### Vesicle size distributions

Analysis of the rotational diffusion FCS curves requires precise knowledge of the vesicle diameter. In contrast to a typical single-molecule experiment, the vesicle size follows a unimodal distribution which has to be taken into account during data fitting according to eq. (2.40). The vesicle size distribution is determined in tandem with the FCS experiment via dynamic light scattering. Fig. 2.19 shows the results together with the averaged radii  $\langle R \rangle = \int R \rho(R) dR$ .

In most cases, the average diameters are larger than the extrusion membrane pore size  $2R_p$ . Both the membrane and the vesicle itself are relatively flexible, meaning the SUVs can squeeze through the membrane pores even if their size should prevent them from doing so, given sufficient pressure. Another explanation for the vesicle sizes is spontaneous fusion. As DEPC<sub>18</sub> is a closely packed planar lipid, its equilibrium vesicle diameter is larger than most pore sizes. All samples were stored below the phase transition temperature, however, which prevents the vesicles from fusing together during

storage. The size difference between freshly prepared and stock SUVs was negligible, meaning size fluctuations during data acquisition can be safely ruled out.

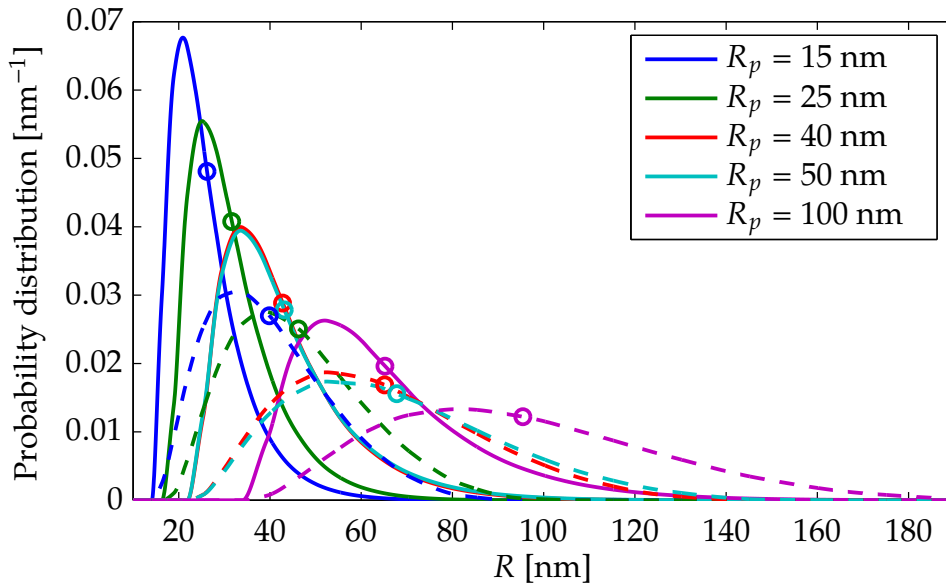


**Figure 2.19:** Vesicle size distributions for different extrusion pore diameters  $R_p$ . Solid lines indicate number distributions  $\rho_N(R)$ , dashed lines indicate intensity distributions  $\rho_I(R)$ . The circles denote the average radii  $\langle R \rangle = \int R \rho(R) dR$ .

In addition to the DLS measurements, the hydrodynamic radius can also be determined by 2f-FCS. While 2f-FCS only provides an average size instead of a distribution, it does inform about fluorescence labelling efficiency: When converting the number distribution  $\rho_N$  to the intensity distribution  $\rho_I$ , it is generally assumed that the labelling scales with the vesicle surface area. For a highly curved bilayer, however, the outer monolayer is more fragmented and vulnerable to dye insertion. The vesicle diameter observed in an FCS experiment could therefore be lower than  $\langle R \rangle_I$  depending on the average size. The outcome of one such 2f-FCS measurement is depicted in fig. 2.20.

All average radii and their standard deviations are listed in tab. 2.3. As suspected, the 2f-FCS results lie somewhere between both distribution averages, indicating that the fluorophore's affinity for curved membranes is indeed higher. The fit error, which was obtained by bootstrapping in this case, reflects the overall brightness distribution and is generally higher for larger vesicles. A "blank" sample containing only fluorescent dye displayed only negligible intensity which was completely uncorrelated. It can thus be safely assumed that the fluorophore integrates quickly into the membrane and stays non-fluorescent in solution as suggested [84], with the exception of dye aggregates. These are very rare, however, and can easily be eliminated from the analysis by filtering out the respective photon bunches. For clarity, in addition to an integration over both distributions, the rotational analysis is also carried out with the fixed  $R_{\text{FCS}}$  values.



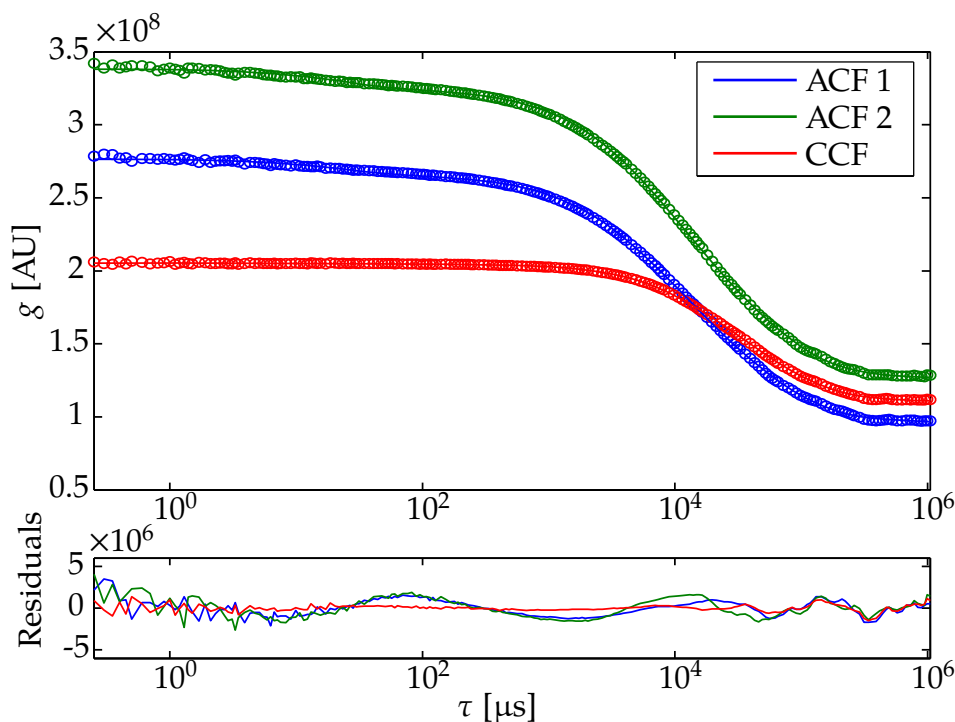


**Figure 2.20:** 2f-FCS experiment of vesicles extruded through 50 nm pore. Even without polarised detection, the rotational tumbling is already visible in the sub-ms range due to the finite focal volume.

$R_p$	$\langle R \rangle_N$	$\sigma_{R,N}$ [nm]	$\langle R \rangle_I$	$\sigma_{R,I}$	$D_{\text{FCS}}$ [ $\mu\text{m}^2 \text{s}^{-1}$ ]	$R_{\text{FCS}}$ [nm]
15	26.2	8.1	39.9	13.4	7.1(8)	30(4)
25	31.6	9.5	46.3	14.6	7.0(10)	31(5)
40	42.8	13.5	65.2	21.5	3.9(16)	55(23)
50	43.2	14.0	67.8	23.2	4.0(7)	53(9)
100	65.2	19.7	95.4	29.8	2.5(10)	86(35)

**Table 2.3:** Vesicle hydrodynamic radii determined from size distributions obtained by DLS and 2f-FCS.  $R_p$  is the extrusion pore radius,  $\langle R \rangle_N$  is the number-distribution averaged vesicle radius,  $\langle R \rangle_I$  is the intensity-distribution averaged radius, and  $R_{\text{FCS}}$  is determined by 2f-FCS.

### Translational lipid diffusion coefficient

The time-scales of translational vesicle and rotational vesicle plus translational lipid diffusion slightly overlap and have to be disentangled during analysis. This is done by fitting a stretched single-focus 3D-diffusion model to the slow time-domain and subtracting the outcome. One example of such a reduced correlation is shown in fig. 2.21.

While it is theoretically possible to obtain a direct estimate for the vesicle radius and measure the rotational diffusion within the same experiment, this is not done for

several reasons: Single-focus FCS has to be calibrated against a sample with a known diffusion coefficient but is still heavily influenced by optical aberrations as well as the size fluctuations inherent to the vesicles. Furthermore, the rotational diffusion measurements require a very large focal volume to impose an approximately flat excitation intensity profile. As such a modification makes it even harder to obtain a quantifiably robust estimate for the vesicle diffusion, it is used for correcting the curves only and no physical meaning is attached to the exponential coefficients.

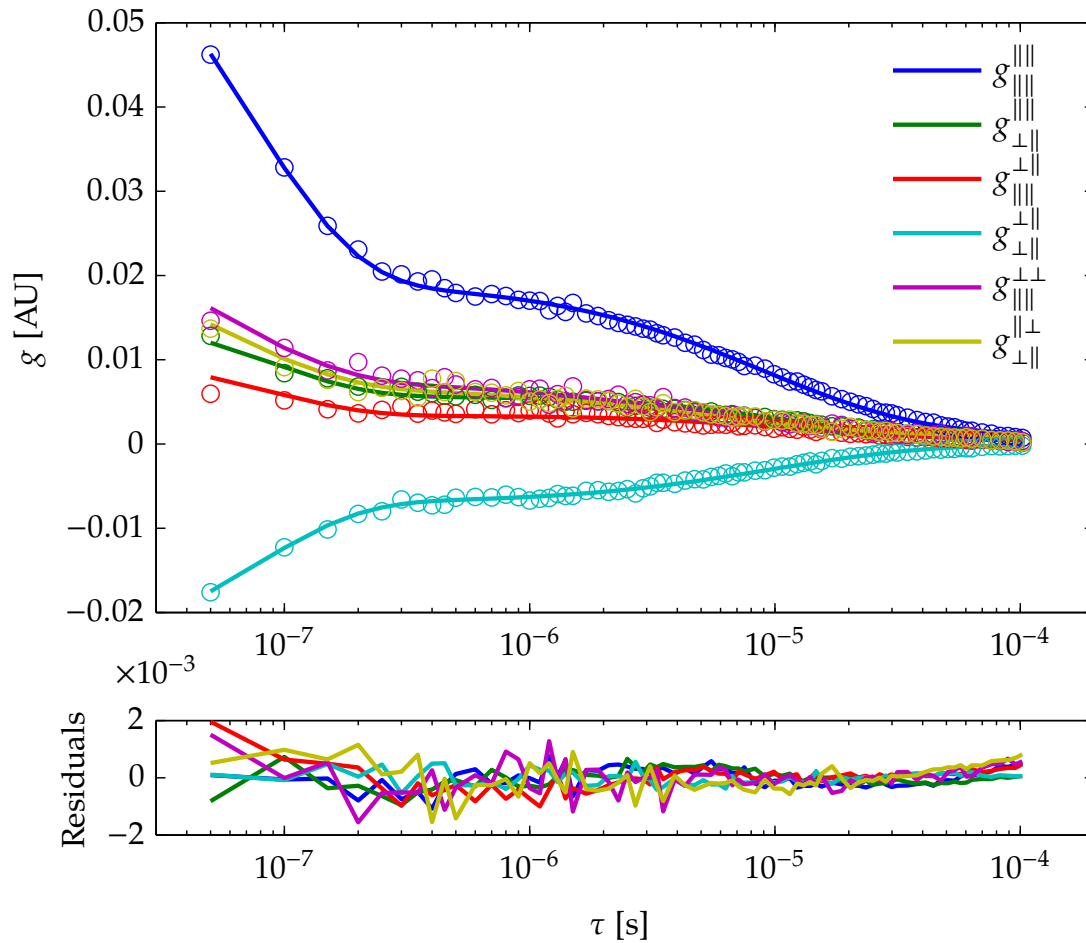


**Figure 2.21:** Polarisation-resolved FCS curves of  $R_p = 15$  nm vesicles. The correlation is performed from  $\tau_{\min} = 50$  ns to  $\tau_{\max} = 1$  s in this case and the diffusional correlation is subtracted. The rotational curves are then fitted up to  $\tau'_{\max} = 0.1$  ms.

Judging from the fit curves, the rotational diffusion model – shown here for  $R_p = 15$  nm vesicles – matches the correlation functions very well. Residuals stay below 5% and do not show any non-random fluctuation except near the vesicle diffusion range at which point the rotational part has almost completely decayed. The figure also shows how important it is in rotational diffusion measurements to have access to the complete set of correlation curves which are only available with a two-laser, four-detector setup.

Although the fit quality is remarkable, the same cannot be said about the diffusion coefficients  $D_{\text{trans}}$  obtained throughout the measurements plotted in fig. 2.22. Given the hydrodynamic radii acquired through 2f-FCS, it could be assumed that the true value for  $D_{\text{trans}}$  lies between the ones determined for the two distributions  $\varrho_I$  and  $\varrho_N$ . When comparing to the planar-limit diffusion coefficient from the GUV experiments, this concept holds up for the  $R_p = 15 - 25$  nm vesicles at best. The lipid diffusion coefficients of the larger vesicles are obviously systematically inflated, up to a factor of 10 in the case of the  $R_p = 100$  nm pore with  $\varrho_I$  as the size distribution. This picture is unaffected by the manner in which the vesicle radius is factored into the fitting function as demonstrated by fig. 2.22b. While it is not impossible to think of a mechanism that would allow lipids to diffuse faster in SUVs than GUVs, the magnitude of the deviation and the discontinuity necessary to explain the data are much too severe. The method's sensitivity in itself is adequate as evidenced by fig. 2.22c which shows the diffusion coefficient of  $R_p = 25$  nm liposomes at different temperatures. As expected, diffusion slows down for lower temperatures and begins to drop significantly when starting to approach the phase transition temperature. Cooling the sample down further was unfortunately prevented by condensation water forming around the tubing which could have damaged the electronics. Assuming sufficient precision, the accuracy could have been affected by a number of factors.

One of these is triplet state transition which happens on a similar time-scale as the diffusion processes and could seriously distort the correlation curves if not taken into account. Three things point against this: First, triplet transitions are intensity-dependent and the laser intensity was specifically adjusted to a very low level such that no triplet state could be detected in the GUV experiments. Next, the membrane dye DiD, which is known to exhibit photo-blinking in membranes even at low excitation, was also added to vesicles and analysed. The resulting correlation (fig. A.2), when fitted without a triplet model, clearly shows how difficult it would be to overlook an additional decay in the data, especially when it comes to the complete anti-correlation function  $g_{\perp\parallel}^{\perp\parallel}$ . Last, a triplet model added to the fit yields transition amplitudes below 0.1% and has no quantifiable influence on residuals or  $D_{\text{trans}}$ .

Another source of artefacts is depolarisation. Depolarisation refers to the possibility of both lasers not being completely linearly and orthogonally polarised with respect to each other due to defects in the dichroic mirror and transmission through the high-NA objective. In FCS, however, this mainly changes the relative amplitudes of all curves, not the time-scales [81], and would affect all vesicle sizes equally. A rather subtle effect that does in fact depend on the vesicle radius is the finite excitation volume: As has been mentioned, the laser beam before the objective is contracted to achieve a flat, widened excitation focus in the sample plane.

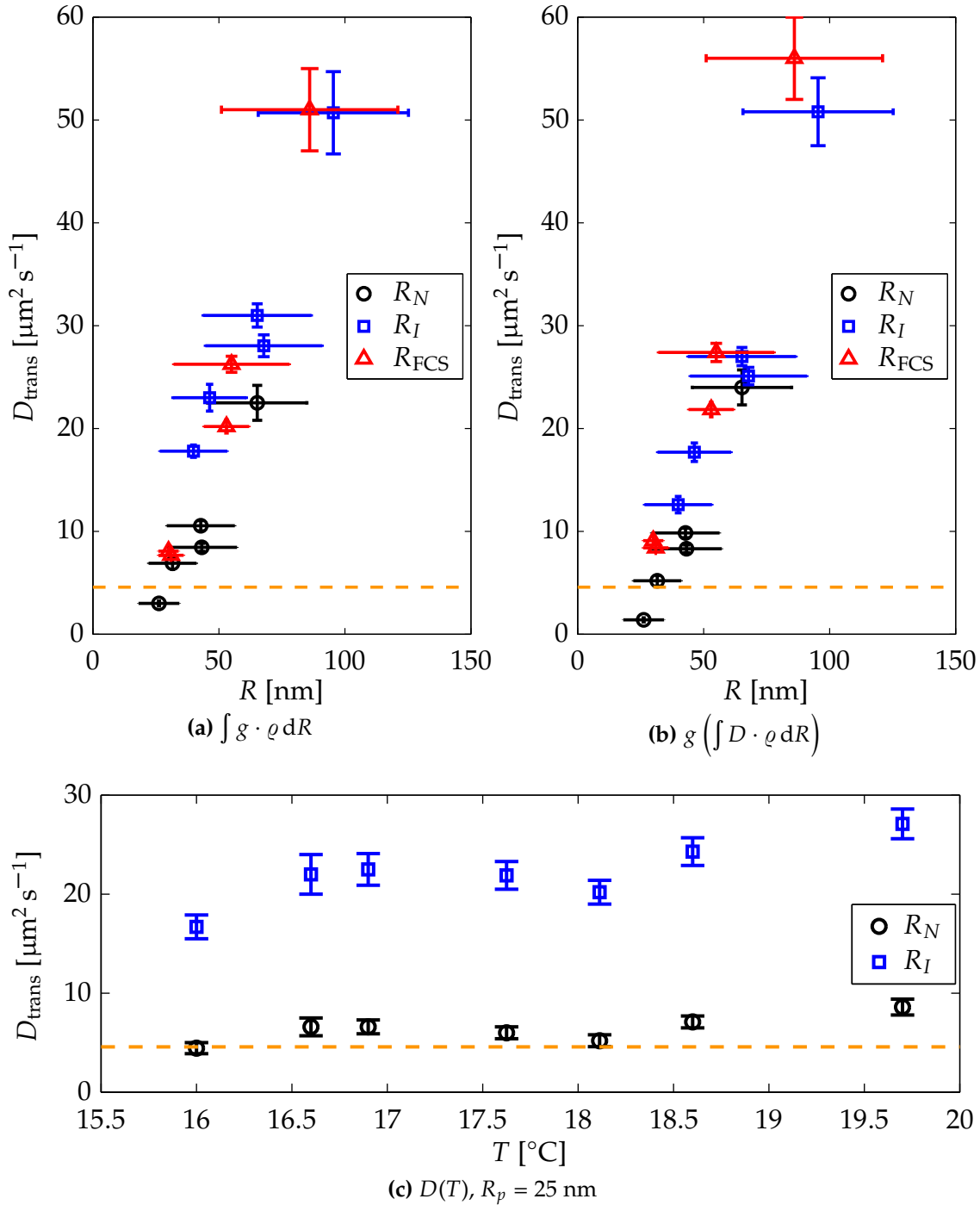


**Figure 2.22:** Lipid diffusion coefficient as a function of vesicle radius and temperature. **(a)** The complete correlation curves are integrated over the size distribution during fitting. The determined translational lipid diffusion coefficient is plotted against the average hydrodynamic radius of the respective size distribution. **(b)** The size-dependent diffusion coefficient  $D_{\perp}$  is integrated over the vesicle radius distribution instead of the whole correlation. **(c)** For a specific vesicle size (pore radius  $R_p = 25 \text{ nm}$ ), the sample temperature is varied over a small range to ascertain the method's sensitivity.  $R_N$  and  $R_I$  denote results obtained with the number and the intensity distribution, respectively. The dashed lines indicate the GUV diffusion coefficient.

---

This is done to ensure that the fluorescence intensity fluctuation during rotation or translation of the fluorophore will only depend on the orientation of the dipole axis, not its position. As the time-scale of translational diffusion is much slower than rotational diffusion, this always holds true in the limit of a point-like particle. A larger vesicle situated at the edge of the focal volume, however, would experience a significant excitation intensity gradient. This gradient would translate into an additional term in the correlation curve with a time-scale  $\tau_I \sim \tau_{\text{rot}}$  whose amplitude mainly depended on vesicle radius and laser beam waist. For a near-infrared Gaussian laser beam 1 mm in diameter, the intensity plateau in the sample plane is about 2  $\mu\text{m}$  wide. Again, this makes itself felt mostly for the  $R_p = 100$  nm vesicles and is not, by itself, sufficient to cause such large deviations.

The biggest influence on  $D_{\text{trans}}$ , and thus the largest potential source of errors, is obviously the size distribution. However, given the accuracy of 2f-FCS and DLS experiments, together with the reproducibility of vesicle preparation by extrusion, it seems rather implausible that the real vesicle radius would be much lower than all of the measurements suggested. Disregarding unknown issues with the measurement setup, there is unfortunately no concrete evidence at the time of writing which could explain the anomalous results.



## CHAPTER 3

# TrackNTrace

In this thesis, single particle tracking (SPT) is frequently relied upon to measure diffusion coefficients in bilayers and collect intensity traces of surface-bound molecules for photo-physical analysis. Since its introduction as “nanovid microscopy” in 1985 [96], SPT has become an important tool in the life sciences to study cellular dynamics. Particle tracking relies on localising fluorescent emitters within a movie and subsequently linking them in an automated fashion to form trajectories. Parameters such as diffusive speed or velocity can be readily extracted from these trajectories which in turn inform about binding kinetics, local geometry, or viscosity, to name a few examples. In addition to position and intensity, criteria such as size, shape, or direction of motion can determine if two particles at different points in time should be connected, increasing the demand for ever more sophisticated programs.

The list of software packages to choose from and features to be supported has been steadily growing to a point where researchers may find it difficult to select a program most suited to their needs. While comparative meta-studies have sought to remedy this problem to some degree [63], selecting the best algorithm for a given dataset is often cumbersome for scientists. Being implemented in low-level programming languages most of the time, adding features or adapting routines to the task at hand is often very challenging or even impossible in the case of closed-source software. Inspecting results to trace the effect of parameter changes is further complicated by poor visualisation interfaces which are often limited to only show a histogram of localisations or a list of trails. Thus, missed emitters, wrongly connected tracks, or prematurely ending trajectories can easily go unnoticed.

When my colleague Simon Christoph Stein faced similar difficulties in his single-molecule localisation microscopy (SMLM, [97]) studies, we decided to collaborate on a software project which would address these issues. The result is TrackNTrace [1], a plugin-based framework for single molecule localisation and tracking applications.

The software is designed to allow the rapid integration of existing algorithms for detecting, fitting, or tracking single molecules with minimal effort through automated integration in the TrackNTrace graphical user interface (GUI). TNT is implemented in MATLAB, a high level programming language that simplifies prototyping and is popular within the life sciences. In addition to its own algorithms, which are designed to be robust and fast, TNT also includes state-of-the-art localisation and tracking methods previously released as standalone software for MATLAB. A built-in preview function allows processing sections of a movie with the results being displayed superimposed on it. This greatly facilitates parameter optimisation and comparative studies, and makes it easy to develop and test new ideas. TNT also supports general image processing plugins to permit the seamless integration of, for example, non-localisation based super-resolution methods such as super-resolution optical fluctuation imaging (SOFI). TrackNTrace is freely distributed as open source and is available at <https://github.com/scstein/TrackNTrace>.

In this chapter, the general structure, user interface, and plugin system of TNT will be presented alongside a detailed explanation of the algorithms involved. The performance of TrackNTrace is then evaluated on simulated and experimental data. The chapter concludes with a short summary of side projects I conducted which relied on TNT for data processing.

Parts of this chapter are closely based on and expand upon the original TrackNTrace paper published in:

S. C. Stein and J. Thiart. 'TrackNTrace: A simple and extendable open-source framework for developing single-molecule localization and tracking algorithms'. *Scientific Reports* **6** (1) 2016 [1].



## 3.1 Materials & Methods

### 3.1.1 Framework composition & plugin system

The TrackNTrace framework consists of four principal analysis stages: First, the movies can be corrected for artefacts and the analogue-digital-converter counts of the camera converted to photon numbers. Next, any signal sources above a certain background threshold are identified to obtain a position list of so-called candidate detections. Based on these rough estimates, more accurate information is collected for each candidate in the refinement stage, including subpixel position or particle shape. Finally, all positions are connected frame-by-frame in the tracking step to retrieve the molecules' trajectories, if needed.

After starting the program and defining a list of movies to evaluate, the user is directed to an input mask as shown in fig. 3.1. Here, all parameters pertaining to the current movie and set of chosen plugins are entered. The preview button opens a visualiser where results for a small portion of a movie, generated with the current settings, can be inspected. A manual review of this data can easily reveal undetected molecules, badly fitted emitters, or prematurely ending tracks. By repeatedly switching between input mask and preview, all variables can be optimised until the result is deemed satisfactory. The user can then advance to the next movie or carry over the current settings for all remaining films. Eventually, the evaluation starts and the complete output is saved in a .mat file which contains the results alongside all utilised plugins and their respective parameters. The data can be inspected with the visualiser or post-processed using various functions, e.g. for drift correction, localisation histogramming, or diffusion coefficient estimation.

TrackNTrace plugins are defined in a single .m file and contain a header and the parameters to be manipulated in the GUI. The header specifies the functions to execute before, during, and after the analysis as well as plugin name, type, and description. The input variables – e.g. float or string – are initialised by default value, tooltip, and range where appropriate. The accompanying help text is mandatory so that users unfamiliar with the inner workings of a plugin are nonetheless able to use it. From this layout, an entry in the input mask is automatically generated without requiring any further assistance by the user or knowledge about the interface. In accordance with this simple structure, writing a plugin for TNT is designed to be as straightforward as possible. If an output function such as a PSF fitter is already available, translating it into a TNT plugin can be achieved with only a dozen lines of code. Thus, even programming novices can test and develop their own applications with TrackNTrace.

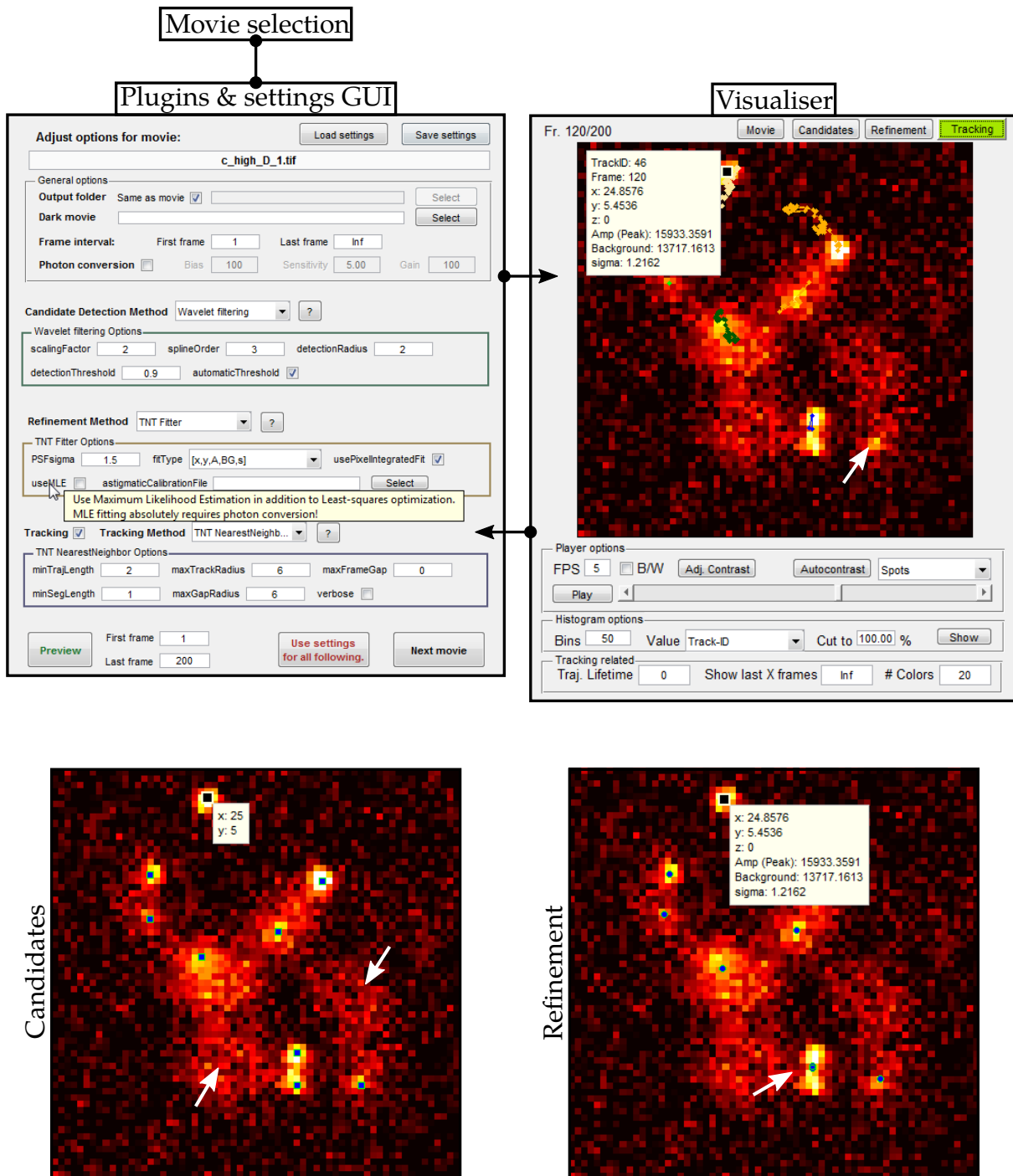


**Figure 3.1:** TrackNTrace input and visualiser GUI. For each movie, a different set of plugins and parameters can be specified and the input GUI is rebuilt accordingly, with each parameter having its own tooltip. A preview based on the current settings can be inspected in the visualiser, where unsuitable settings or algorithms can be quickly identified by the faulty output they produce (indicated by arrows). This allows adjusting all settings to the user’s satisfaction. Either the next movie is loaded or given inputs are used for the complete movie stack.

### 3.1.2 Algorithms & developed plugins

TrackNTrace is being delivered with a variety of different plugins to choose from for each of the three main processing stages – candidate detection, refinement, and tracking. While some functions have merely been ported to TrackNTrace from previously published MATLAB software packages, most of them have been specifically created by Mr. Stein and myself. This section will give a detailed overview of these scripts. A list of all currently available plugins is given in tab. 3.1.

Name	Type		Description
Cross-correlation	Candidate	O	PSF template matching
Defocused patterns	Candidate	P	Defocused dipole pattern matching [98]
Defocused refinement	Refinement	O	See above
Gauss-2D-Circ	Refinement	P	PSF matching by matrix inversion [99]
Image filtering	Candidate	O	Multi-purpose image filtering
GPU-Gauss MLE	Refinement	P	PSF fitting in C & CUDA [100]
<i>p</i> -value filtering	Candidate	O	Hypothesis-test-based thresholding
Radial symmetry	Refinement	P	Radial-symmetry-based centroid estimation [101]
TNT fitter	Refinement	O	PSF fitting using ceres library [102]
TNT z-Calibration	Refinement	O	Astigmatic imaging calibration
TNT NearestNeighbor	Tracking	O	Nearest-neighbour tracking
u-Track	Tracking	P	Global optimum tracking [103]
Wavelet filter	Candidate	O	Wavelet filtering

**Table 3.1:** List of TrackNTrace plugins. “P” indicates ported plugin, “O” previously unavailable and/or original contribution.

#### Cross-correlation

The patterns of sub-diffraction-sized emitters distributed in the microscope’s field of view closely resemble its point spread function. Then, the image correlation between patches containing such an emitter and the PSF should be relatively high whereas the noisy background would not appear correlated at all. Cross-correlation can thus be used to roughly estimate the positions of possible signal sources. The two-dimensional in-focus PSF of a microscope can be well-approximated by a symmetric Gaussian function

$$p_1(x, y) = \exp\left(-\frac{(x - \mu_x)^2}{2\sigma_{\text{PSF}}^2} - \frac{(y - \mu_y)^2}{2\sigma_{\text{PSF}}^2}\right), \quad (3.1)$$

where  $\sigma_{\text{PSF}} = \lambda/(4\sqrt{\log 2} \text{NA})$  and  $\lambda$  is the emission wavelength. Alternatively, a pixel-integrated Gaussian can be chosen instead which more closely resembles the actual

experiment where emitted photons impact upon the camera chip's pixel grid. It is given by integrating the above expression over the area of a single pixel which is assumed here to have a fill factor of 100%:

$$\begin{aligned}
 p_2(x, y) &= \int_{-1/2}^{+1/2} dx \int_{-1/2}^{+1/2} dy p_1(x, y) \\
 &= \frac{\pi \sigma_{\text{PSF}}^2}{2} \left[ \operatorname{erfc} \left( -\frac{x - \mu_x + 1/2}{\sqrt{2} \sigma_{\text{PSF}}} \right) - \operatorname{erfc} \left( -\frac{x - \mu_x - 1/2}{\sqrt{2} \sigma_{\text{PSF}}} \right) \right] \times \\
 &\quad \left[ \operatorname{erfc} \left( -\frac{y - \mu_y + 1/2}{\sqrt{2} \sigma_{\text{PSF}}} \right) - \operatorname{erfc} \left( -\frac{y - \mu_y - 1/2}{\sqrt{2} \sigma_{\text{PSF}}} \right) \right]
 \end{aligned} \tag{3.2}$$

Using one of these patterns with  $\mu_x = \mu_y = 0$ , one can calculate the normalised cross-correlation between the image  $I(x, y)$  and the  $(2n + 1) \times (2n + 1)$  pixel pattern  $p(x, y)$ :

$$\begin{aligned}
 \text{NCC}(x, y) &= \frac{1}{(2n + 1) \sqrt{\langle p(x, y) - \langle p(x, y) \rangle \rangle^2}} \times \\
 &\quad \sum_{i=-n}^n \sum_{j=-n}^n \frac{(I(x + i, y + j) - \langle I(x + i, y + j) \rangle_{ij}) p(x + i, y + j)}{\sqrt{\langle I(x + i, y + j) - \langle I(x + i, y + j) \rangle_{ij} \rangle_{ij}^2}} .
 \end{aligned} \tag{3.3}$$

By this definition,  $\text{NCC}(x, y) \in [-1, 1]$ . In regions containing a point-source emitter, the cross-correlation with the Gaussian template will be significant whereas pixels which only represent background noise will show a correlation close to 0. The pixel centres of all emitters above a certain threshold are determined by grayscale image dilation with a structuring element  $S$ :

$$I_{\text{dilated}}(x, y) = \max_{(i, j) \in S} \{I(x - i + n, y - j + n) + S(i, j)\} \tag{3.4}$$

$S$  is simply a  $(2n + 1) \times (2n + 1)$  matrix of ones. Therefore, in every  $(2n + 1) \times (2n + 1)$  neighbourhood, the dilated image will show elevated values except for a point where  $I_{\text{dilated}}(x_l, y_l) = I(x_l, y_l)$  which is the local maximum of its respective neighbourhood. Both cross-correlation and image dilation are directly implemented in the MATLAB image processing toolbox, thus being high-performance.

The coordinates of all local maximums above a certain threshold  $c_{\text{thresh}}$  are returned as candidates. The user can choose  $c_{\text{thresh}}$ ,  $\sigma_{\text{PSF}}$ , and  $n$ , as well as the pattern model.

### Defocused patterns & refinement

The defocused image of a fluorophore heavily depends on its emission dipole orientation. Applications such as metal-induced energy transfer depend upon the precise knowledge of this orientation. Recording a large number of molecules at the same time

and matching the defocused patterns to theoretical templates is the fastest way to perform such control measurements.

The TrackNTrace implementation is based on code published by Jörg Enderlein [98] which serves as the foundation for calculating the theoretical patterns. The user can specify the necessary microscope parameters (magnification, NA, emission wavelength, camera pixel size, focal distance) as well as the angular step size of the radial and azimuthal dipole angles. The original code is massively sped up by using cross-correlation for template matching as discussed above, and allowing the program to save and re-use patterns if no settings are changed.

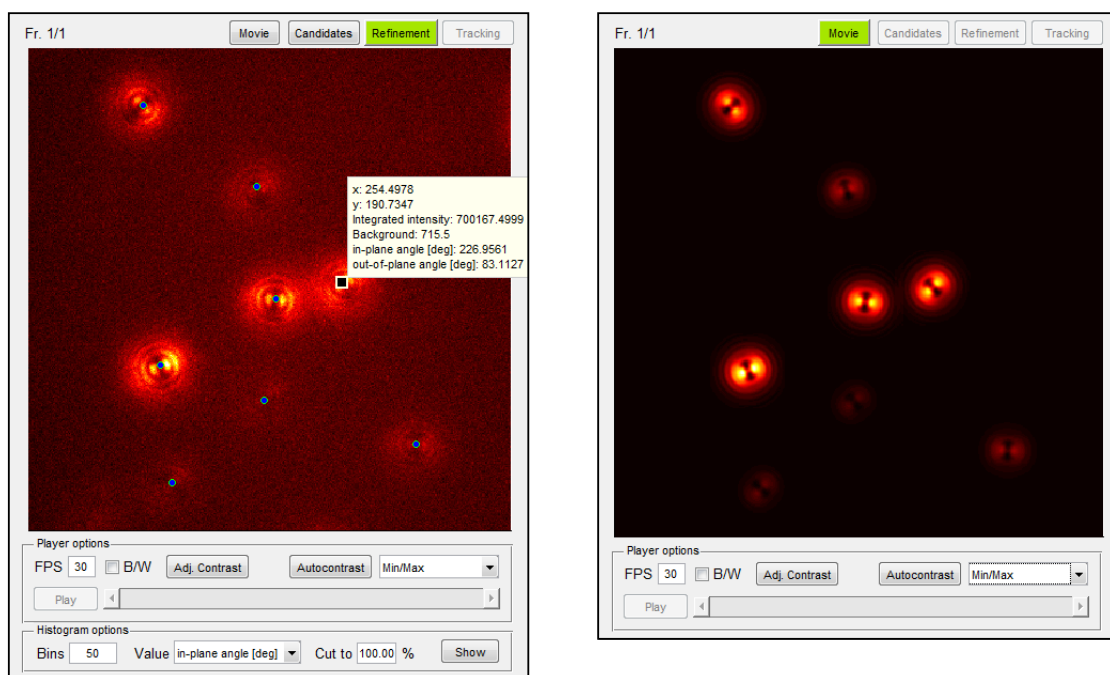


**Figure 3.2:** Defocused pattern fitting in TrackNTrace. The right panel shows the fitted final templates (Supplementary Figure 2 [1], data provided by Narain Karedla).

If necessary, the preliminary results can be passed on to a refinement routine which uses the candidate data as initial guesses for a custom conjugate-gradient solver. Here, patterns are fitted to smaller subimages around the emitter centroids either by least-squares or maximum-likelihood optimisation. The refined templates can be visually inspected by the user as depicted in fig. 3.2.

### Image filtering

The idea of microscopy image filtering in general is to elevate intensity levels originating from actual emitters and suppress any background noise or spurious signals. All local

maximums above a certain intensity threshold typically set by the user are then counted as candidates. Many digital filtering techniques are linear operations which means they can be expressed by a convolution of the original  $n \times n$  image  $I$  with a  $k \times l$  filter kernel  $H$ :

$$I'(x, y) = I * H = \sum_{i=-\lfloor k/2 \rfloor + 1}^{\lfloor k/2 \rfloor + 1} \sum_{j=-\lfloor l/2 \rfloor + 1}^{\lfloor l/2 \rfloor + 1} H(i + \lfloor k/2 \rfloor, j + \lfloor l/2 \rfloor) \cdot I(x - i, y - j) \quad . \quad (3.5)$$

It is assumed that the image index starts at  $(1, 1)$ . Here, as in most cases,  $H$  is a symmetric  $k \times k$  matrix with  $k < n$ . In TrackNTrace, all linear filters are also separable, meaning they can be expressed by vector multiplication as  $H = \mathbf{h} \cdot \mathbf{h}^T$ . Then, instead of using one two-dimensional convolution, the operation can be decomposed into two one-dimensional convolutions

$$I'(x, y) = (I(x, y) * \mathbf{h}) * \mathbf{h}^T \quad , \quad (3.6)$$

reducing the number of operations from  $(nk)^2$  to  $2n^2k$ . Six different filter functions are available in TNT: Moving average, difference of averages, Gaussian, zero-mean Gaussian, difference of Gaussians, and median. Fig. 3.3 displays the actions of these filters on a typical microscopy image.

The moving average filter, also known as boxcar, is one of the most commonly used in signal processing. The vector kernel is simply a list of ones divided by the length,  $\mathbf{h}_{\text{avg}} = (1, 1, \dots, 1)/k$ . Higher pixel values appear dilated while noise is blurred out and deflated. By convolving the image with a larger averaging kernel of size  $p \times p$ ,  $p > k$ , and subtracting it from the first filtered frame, elevated intensities appear less dilated and the contrast is increased. This difference-of-average filter restores emitter shapes to more closely resemble the original image but can lead to more artefacts.

Gaussian blur is primarily used as a smoothing filter but in contrast to the moving average, it is circularly symmetric. The vector kernel is expressed as  $a \exp(-x^2/(2\sigma^2))$  where  $a$  is a normalisation constant and  $x \in [-\lfloor k/2 \rfloor, \lfloor k/2 \rfloor]$ . The window size is automatically chosen such that  $k = 2 \lceil 3\sigma \rceil + 1$ . Both the difference-of-Gaussians filter and the zero-mean Gaussian blur are modified versions which work similar to the difference-of-averages filter: High intensities are still elevated, but washed out features are subtracted to reduce dilation. The former works exactly as its averaging counterpart, while the latter is implemented with the kernel  $\exp(-x^2/(2\sigma^2)) - 1/k \sum_x \exp(-x^2/(2\sigma^2))$ .

The median filter is the only one in the list which cannot be expressed as a linear operation. Here, the intensity of each pixel pair  $(x, y)$  is replaced by the median value of all pixels in a  $k \times k$  neighbourhood. Again, local maximums are dilated but edges are preserved. Thus, the filter is most suited to images distorted by spurious noise such as hot pixels and similar artefacts.

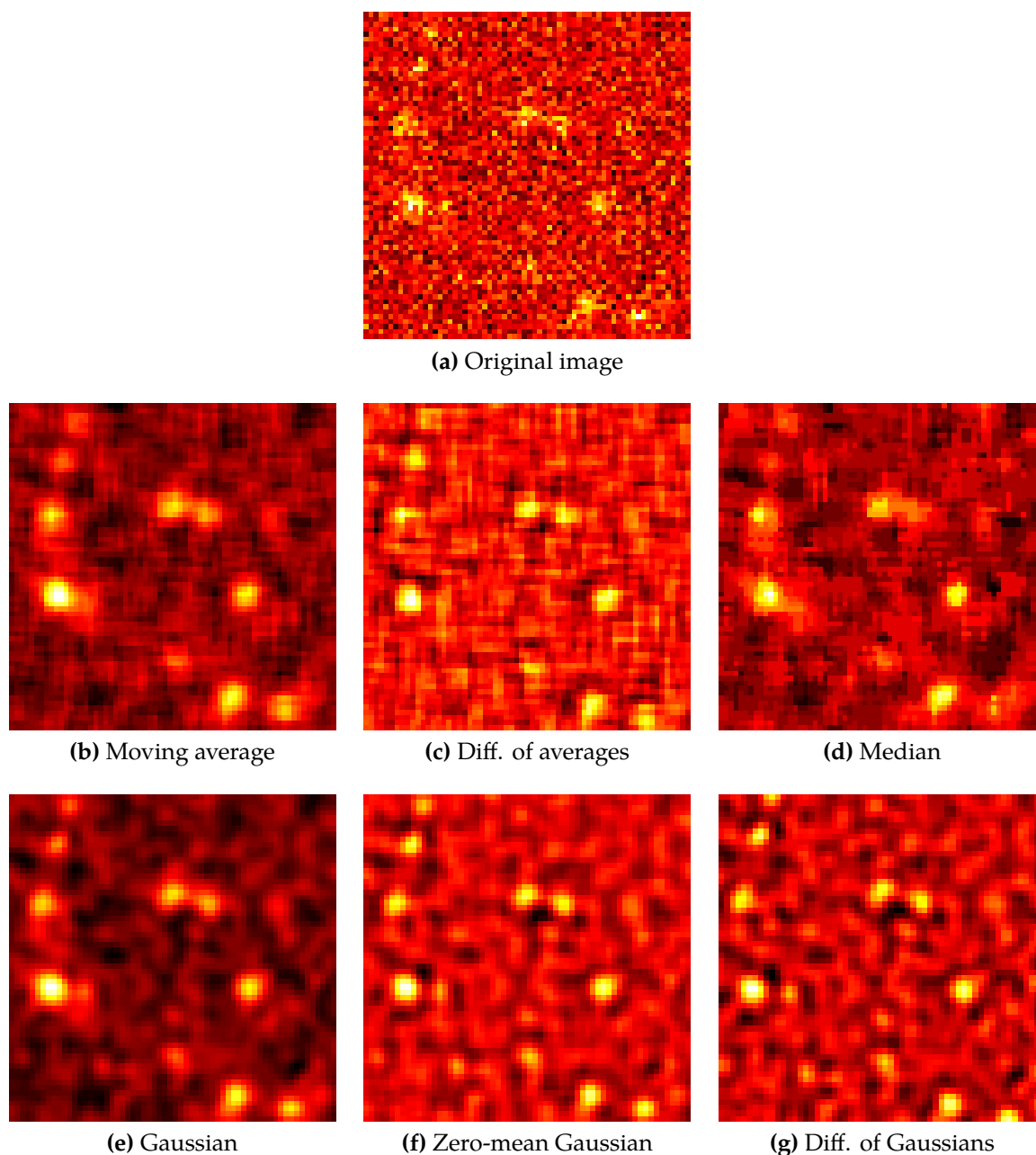


**Figure 3.3:** Examples of image filtering in TrackNTrace. All images were taken using the respective filter's default settings.

Molecule centroids in the filtered images are extracted by grayscale dilation with thresholding as explained above. The user can determine the size of the normal and enlarged windows,  $\sigma$ , as well as local maximum search radius and detection threshold.

### ***p*-value filtering**

The noisy background in a fluorescence microscopy image is a complex combination of Poisson shot noise, camera chip artefacts, read-out noise, and other sources. In most

cases, however, it can be well-approximated by a Gaussian distribution [104].  $p$ -value filtering, also called hypothesis filtering, is based on the concept of statistical hypothesis filtering. Here, both mean  $\mu_b$  and standard deviation  $\sigma_b$  of the local background of all pixels in an image are calculated approximatively. It is assumed that the intensity of any pixel in an emitter-free image originates from a Gaussian-distributed background  $\mathcal{N}(\mu_b, \sigma_b)$  which is the null hypothesis  $H_0$ . If a pixel violates this assumption at a confidence level  $p$ , that is  $\text{CDF}_{\mathcal{N}}(I(x, y, ), \mu_b, \sigma_b) > p$ , the null hypothesis is rejected ( $H_1$ ). The result is a binary map where clusters of ones are associated with fluorescent molecules. Any four-connected neighbourhood is counted as a cluster and its centroid position extracted to be used as an emitter candidate. The user can specify  $p$  and the minimum cluster size in addition to the frequency at which the local background is determined. The latter is based on a least-median squares routine [105].

### TNT fitter

After candidate detection, a model PSF can be fitted to a small image window around every estimated position to retrieve additional, refined parameters. In most cases, the subpixel position and the background-corrected intensity are sufficient, which can be used to create a localisation histogram of the data or perform particle tracking. In some cases, the particle shape is an equally important parameter if the PSF is being manipulated to encode additional information such as the sample's  $z$ -position. The TNT fitter supports 3D-localisation through astigmatic imaging by using an elliptic, rotated Gaussian as a PSF model:

$$G(x, y) = A \exp \left( - \left[ q_1(x - \mu_x)^2 + q_2(y - \mu_y)^2 - 2q_3(x - \mu_x)(y - \mu_y) \right] \right) + B \quad (3.7)$$

$q_i$  is related to the PSF standard deviations  $\sigma_{x,y}$  and the in-plane rotation angle  $\theta$  as follows:

$$q_1 = \frac{\cos^2 \theta}{2\sigma_x^2} + \frac{\sin^2 \theta}{2\sigma_y^2} \quad (3.8)$$

$$q_2 = \frac{\sin^2 \theta}{2\sigma_x^2} + \frac{\cos^2 \theta}{2\sigma_y^2} \quad (3.9)$$

$$q_3 = -\frac{\sin 2\theta}{4\sigma_x^2} + \frac{\sin 2\theta}{4\sigma_y^2} \quad (3.10)$$

While less intuitive at first, fitting  $\mathbf{q}$  instead of the original model parameters is preferable as it avoids divergences and is numerically more stable. The back-transformation



yields:

$$\theta = \frac{1}{2} \arctan \left( -\frac{2q_3}{q_2 - q_1} \right) \quad (3.11)$$

$$\sigma_x = \left( q_1 + q_2 - \frac{2q_3}{\sin 2\theta} \right)^{-1/2} \quad (3.12)$$

$$\sigma_y = \left( q_1 + q_2 + \frac{2q_3}{\sin 2\theta} \right)^{-1/2} \quad (3.13)$$

with  $\theta \in [-\pi/4, \pi/4)$ . If the angle is not optimised, the model reverts back to eqn. (3.1) or (3.2) with  $\sigma_x = (2q_1)^{-1/2}$  and  $\sigma_y = (2q_2)^{-1/2}$ . The minimisation is performed in C++ using the ceres-solver library [102]. Both Levenberg-Marquardt least-squares regression and maximum likelihood estimation are available.

The routine can be further improved by calculating better initial guesses instead of relying solely on the estimates obtained during candidate detection. A straightforward approach is the use of image moment analysis. Assuming a background-subtracted  $k \times k$  image  $I$ , image moments are defined by the equation

$$M_{mn} = \sum_{i=0}^{k-1} \sum_{j=0}^{k-1} i^m j^n I(i, j) \quad (3.14)$$

The first order moments simply return the centroid intensity while higher order moments are related to eccentricity, skewness, or scale. More information can be extracted by constructing the covariance matrix  $\Sigma$ ,

$$\Sigma = \begin{pmatrix} M'_{20} - (M'_{10})^2 & M'_{11} - M'_{10}M'_{01} \\ M'_{11} - M'_{10}M'_{01} & M'_{02} - (M'_{01})^2 \end{pmatrix} \quad \text{with} \quad M'_{mn} = M_{mn}/M_{00} \quad (3.15)$$

whose eigenvectors represent the two major intensity axes of the image and whose eigenvalues  $\lambda_{1,2}$  correspond to  $\sigma_x$  and  $\sigma_y$ . The angle of rotation is then given as the angle between the eigenvector with the largest eigenvalue towards the nearest axis. For a Gaussian pattern, one obtains

$$\theta = \frac{1}{2} \arctan \left( \frac{2\Sigma_{12}}{\Sigma_{11} - \Sigma_{22}} \right) \cdot \text{sign}(\Sigma_{11} - \Sigma_{22}) \quad (3.16)$$

$$\sigma_x = \left( \text{Tr}(\Sigma)/2 + \text{sign}(\Sigma_{11} - \Sigma_{22}) \sqrt{(\text{Tr}(\Sigma))^2/4 - \text{Det}(\Sigma)} \right)^{-1/2} \quad (3.17)$$

$$\sigma_y = \left( \text{Tr}(\Sigma)/2 - \text{sign}(\Sigma_{11} - \Sigma_{22}) \sqrt{(\text{Tr}(\Sigma))^2/4 - \text{Det}(\Sigma)} \right)^{-1/2} \quad (3.18)$$

Through careful starting parameter estimation, multi-threading, and the computational speed advantage of C++ over MATLAB, the TNT fitter is able to fit close to  $10^6$  emitters per second<sup>1</sup> which is sufficient for large-scale localisation microscopy experiments.

<sup>1</sup>This estimate is based on a standard office PC with a Core i7-3770 CPU.

The user has to provide an initial value for  $\sigma_{\text{PSF}}$  and can choose the fit model (symmetric, elliptic, or rotated, and pixel or pixel-integrated) as well as the fitting algorithm (least-squares minimisation with optional maximum likelihood estimation).

### TNT NearestNeighbor

Nearest-neighbour tracking (NNT) is the most common form of automated single particle tracking. For every position  $\mathbf{r}_i$  at time  $t$ , an associated position  $\mathbf{r}_j$  at time  $t + \Delta t$  is sought which fulfils  $\|\mathbf{r}_i - \mathbf{r}_j\| = r_{ij} \leq r_{\text{max}}$ , where  $r_{\text{max}}$  is a user-supplied variable. The positions are paired into a set of trajectories  $T_k = \{\mathbf{r}_{1k}, \dots, \mathbf{r}_{ik}, \mathbf{r}_{jk}\}$  subject to the constraint

$$T_k \cap \mathbf{r}_j \mid \min_{i,j} \left\{ \sum_i \sum_j r_{ij} \right\} . \quad (3.19)$$

If no nearest neighbour for particle  $i$  is found, the trajectory  $T_k$  ends and  $\mathbf{r}_j$  is the start of a new one.

For Brownian particles, seeking the global minimum of eq. (3.19) over all frames and all possible particle combinations yields the optimal trajectory set. In practice, this is only rarely done due to the computational demand imposed by the combinatorics involved and the limitations of Brownian diffusion models. Typically, nearest-neighbour tracking is performed frame-to-frame and reserved to simplistic scenarios with low particle densities, low mobility, or high time resolution. The TrackNTrace NNT plugin is implemented in the same frame-to-frame fashion using  $kd$ -tree traversal implemented in C++ via the nanoflann library [106]. The function can handle millions of localisations almost instantaneously and thus serve as a precursor to more sophisticated tracking algorithms. The plugin can also handle blinking fluorophores which are temporarily invisible by re-tracking all trajectories from the first part of the analysis. If a molecule vanishes but reappears in a later frame, the tracker tries to link the end of the first trajectory and the start of the second one. If the two segments of minimum length  $l_S \leq l_T$  are closer than a specified distance  $r_{\text{gap}}$  in space and  $t_{\text{gap}}$  in time, they are recombined into a single trajectory. The user can change  $r_{\text{max}}$  and the minimum allowed trajectory length  $l_T$  as well as  $r_{\text{gap}}$  and  $t_{\text{gap}}$ .

### Wavelet filter

The wavelet transform is a spatial frequency band-pass filter. By continuous removal of lower frequency components, differently sized features are elevated depending on

the number of filtering passes. It is recursively defined as:

$$W_i = F_{i-1} - F_i \quad (3.20)$$

$$F_i = \begin{cases} I & \text{if } i = 0, \\ (F_{i-1} * \mathbf{h}_i) * \mathbf{h}_i^T & \text{otherwise.} \end{cases} \quad (3.21)$$

Here,  $W_i$  is the wavelet image,  $\mathbf{h}_i$  is a low-pass filter kernel, and  $F_i$  is the respective filter image. The first wavelet level contains only high-frequency components such as noise while the lower levels are composed of increasingly larger features. The specific implementation relies on choosing the right low-pass filter and the best wavelet level to use for feature extraction. Izeddin et al. [107] suggest an “à trous” wavelet algorithm of second order using upsampled B-spline kernels recursively defined in the following way:

$$B_1(x) = \begin{cases} 1 & \text{if } 0 \leq x < 1, \\ 0 & \text{otherwise.} \end{cases} \quad (3.22)$$

$$B_m(x) = \frac{x}{m-1} B_{m-1}(x) + \frac{m-x}{m-1} B_{m-1}(x-1) \quad (3.23)$$

The initial filter kernel is then calculated as  $\mathbf{h}_1(j) = a^{-1} B_m\left(\frac{2j-k-1+sm}{2}\right)$ , where  $i \in [1, k]$ ,  $k = 2 \lceil sm/2 \rceil - 1$ , and  $a$  is a normalisation constant.  $m \in \mathbb{N}^+$  is the spline order and  $s \in \mathbb{R}^+$  is a scaling factor. Higher order kernels are constructed by inserting zeros between the coefficients.  $m = 3$  and  $s = 2$  are the default values to be changed by the user on request.

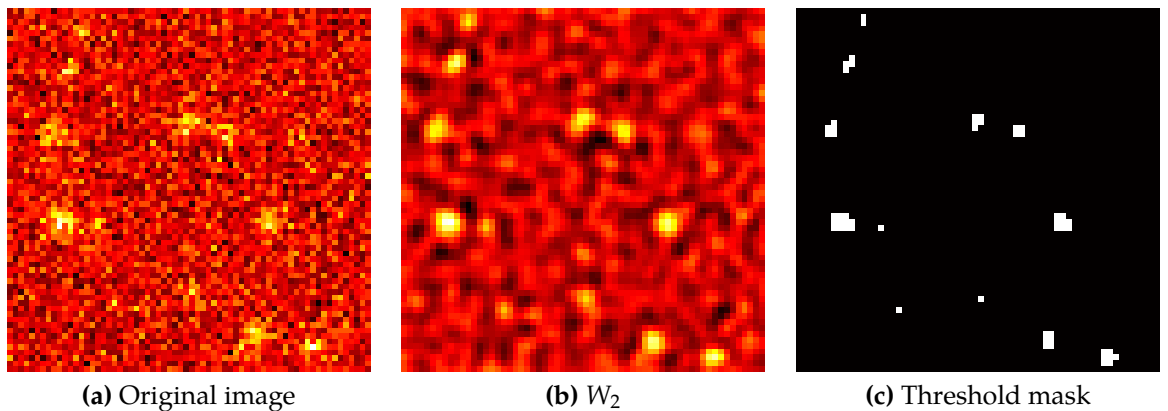


**Figure 3.4:** Wavelet filtering in TrackNTrace. The images are created with the default settings ( $t = 0.9$ ,  $m = 3$ ,  $s = 2$ ).

One of the great advantages of using wavelet filtering for particle candidate identification is its capability of automated intensity thresholding. As the first wavelet level

is essentially feature-free, it can be exploited for background estimation. More specifically, only local maximums fulfilling the condition  $W_2(x, y) > t\sigma(W_1)$  are accepted as candidates where  $\sigma$  is the standard deviation of all intensity values and  $t$  is a user-specified variable which should be close to 1. Since  $W_1$  is calculated for each frame, the threshold is updated with it at no cost in performance. This property is especially useful for movies where the background changes on relatively short time-scales. Fig. 3.4 shows the filter in action.

### 3.1.3 Performance evaluation

The main focus of TrackNTrace as a framework lies on the integration and development of localisation and tracking algorithms. It is nevertheless important to compare it to established software to validate its suitability for common applications. As any challenging particle tracking scenarios can be handled by a plugin version of u-Track, which has been extensively benchmarked by its original authors [103], the evaluation focuses on localisation microscopy only. Three programs – TrackNTrace, rapidSTORM [108], and ThunderSTORM [109] – were examined in simulations and TNT was tested on two biological samples.

#### Simulation

Simulated fluorescence microscopy movies were created by randomly distributing sub-diffraction-sized emitters on a Siemens star object with  $n$  arms assuming imaging conditions typical for localisation microscopy as described previously [110]. The particle density was fixed at  $\varrho = 7.5 \text{ pixel}^{-1}$  and emitter positions  $\mathbf{r} = (\mu_x, \mu_y)$  were drawn from a uniform distribution such that the condition  $\cos(\arctan(\mathbf{r} \cdot \mathbf{n})) > 0$  was fulfilled. Blinking was implemented by drawing a random number of activation events from a Poisson distribution  $\text{Poiss}(k_{\text{ac}}n_{\text{frames}})$  and obtaining the active-state duration from an exponential distribution  $\text{Exp}(k_{\text{deac}})$ . If the blinking cycles reached a maximum of  $n_{\text{bleach}} = 1 + \text{Geom}(p_{\text{bleach}})$ , the respective emitter was considered bleached.  $\text{Geom}(x)$  refers to the geometric distribution with probability density  $\rho(p) = (1 - p)^{k-1}p$  for  $k$  trials and event probability  $p$ . The rates were coupled to ensure a sufficiently sparse set of fluorescing molecules in each frame,

$$k_{\text{deac}} = k_{\text{off}} + k_{\text{bleach}} \quad (3.24)$$

$$k_{\text{ac}} = \left( \frac{1}{k_{\text{deac}}} + \frac{1}{k_{\text{on}}} \right)^{-1} \quad (3.25)$$

$$p_{\text{bleach}} = \frac{k_{\text{bleach}}}{k_{\text{deac}}}, \quad (3.26)$$

with  $k_{\text{on}} = k_{\text{off}}/(5\rho)$ ,  $k_{\text{off}} = 1 \text{ frame}^{-1}$  and  $k_{\text{bleach}} = 0.15 \text{ frame}^{-1}$ . For each emitter and each frame, a normalised on-time amplitude  $A \in [0, 1]$  was calculated this way. The field of view was discretised as a  $256 \times 256 \text{ px}^2$  grid with a pixel size<sup>2</sup> of 100 nm. At each particle subpixel position, an integrated Gaussian  $AN \times g_m + B$  was added to the image where  $N$  is the maximum number of photons emitted by a fluorophore and  $g_m$  is the Gaussian mask from eq. (3.2) with a standard deviation of  $\sigma_{\text{PSF}} = \lambda/(4\sqrt{\log 2} \text{ NA})$ . For all simulations,  $\lambda = 670 \text{ nm}$ ,  $\text{NA} = 1.4$ , and  $N = 50$  were chosen, with the background  $B$  adjusted such that a signal-to-noise ratio (SNR) of 1 to 5 was achieved. The simulations were carried out for 1500 frames with typically  $3 \cdot 10^5$  emitters per movie and the end result was distorted by Poisson shot noise.

For the execution speed measurement, a rectangular array of  $16 \times 16$  emitters was evenly distributed on a  $512 \times 512 \text{ px}^2$  grid. The SNR was set to 10 to ensure every software would localise the same number of molecules regardless of the settings used. The movie frame was duplicated 3500 times for a total of 896,000 spots. The execution time was measured on a Dell Optiplex 7010<sup>3</sup> running on Windows 7x64 and was corrected for reading and saving any data.

### Analysis

All programs were operated with the same settings if possible, with a few exceptions. *rapidSTORM* lacks wavelet filtering and was run with a difference-of-averages filter instead. It also cannot fit an integrated Gaussian PSF by default. To provide optimal comparability, a number of different parameter values producing similar outputs were chosen and the result achieving the highest test scores was selected.

Three different quality scores were compiled for each software by comparing output data set  $\mathcal{L}_{\text{obs}}$  and ground truth  $\mathcal{L}_{\text{ref}}$ . These included the Jaccard index (JAC), the root-mean-square error (RMSE), and the Fourier ring correlation (FRC). The JAC indicates how well a localisation routine can detect actual emitters and distinguish them from background noise while the RMSE simply states how well the positions are fitted:

$$\text{JAC} = \frac{|\mathcal{L}_{\text{obs}} \cap \mathcal{L}_{\text{ref}}|}{|\mathcal{L}_{\text{obs}} \cup \mathcal{L}_{\text{ref}}|} = \frac{\text{TP}}{\text{TP} + \text{FP} + \text{FN}} \quad (3.27)$$

$$\text{RMSE}^2 = \frac{1}{\text{TP}} \sum_{i \in \mathcal{L}_{\text{obs}} \cap \mathcal{L}_{\text{ref}}} \left( \mu_{x,\text{obs}}^i - \mu_{x,\text{ref}}^i \right)^2 + \left( \mu_{y,\text{obs}}^i - \mu_{y,\text{ref}}^i \right)^2 \quad (3.28)$$

A correctly localised particle counts as a true positive (TP) whereas a false negative (FN) or a false positive (FP) does not appear in the experimental or the ground truth set, respectively.

<sup>2</sup>The unit "px" denotes the length of one pixel, not its area.

<sup>3</sup>Intel Core i7-3770 CPU, 16 GB RAM, SSDSC2CT180A4 drive.

The FRC as a resolution criterion stems from electron microscopy and was introduced to the super-resolution microscopy field by Nieuwenhuizen et al. [111]. It quantifies the spatial correlation between two subimages  $I_1$  and  $I_2$  of a structure in Fourier space:

$$\text{FRC}(q_r) = \frac{\sum_{|\mathbf{q}| \leq q_r} \hat{I}_1(\mathbf{q}) \hat{I}_2(\mathbf{q})}{\sqrt{\sum_{|\mathbf{q}| \leq q_r} |\hat{I}_1(\mathbf{q})|^2 \cdot \sum_{|\mathbf{q}| \leq q_r} |\hat{I}_2(\mathbf{q})|^2}} \quad (3.29)$$

$I_1$  and  $I_2$  are localisation histograms of  $\mathcal{L}_{\text{obs}}$  and  $\mathcal{L}_{\text{ref}}$  created at a tenth of the original pixel size. For increasing frequencies, which correspond to smaller features in real space, the FRC decreases until reaching a noise threshold. The image resolution is then given as the inverse spatial cutoff frequency  $(q_{r,\text{cut}})^{-1}$  where the FRC has dropped to a specific value. Many different possibilities of  $q_{r,\text{cut}}$  exist in literature. Here,  $\{q_{r,\text{cut}} \mid \text{FRC}(q_{r,\text{cut}}) = \text{FRC}(q_{\text{min}})/7\}$  was chosen as suggested in the original publication.

### 3.1.4 Biological examples

Apart from synthetic benchmarks, TrackNTrace was evaluated in two experimental scenarios, dSTORM imaging of  $\beta\text{IV}$ -spectrin in a mouse hippocampal neuron axon initial segment, and single particle tracking of lipids and proteins in a black lipid membrane.

#### dSTORM of $\beta\text{IV}$ -spectrin in mouse hippocampal neurons

The movie analysed in this thesis was recorded and provided by Melanie Dannemeyer. Both the microscope setup and sample preparation have been described in detail in her thesis [112]. Briefly, a hippocampal neuron extracted from a mouse brain matured for 11 days in vitro was fixed and immunolabelled against N-terminal  $\beta\text{IV}$ -spectrin. A secondary, Alexa647-conjugated antibody was added for fluorescence labelling. The cells were immersed in a STORM-compatible imaging buffer (10 mM TRIS, 100 mM cysteamine hydrochloride, 4 mg ml<sup>-1</sup> glucose oxidase, 0.57 mg ml<sup>-1</sup> catalase, and 10% glucose at pH = 8.4) and mounted on a coverslip. The fluorophores were excited with a 647 nm laser and a 100× UApoN TIRF-objective (NA = 1.49) in HILO mode and imaged onto a DU-885 EMCCD at an effective pixel size of 80 nm.

The resulting movie was evaluated with TrackNTrace and its cross-correlation and nearest-neighbour tracking plugins. The latter was employed to detect and discard clusters of molecules or dirt visible for longer than 25 frames. Defocused or dim emitters with a size deviation of  $\Delta_\sigma > 0.4$  px or signal-to-background ratio below 0.8 were likewise rejected. The remaining positions were assembled into a localisation histogram with a super-resolution pixel size of 10 nm.

### Diffusion in black lipid membranes

Black lipid membranes were created with a Bilayer Explorer system (*Ionovation, Germany*) by adding a 3 : 2 weight mixture ( $c_{\text{final}} = 10 \text{ mg ml}^{-1}$ ) of POPE and POPC dissolved in dodecane to the Explorer fluid channel chip which was filled with PBS (137 mM NaCl, 2.7 mM KCl, 1.5 mM  $\text{KH}_2\text{PO}_4$ , and 8.1 mM  $\text{Na}_2\text{HPO}_4$  at pH = 7.4). By repeatedly pumping the solution through a 120  $\mu\text{m}$  polytetrafluoroethylene pore, a stable bilayer with a diameter of 100  $\mu\text{m}$  was formed. DPPE, Cytochrome B5, and KcsA potassium channel monomers from *Streptomyces lividans* were expressed, labelled with Atto655, and added via direct addition as described before [113]. The lipids were bought from *Avanti, USA*.

Movies of diffusing particles were recorded on a custom-built wide-field setup assembled from a  $\lambda = 637 \text{ nm}$  CUBE diode laser (*Coherent, Germany*), a 60 $\times$  1.2 NA UPLS-APO water-immersion objective (*Olympus, Germany*), and an iXon3 DU-860D EMCCD (*Andor, Ireland*). To achieve high excitation rates, the laser light was focused on the back-focal plane of the objective with an  $f = 300 \text{ mm}$  lens, resulting in a small field of view 10  $\mu\text{m}$  in diameter. The emission light was collected through the same objective and focused onto the camera chip by an  $f = 200 \text{ mm}$  tube lens and a 3.33 $\times$  post-magnification system (MAP1030100-A, all optics by *Thorlabs, UK*). Imaging was performed at an acquisition rate of 950 Hz and an effective pixel size of 108 nm.

### Single particle tracking

The movies were analysed in TrackNTrace using wavelet filtering and the TNT fitter plugin. The determined positions were passed on to the nearest-neighbour tracker and the tracks visualised. Parameters such as particle size, maximum allowed particle-to-particle linking distance, and minimum trajectory length were optimised iteratively until the outcome was deemed satisfactory. These settings were transferred to the u-Track plugin which itself optimises these parameters through forward-backward Kalman filtering. As u-Track seeks a solution to a global optimisation problem instead of only linking adjacent frames, it is better equipped to deal with overlapping trajectories or particle motion heterogeneity. The results were interpreted by an MSD fit routine. Here, displacement vectors of each trajectory's  $N$  position vectors  $\mathbf{r}_i = (x_i, y_i)$ ,  $i = 1, \dots, N$  were calculated for all possible frame intervals  $\Delta t_{ij}$ :

$$\mathbf{d}_{ij} = \mathbf{r}_i - \mathbf{r}_j, \quad 1 \leq j < i \leq N \quad (3.30)$$

$$\Delta t_{ij} = (i - j) t_a \quad (3.31)$$

$t_a$  is the camera acquisition time. From this point, the displacements  $\{\mathbf{d}_{ij}\}$ ,  $i - j = k$  for one frame interval  $kt_a$  could be processed in three different ways: Calculate and fit

the MSD for each individual trajectory, average over all trajectories first and then fit, or perform MSD histogram analysis. Choosing the latter option, the displacements were binned into a single, normalised histogram and then fit for each time interval:

$$P(\mathbf{d}_k) = \sum_i \frac{w_i}{\left(\sqrt{2\pi\sigma_i^2}\right)^\nu} \exp\left(-\frac{|\mathbf{d}_k - \mathbf{v} \times kt_a|^2}{2\sigma_i^2}\right) \quad (3.32)$$

$$P(|\mathbf{d}_k|) = \sum_i \frac{w_i}{\sigma_i^2} |\mathbf{d}_k| \exp\left(-\frac{|\mathbf{d}_k|^2}{2\sigma_i^2}\right) , \quad (3.33)$$

where each diffusing species contributes to the histogram with a weight  $0 < w_i \leq 1$  and  $\sum_i w_i = 1$ . The bell curve histogram can be fitted for  $\nu = 1$  or 2 dimensions with and without a velocity component  $\mathbf{v}$ . If the diffusion is isotropic,  $x$ - and  $y$ -displacements can be pooled into a single data set which is advantageous if the statistics are inadequate. The jump distance distribution on the other hand is more sensitive to discrepancies in the data such as incorrectly chosen linking distance and noisy tracks. While  $i_{\max}$  can be chosen automatically through hypothesis  $F$ -testing, it was forced to 1 in this case. Diffusion was assumed to be isotropic with  $\nu = 1$  and the velocity taken as 0. The MSD values  $\sigma^2$  obtained from the histogram analysis were subsequently fitted to a line to extract the diffusion coefficient  $D$ :

$$\sigma^2(k) = 2Dkt_a + \varepsilon \quad (3.34)$$

$\varepsilon$  is a measure for the fit accuracy affected by the localisation uncertainty and finite camera exposure time [114].



## 3.2 Results

### 3.2.1 Performance evaluation

Although initially developed as a framework for testing and developing, TrackNTrace was ultimately designed as a fully-featured fluorescence imaging software. As a demonstration, its effectiveness in typical applications is evaluated and compared to two other well-established programs: *rapidSTORM*, a widely used standalone software for PALM and STORM, and ThunderSTORM, an ImageJ plugin which ranked first among several dozen SMLM software packages in a recent comparative meta-study [97]. Simulated fluorescence localisation microscopy movies of a Siemens star test structure were prepared and the localisation quality and execution speed of each software was assessed.

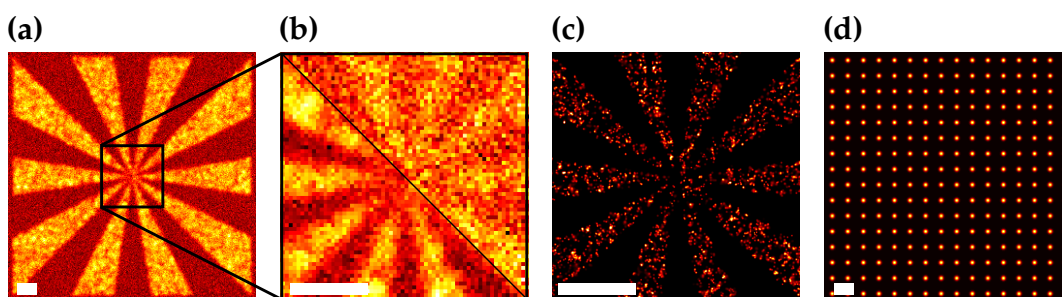


**Figure 3.5:** Simulated test structures for performance evaluation. (a) Sum intensity image of Siemens star test structure at an average SNR of 3. (b) Zoom-in of inner spoke region at SNRs of 1 (upper right) and 3 (lower left). (c) Reconstructed localisation histogram of the same region at SNR = 3 with Gaussian rendering using TrackNTrace with cross-correlation for candidate detection. (d) Execution speed test grid at SNR = 10. All scale bars correspond to a length of 2  $\mu\text{m}$ .

Fig. 3.5 shows an overview of the simulation course. If all frames of the movie are simply summed up, which represents a wide-field image of the structure, no details are visible, the edges are blurred out and the central spoke pattern is completely unresolved, especially at low signal-to-noise ratios (SNR). A super-resolved localisation image of the same region clearly reveals the amount of detail that was lost in the conventional recording and restores the core structure. The rendering style makes use of Gaussian re-weighting of all localisations. Here, a Gaussian PSF is added to the histogram instead of simply binning all positions. The emitter amplitude is proportional to the fit precision so that higher-quality localisations are represented to a greater extent in the reconstructed object. The result quality is examined by calculating the Jaccard index (JAC), root-mean-square error (RMSE), and the Fourier ring correlation (FRC). In the execution-speed test, emitters are distributed on a grid in a regular fashion and at a very high SNR of 10. As a consequence, the number of fitted positions becomes independent of the candidate

detection method, and the fit performance – which has the largest influence on execution speed – is emphasised. The respective graphs are displayed in fig. 3.6.

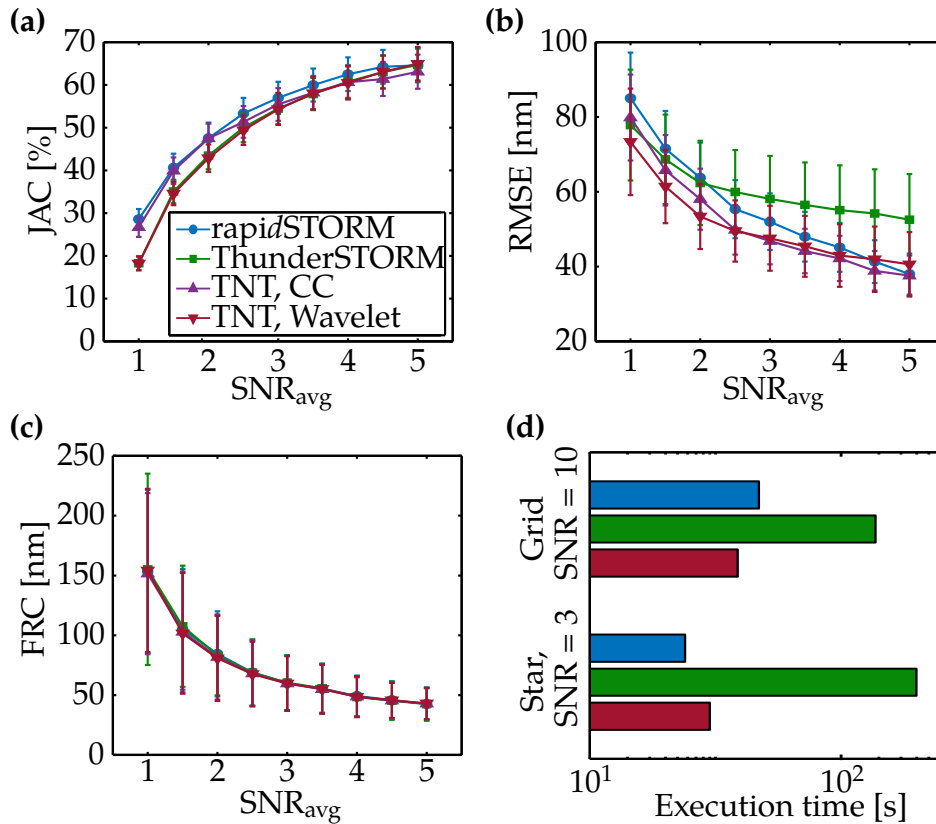


**Figure 3.6:** Simulation performance evaluation results. **(a–c)** Overview of simulation results: Jaccard index, root-mean-square error, and Fourier ring correlation of emitters localised with different programs at various average SNR levels. TrackNTrace is evaluated using wavelet filtering and cross-correlation for emitter candidate detection. **(d)** Execution time of programs on Siemens star and high-SNR emitter grid.

The Jaccard index, which almost completely depends upon the candidate detection method, suggests that wavelet filtering is less suited for lower SNRs whereas TNT’s cross-correlation and especially *rapidSTORM*’s difference-of-averages filter score consistently well across the whole SNR range. All curves saturate at a relatively low JAC of 0.65 which is understandable given the exponential emitter intensity distribution. These performance differences, however, do not directly translate into a corresponding change in fit accuracy when comparing JAC and RMSE. Here, *rapidSTORM* does not benefit from its higher detection efficiency and loses to TrackNTrace using either cross-correlation or wavelet filtering. This outcome suggests that a higher number of low-signal localisations tends to have negligible impact on resolution improvement. Regardless of these discrepancies, all software packages achieve virtually the same structural resolution which is given by the FRC. This result is unaffected by confining the FRC calculation to different parts of the Siemens star, meaning that the result is not

dominated by the layout of the structure itself. When it comes to execution speed, TrackNTrace is on par with *rapidSTORM* and even surpasses it on the high-SNR grid whereas ThunderSTORM takes an order of magnitude longer to finish. This comes as a surprise given that *rapidSTORM* is programmed exclusively in C++, a testament to TNT's efficiency. Overall, TrackNTrace performs on the same level as established programs and meets the demands currently imposed upon SMLM software.

### 3.2.2 Experimental examples

With TrackNTrace's performance in synthetic benchmarks proving to be satisfactory, the next logical step was to assess its viability in real experiments. Fig. 3.7 pictures the outcome of a dSTORM measurement from a mouse hippocampal neuron labelled with an Alexa647-tagged antibody against the N-terminus of  $\beta$ IV-spectrin. The movie, which depicts the tubular membrane of an axon initial segment, was recorded and kindly provided by Melanie Dannemeyer [112].

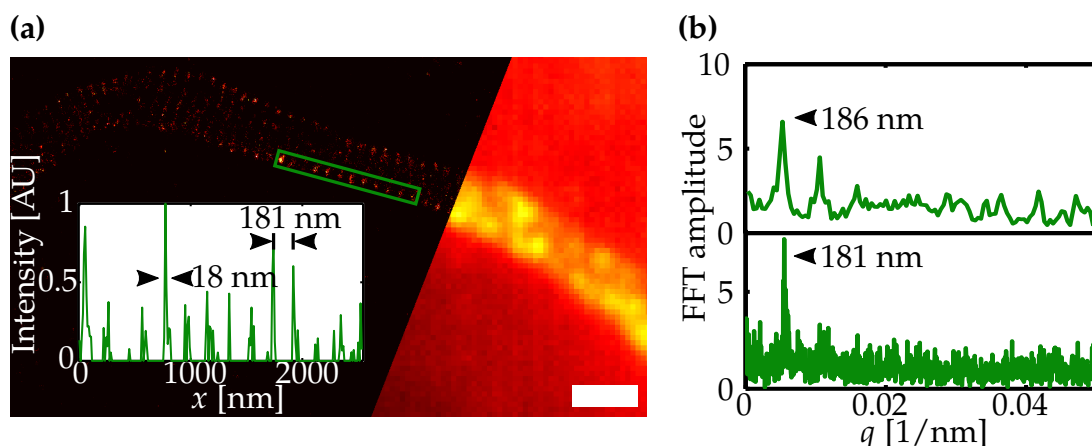


**Figure 3.7:** dSTORM imaging of a mouse hippocampal neuron axon initial segment (AIS). **(a)** dSTORM histogram of Alexa647-labelled  $\beta$ IV-spectrin in an AIS with wide-field image for comparison. Inset: Normalised 1D intensity projection of rectangle. Scale bar is 1  $\mu$ m. **(b)** Fourier spectrum of intensity projection from inset region (upper) and whole image (lower), showing the periodicity of the  $\beta$ IV-spectrin clusters.

While no features of any kind can be identified in the wide-field image, the STORM reconstruction prominently displays the periodic spectrin-actin cytoskeletal structure characteristic for the axon terminal membrane. Through the removal of dirt and non-blinking aggregates by particle tracking, the resolution could be improved up to a maximum of about 20 nm for some of the spectrin clusters. The inter-cluster distance can be determined by taking all intensity values along and near the structure's backbone, projecting them along the wide axis, and calculating the Fourier transform  $\hat{I}(q)$ . A sharp

peak in the spatial frequency spectrum corresponds to a spacing of  $1/q = 181$  nm, the same as discovered in earlier publications [115].

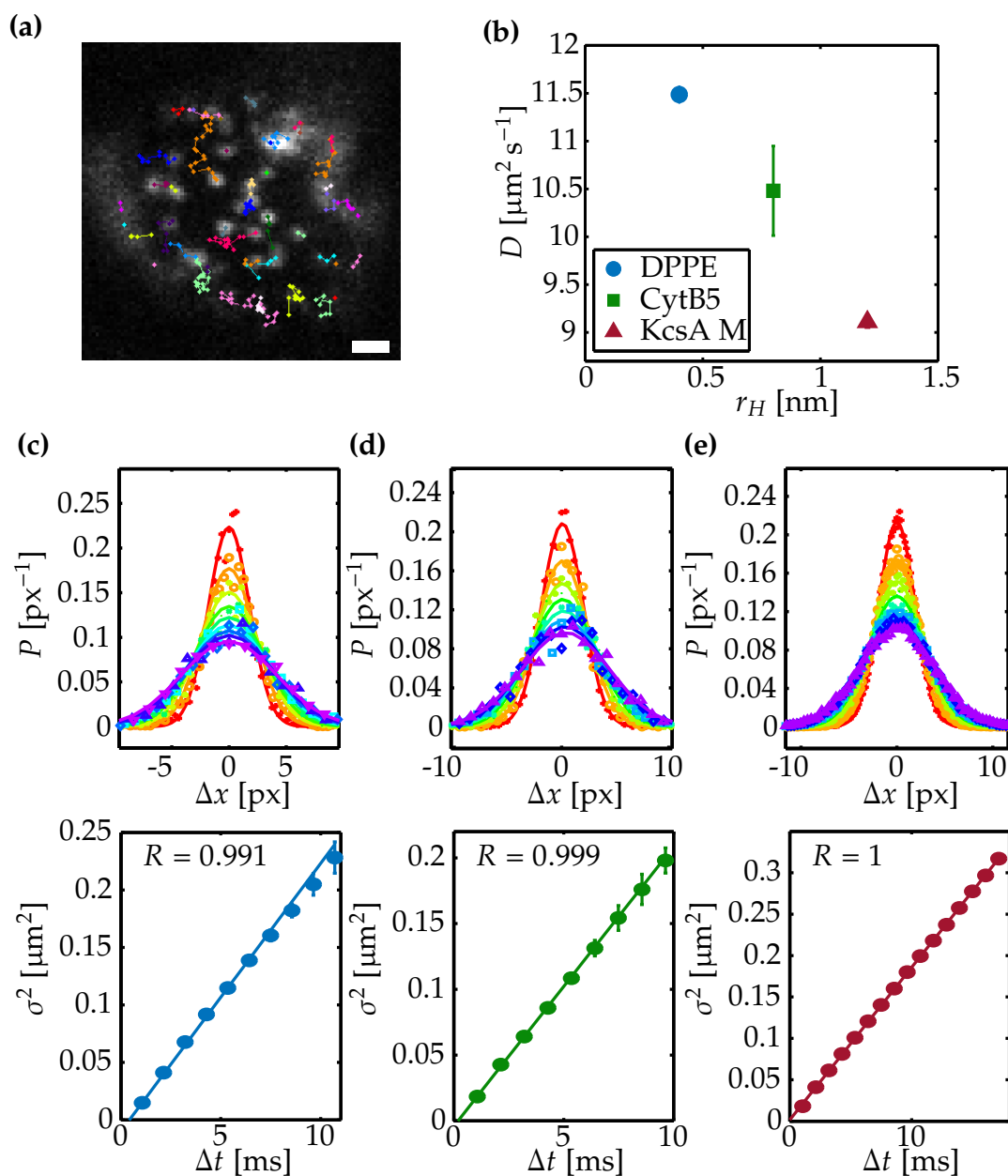


**Figure 3.8:** Single particle tracking in black lipid membranes. **(a)** Example of Atto655-DPPE diffusing in a BLM with overlaid tracks. **(b)** Diffusion analysis results. **(c–e)** Displacement histograms and MSD curves with fit results.

The particle tracking module was evaluated by incorporating lipids and membrane proteins labelled with Atto655 into an artificial black lipid membrane (BLM) spanned over a polytetrafluoroethylene pore  $120 \mu\text{m}$  in diameter. The labelled probes – either DPPE, Cytochrome B5, or a monomeric subunit of the potassium ion channel protein KcsA – were recorded while diffusing through the POPC/POPE BLM and tracked with both NearestNeighbor- and u-Track plugins.

Using the previewer in combination with the very fast nearest-neighbour tracker makes it possible to quickly fine-tune the most important tracking parameters such as maximum particle linking distance or minimum trajectory length which then serve as inputs for the more sophisticated but slower u-Track. This supervised tracking makes it possible to achieve a high level of tracking accuracy in a small amount of time without having to repeat all analysis steps over and over. The diffusion coefficients obtained by mean-squared displacement histogram analysis range from  $9.1(1) \mu\text{m}^2 \text{s}^{-1}$  for the KcsA monomer to  $11.5(1) \mu\text{m}^2 \text{s}^{-1}$  for DPPE, in excellent agreement with earlier FCS measurements [113].

To summarise, TrackNTrace is a versatile tool for the analysis of fluorescence microscopy data. The user-friendly interface in combination with a powerful visual feedback mechanism allows for a high degree of control and flexibility. Parameters can be quickly adjusted and iteratively optimised instead of requiring the user to resort to educated guessing. Small adjustments to existing routines as well as large-scale projects can be implemented with relative ease due to the modular nature of the plugin schema. The large prevalence of MATLAB in the life sciences ensures that scientists can quickly familiarise themselves with the framework and gain access to a large array of useful methods from the start.

## 3.3 Additional plugin development & experiments

TNT can quickly and easily be adapted to a diverse range of experiments. Apart from supporting the data analysis performed during this thesis, it was also used to help along with collaborations and other group members' projects. The following section will briefly summarise the most important ones.

### 3.3.1 Diffusion on membrane-coated silica beads

Membrane fusion is a complex process that is typically studied by observing the reaction of differently labelled, sometimes surface-bound SUVs with each other. A simpler approach towards such an assay is to use artificial silica beads and coat them with a fluorescent lipid mixture, similar to a supported lipid bilayer. Beads brought in close contact by chance or on purpose, e.g. through optical trapping, can be bleached in specific places or doped with other fluorophores. The diffusive speed inferred from position and magnitude of the changes in fluorescence intensity can be used to estimate fusion contact zone size or fusion speed, as performed in a recent publication by Savić et al. [2].

To make sure the FRAP-based method would give robust enough measures of the fusion contact zone, the bilayer diffusion coefficients of these beads was determined independently by single particle tracking using MOSAIC [116] and an earlier version of TNT. Only the top cap of the beads, with a diameter of roughly  $4\ \mu\text{m}$  against the  $6.5\ \mu\text{m}$  bead size, was imaged. The error made by projecting the molecules diffusing within the spherical surface on the 2D camera grid before performing localisation and tracking is 8% at most. The average diffusion coefficient obtained this way,  $\langle D \rangle = 1.3(2)\ \mu\text{m}^2\ \text{s}^{-1}$ , is typical for a supported bilayer, with a broad range of values as depicted in fig. 3.9.

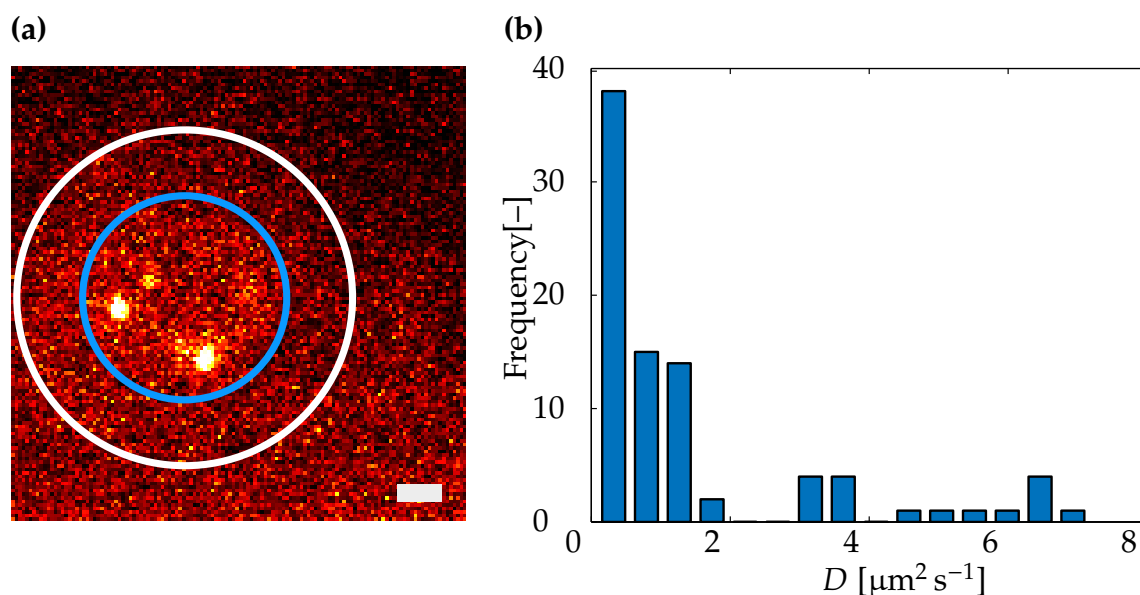


**Figure 3.9:** Single particle tracking in silica beads coated with a 50:24.997:25:0.003 mixture of DOPC/DOPE/Cholesterol/Atto655-DPPE **(a)** Image of single Atto655-DPPE molecules in the coated bead bilayer. The blue circle marks the tracking area, the white circle indicates the bead diameter. Scale bar is  $1\ \mu\text{m}$ . **(b)** The lipid diffusion coefficients differ greatly between individual beads, with an average of  $\langle D \rangle = 1.3(2)\ \mu\text{m}^2\ \text{s}^{-1}$ . The figure and the data used to create it was published in [2].

### 3.3.2 On-/off-state distribution in carbon nanodots

Carbon nanodots (CND) are carbon-based, fluorescent nanoparticles combining properties of organic dyes and quantum dots. They are extremely photo-stable, can easily be tuned to a specific spectral range, and are bio-compatible in contrast to quantum dots. Like their semiconductor analogues, CNDs show pronounced blinking with an on- or off-state-duration distribution that follows a power law whereas organic dye states are exponentially distributed [117]. On one hand, such a behaviour can be beneficial as blinking can then be observed on any time-scale, but the overall spread of the on-/off-timings, in the same vein, is much higher compared to conventional fluorophores.

Understanding and thereby being able to modify this blinking property is crucial to increase the viability of CNDs for techniques such as STORM and SOFI [118] which depend on precise switching of molecules.

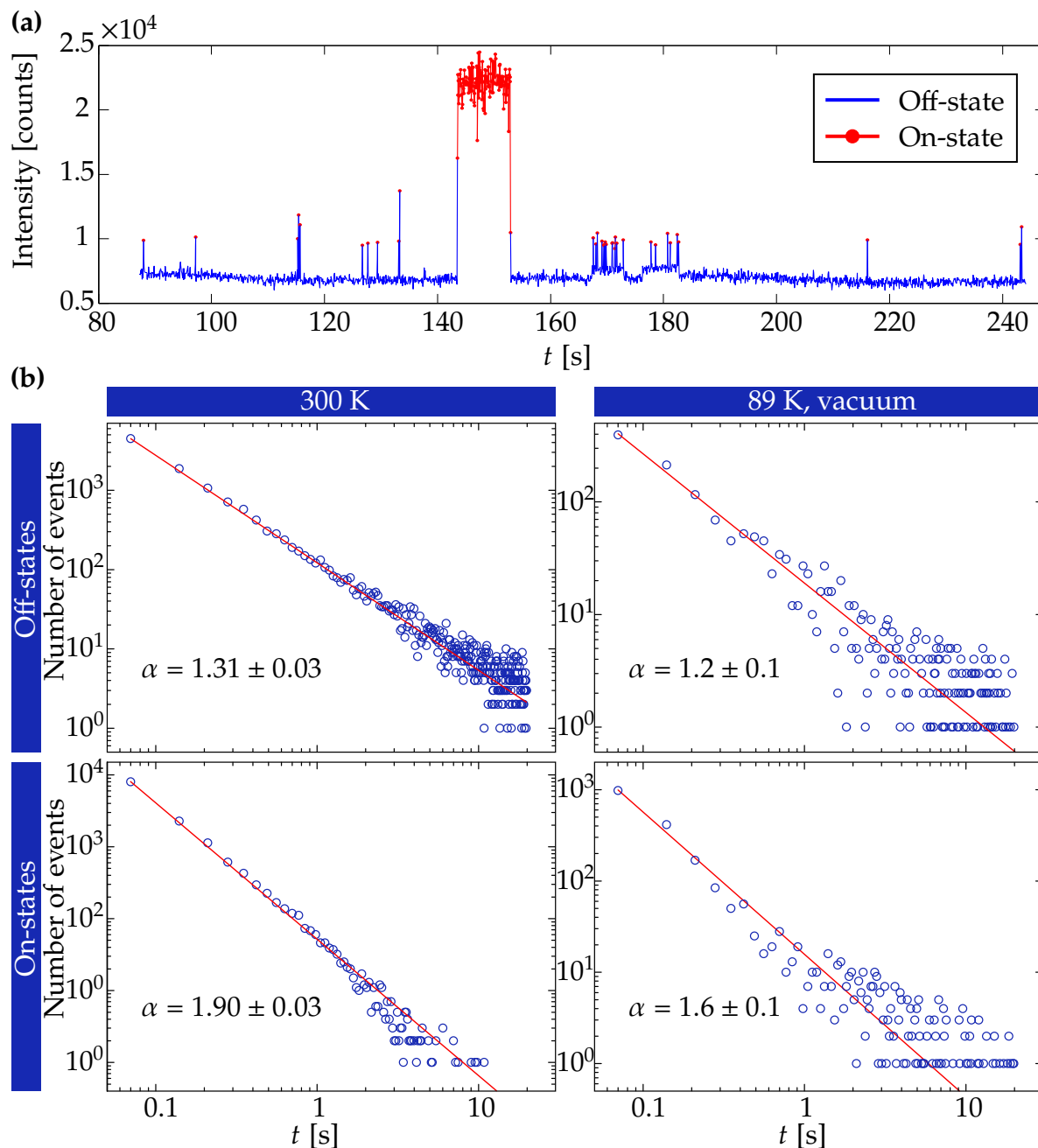


**Figure 3.10:** Results of on-/off-state analysis obtained by TNT. (a) Example trace recorded with an acquisition time of  $t_{\min} = 70$  ms at room temperature showing switching behaviour. (b) Power-law state distributions obtained from whole sample with fit using the equation  $f(t) = a(t/t_{\min})^{-\alpha} + b$ . Data recorded by Syamantak Khan, analysis and figure done by Alexey Chizhik (review pending).

When imaging surface-immobilised CNDs, the on- and off-state distribution can easily be extracted with TrackNTrace by particle tracking. CNDs are localised and tracked

within a radius of  $r = 2$  px to account for sample drift and jitter with a certain detection gap size of  $N$  frames. On- and off times can then be determined simply by collecting the lengths of all continuous localisation events and gaps. The time-scale of both on- and off-distributions is limited by the camera acquisition time  $t_{\text{on/off,min}}$  and the maximum gap size  $N \cdot t_{\text{frame}}$ . Hundreds of emitters can be imaged at the same time, and a statistically robust amount of data can be collected within seconds – much faster than any FCS experiment, for example.

To determine if CNDs could be viable for photo-switching experiments at cryogenic temperatures, their blinking behaviour at 300 K versus 89 K in vacuum was determined. With liquid-nitrogen cooling, fluorophore photo-stability is generally increased while the probability for a triplet-state transition is decreased at the same time. This reduces the applicability of organic fluorophores in such cases which is one reason carbon nanodots and quantum dots have seen more interest in recent years. The results of such an experiment are depicted in fig. 3.10, showing an exemplary fluorescence trace together with the state analysis. While the TNT routine was written by myself, the data was recorded by Syamantak Khan and both the analysis as well as the figure itself was provided by Alexey Chizhik. As expected, the CNDs observed in this case exhibit power-law-distributed blinking. Decreasing the temperature naturally prolongs the time that the CND stays in the on-state whereas the off-times shows no such behaviour. This supports the idea that the fluorescence intermittency of CNDs is reliant on surface charge transfer via electron tunnelling which is unaffected by temperature change and already known to occur in ordinary quantum dots [119]. Calibration objects for STORM and SOFI are being prepared at the moment to determine how well-suited these probes are for super-resolution microscopy.

### 3.3.3 Membrane signalling protein activation in *Dictyostelium discoideum*

*Dictyostelium discoideum* is a so-called “social amoebae”, a slime mould composed of single, independent cells that can organise into a multi-cellular organism if starved for food. The mechanism allowing the cells to synchronise and cluster is based on secretion of cyclic adenosine monophosphate (cAMP). When detected by receptor proteins on the cell membrane, a signalling cascade is activated which in turn triggers a reorganisation of the whole cytoskeleton. The *D. d.* cells begin to migrate within the cAMP gradient towards the strongest concentration, a process known as chemotaxis. As *D. d.*'s genome is fully sequenced, it has become the prime model organism for cell sensing and migration, with the latter being similar to human cancer cells [120]. Learning how these amoebae survey and move through their surroundings is therefore highly beneficial.



The signal transduction chain of *D. d.* is made up of a large, highly complex protein network which is still not fully understood, forcing researchers interested in the topic to concentrate on small subsets of the complete protein family. Together with Marco Tarantola's group from the Max Planck Institute for Dynamics and Self-Organization, I collaborated on a project focused on investigating the activation rates of RasG, a protein within the Ras subfamily. In *D. d.*, Ras is responsible for relaying cAMP activation events between a receptor's transmembrane domain and the cytosolic part of the transduction network. RasG is a GTPase, or G-protein, which can exist in two structurally distinct forms. In its "off"-state, RasG is bound by guanosine diphosphate (GDP) and connected to the plasma membrane. After upstream activation<sup>4</sup> of a different G-protein, the expression of guanine nucleotide exchange factors (GEF) is promoted which in turn switches RasG to an "on"-state, swapping GDP with its triphosphate analogue, GTP. The protein can be turned off again by GTPase-activating proteins (GAP) hydrolysing the GTP [121].

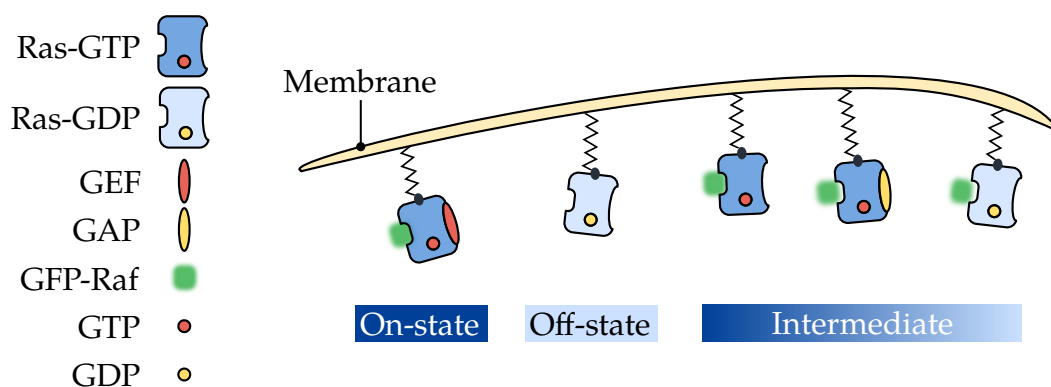


**Figure 3.11:** Presumed diffusive states of RasG in *Dictyostelium discoideum*. In its active form, RasG is GTP-bound by reaction with a nucleotide exchange factor (GEF) and is ready to interact with other proteins. It is switched off by GAP, hydrolysing GTP to GDP, but stays membrane-bound. Instead of labelling RasG directly, the *D. d.* cells are genetically modified to express RBD-Raf-GFP, a green-fluorescent-protein variant which binds to RasG-GTP.

When active, RasG binds and interacts with other proteins responsible for different parts of the cell migration engine. Evidently, it should be possible to extract on- and off-switching rates by measuring the diffusion of RasG and the probabilities to occupy a specific diffusive state with particle tracking. Mathematically, the trajectory data can be expressed as experimentally measured outcomes of a hidden Markov chain model [122]. Here, the observed particle is thought to occupy a state  $s_i(D_i)$  at time  $t$ , with the probability  $p_{ij}$  to change to – or stay in – a state  $s_j(D_j)$  between  $t$  and  $t + \Delta t$ . The transition

<sup>4</sup>“Up” refers to the position of a signal protein within the transduction hierarchy. The highest point, associated with the earliest changes, is occupied by the cAMP receptors.

depends solely on the present state and is therefore memoryless (“Markovian”) but both the currently observed state as well as the total number of states is not explicitly known to the observer (“hidden”). They can, however, be determined approximately by computational optimisation using iterative Monte Carlo modelling such as the variational-Bayes algorithm (vbSPT, [123]) which was employed in this thesis.

The schematic of the various possible binding and diffusion states of RasG is laid out in fig. 3.11. It is important to note that instead of labelling RasG directly, *D. d.* is genetically modified to express RBD-Raf-GFP which in turn binds to RasG-GTP. RBD-Raf-GFP is a binding domain engineered from Ras-related proteins spliced together with green fluorescent protein (GFP) which can be excited by a  $\lambda_{\text{exc}} = 488 \text{ nm}$  laser. The reason for doing so is the concentration of RasG within the cell which is too high to conduct any single-molecule experiments. While the protein expression level can be reduced, it was decided that this could alter the cell function too much and so an indirect labelling scheme was chosen instead [124, 125].

To observe RasG cycling through on- and off-states, *D. d.* cells were placed in a microchannel and subjected to a weak cAMP gradient of  $\Delta c/\Delta x = 4 \text{ nM } \mu\text{m}^{-1}$ . The gradient was created by flushing two solutions of cAMP and normal buffer through an array of flow resistors interconnected in such a way as to mix both fluids in discretised steps from 0% to 100%. The cells are introduced further downstream and then tracked while moving between the two channel walls. Fig. 3.12 shows a diagram of this gradient mixer together with a densely labelled fluorescent cell moving towards the gradient.

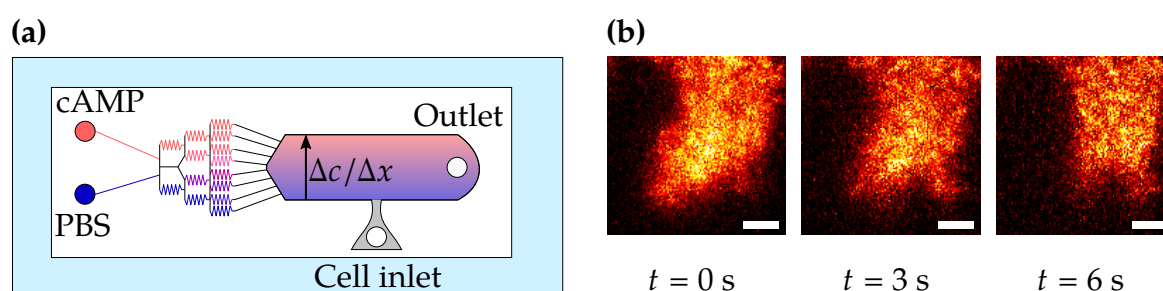


**Figure 3.12:** Gradient mixer with moving *Dictyostelium discoideum* cell. **(a)** Gradient mixer microchannel made by fusing a polydimethylsiloxane cast onto a conventional glass coverslip. **(b)** Fluorescently labelled *D. d.* cell moving through the channel to the top right in the direction of the gradient. Images taken with an iXon-885DU EMCCD (*Andor, Ireland*) at an acquisition speed of 200 Hz. Scale bars are 2  $\mu\text{m}$ .

Using TNT in conjunction with vbSPT, the diffusive state analysis was carried out both on the wild type *D. d.* cells as well as a positive control (Ras-G12V, [125]). The latter was modified to express a constitutively active form of RasG which cannot be hydrolysed and is permanently switched on. TNT’s preview function is especially helpful in this case as localisation and tracking settings differ from cell to cell depending on migra-

tion speed or particular labelling efficiency, and unsuitable recordings can be identified immediately.

	State				
$D_{\text{WT}} [\mu\text{m}^2 \text{s}^{-1}]$	0.33	0.41	1.13	1.69	2.97
$p_{\text{WT}}$	0.06	0.10	0.06	0.25	0.53
$D_{\text{pos}} [\mu\text{m}^2 \text{s}^{-1}]$	0.30	0.62	0.76	1.26	–
$p_{\text{pos}}$	0.18	0.25	0.30	0.27	–

**Table 3.2:** Result of vbSPT analysis for wild type and positive control *D. d.* cells.  $p_i$  is the probability to find the fluorophore in the respective diffusive state.

The results are given in tab. 3.2. The diffusion coefficients of both cell types are roughly the same, but the fastest, possibly cytosolic diffusion observed for the WT cells is absent in the positive control. In similar fashion, the occupancies of the slower diffusive states rise, indicating increased RasG activity. Diffusion coefficients of  $0.3 \mu\text{m}^2 \text{s}^{-1}$  to  $1.3 \mu\text{m}^2 \text{s}^{-1}$  are typical for membrane-associated proteins, but the cytosolic diffusion of the RBD-Raf-GFP marker was expected to be at least an order of magnitude higher. This raises the question if the cytosolic fraction is misrepresented by or even completely missing in the tracking data.

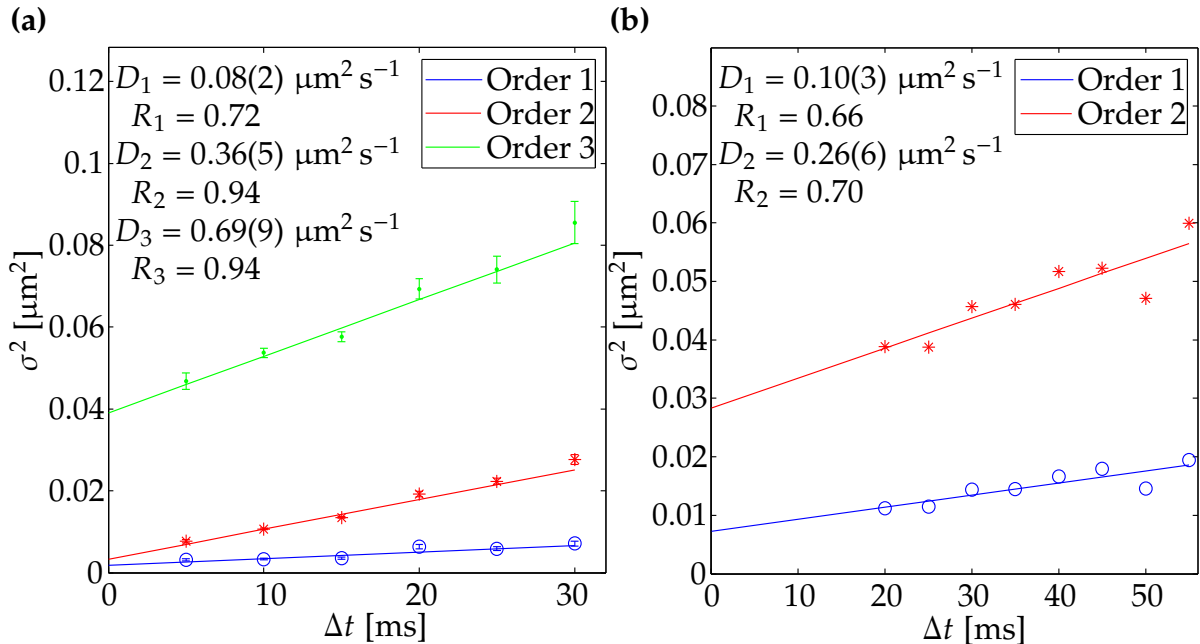


**Figure 3.13:** MSD plots for positive and negative *D. d.* controls with diffusion coefficients and respective correlation coefficients. **(a)** Positive control. **(b)** Negative control, showing no change in diffusion coefficients except for a missing faster component, the opposite of what can be expected for unbound RBD-Raf-GFP.

To quantify the fluorophore's random motion when not bound to RasG and increase the likelihood of obtaining accurate transition rates by identifying all unbound, non-membrane states, a negative control was prepared. Here, RasG was knocked out and replaced by the permanently inactive variant RasG<sup>S17N</sup>. If the labelling scheme and the assumptions about RasG's diffusive states were correct, the negative control would have shown either no activity at all, since RBD-Raf-GFP could not have been recruited to the membrane, or only display one fast diffusion component. When performing the experiments, however, the cells looked identical to the positive control at first glance and a multivariate displacement histogram analysis confirmed this suspicion, as can be seen in fig. 3.13. One reason for this unexpected behaviour is a possible affinity of RBD-Raf-GFP for similar proteins within the Ras family, e.g. RasC [126]. Given the negligible change in diffusion coefficients, it is not unlikely that the particle motion is the result of unspecific binding and completely unrelated to RasG activity. In both cases, the assumptions made about how to approach the project would be completely wrong and all measurements would have to be repeated with directly labelled RasG, for example. As a consequence, further experiments were put on hold for the time being.

## Conclusion & outlook

Improving fluorescence microscopy to a point where structures and dynamic processes can be visualised at the nanometre scale does not only require clever new experimental techniques, but advanced data processing methods as well. To this purpose, the last chapter introduced TrackNTrace, an open-source framework for the analysis of fluorescence microscopy images written in MATLAB. Originally designed as a localisation microscopy and particle tracking tool, TrackNTrace is readily extendible through a simple plugin system. The software is written to be understood and operated by programming novices and researchers previously unfamiliar with this field, providing many state-of-the-art implementations of important algorithms out-of-the-box. An extensive visual feedback mechanism allows inspecting the program's output at all stages of the processing pipeline, facilitating parameter optimisation and error recognition. To validate these concepts, TrackNTrace was set against similar software applications and found to perform comparable to or even better than them. The program has been a great help in analysing many of the experiments presented in this thesis and will hopefully turn out to be similarly beneficial for other scientists.

The main focus of this work lies on enabling diffusion measurements in sub-diffraction-sized vesicles. The aptly named dynaMIET relies on metal-induced energy transfer determined by fluorescence correlation spectroscopy to resolve the motion of fluorescently labelled lipids below the resolution limit. With MIET being a near-field effect, the liposomes have to be brought into close proximity to the metal surface. For this purpose, a highly specific, versatile, and reproducible surface passivation protocol was developed. The assay combines the adaptability of previous PEG-based approaches without requiring any kind of incubation buffer or solvent that can destabilise the coating. Unspecific binding is effectively prevented, tethered vesicles retain their spherical shape, and the functional groups can be changed with ease if needed, e.g. to experiment with cushioned supported bilayers. Although the preparation has turned out

well, the same, unfortunately, cannot be said about the experiment itself. The effective photon yield and stability of the organic dyes is lower than expected from previous experiments by several orders of magnitude – too low to calculate a proper intensity correlation. This is due to the fact that the fluorophores not only photo-bleach much faster than their non-conjugated variants, but can be effectively locked into a dark state which reduces their average brightness considerably. As this happens even at very low excitation intensities and for dyes known not to show triplet state transitions in solution, the most likely reason is dye-lipid interaction, for example quenching by the polar lipid headgroups.

Without being able to determine and eliminate the cause behind the membrane dyes' weak performance, a solution-based approach was developed which uses polarisation-resolved FCS to recover lipid diffusion coefficients. As vesicles automatically move in and out of the excitation focus, the signal quality is less of an issue compared to dynaMIET, where it is necessary to scan each individual vesicle one at a time. However, these measurements would require a label possessing a fixed bilayer-to-dipole orientation which makes it possible to determine its angular displacement. The fluorophore I have been using in this work, designed in the lab of Andrey Klymchenko, not only meets this criterion, but apart from that is also a highly efficient membrane stain, exhibiting exceptional photo-stability, photon yield, and membrane specificity. To describe this symmetric-top rotor diffusing through the spherical bilayer, a model has been developed which also incorporates the vesicle size distribution. While the acquired rotational-diffusion correlation functions are fit very well by the theoretical curves, the diffusion constants thus obtained are heavily biased towards higher values, especially for large liposomes. Several potential artefact sources have been deliberated but none could explain the results adequately.

Although a more successful outcome would certainly have been preferable, the rotational diffusion experiments have still proven to be useful thanks to the squaraine membrane dye discovered in the process. As the fluorophore has all the qualities that the organic dyes used in the dynaMIET experiments lacked, it could turn out to be the key factor in solving the photon yield issues. By using circularly polarised laser light, the orientational dependence of the emission can be eliminated and the measurements conducted the same way as before. The advantages of pursuing dynaMIET in favour of other techniques are clear: It can be combined with any standard vesicle surface assay and adapted to particular experimental conditions by choosing the optimal metal surface. Instead of using gold, as done in this case for vesicles up to 100 nm in diameter, MIET can be tweaked towards sub-nanometre sensitivity. Furthermore, the method is single-molecule sensitive, so that diffusion could potentially be estimated on a per-vesicle basis given sufficient emission intensity. Finally, calculating an average

---

lifetime in addition to the intensity correlations allows us to immediately identify and filter deformed vesicles which is impossible with other techniques.

As has become clear during the course of this thesis, single-molecule measurements in sub-diffraction-sized vesicles present a difficult challenge due to a decline in fluorophore performance which could not be anticipated from previous fluorescence microscopy experiments. Despite some setbacks, I am confident that the ideas and findings gathered in this work provide the necessary foundation to successfully probe the diffusion of lipids and proteins in membranes beyond the microscopic scale.

## A.1 Additional figures and tables

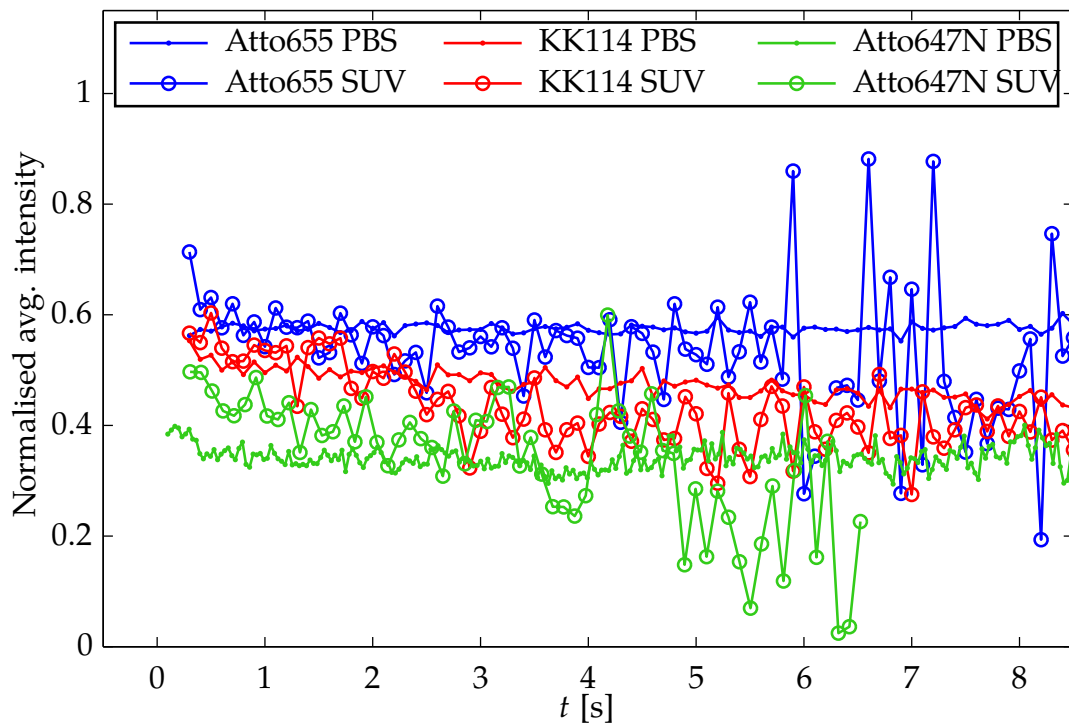
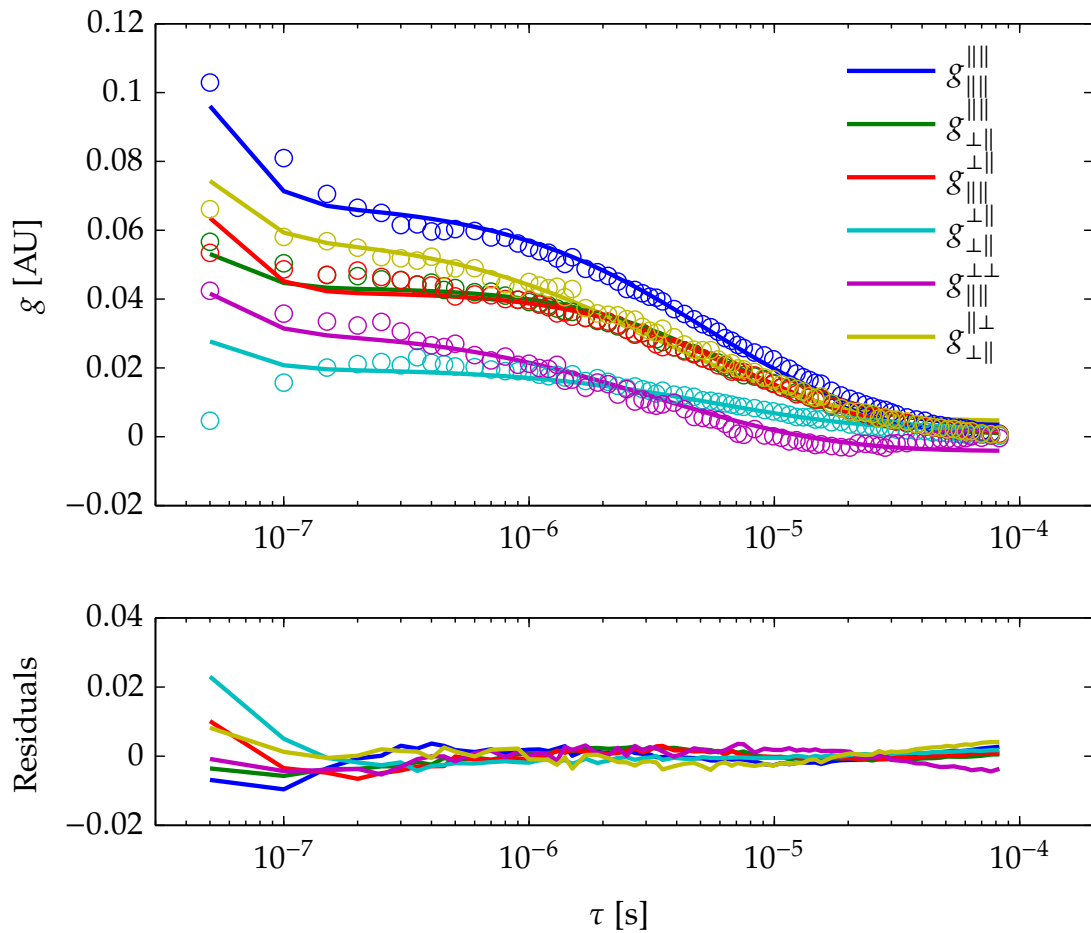


Figure A.1: Normalised average intensity traces of lipid-conjugated dyes.





**Figure A.2:** Polarisation-resolved FCS curves of  $R_p = 25$  nm vesicles labelled with DiD. The curves were purposefully fitted without a triplet state model, demonstrating how clearly a triplet transition previously unaccounted for is visible in the correlation curves.

## A.2 Rotational diffusion FCS functions

This section lists all six rotational diffusion FCS functions as laid out in sec. 2.1.3, with  $D_p = D_{\parallel} - D_{\perp}$ .

$$\begin{aligned}
g_{\parallel\parallel\parallel}^{\parallel\parallel\parallel} &= \frac{2e^{-4t(5D_{\perp}+4D_p)}}{11025(6D_{\perp}\tau+1)^2(6D_{\perp}\tau+4D_p\tau+1)^2} \left[ 49e^{4t(5D_{\perp}+4D_p)} (60D_{\perp}^2\tau^2 + 4D_{\perp}\tau(10D_p\tau+7) + 8D_p\tau+3)^2 \right. \\
&\quad + 60e^{2t(7D_{\perp}+6D_p)} (42D_{\perp}^2\tau^2 + D_{\perp}\tau(28D_p\tau+25) + 6D_p\tau+3)^2 + 20e^{2t(7D_{\perp}+8D_p)} (42D_{\perp}^2\tau^2 + D_{\perp}\tau(28D_p\tau+25) + 8D_p\tau+3)^2 \\
&\quad \left. + 20e^{12D_p t} (6D_{\perp}\tau+2D_p\tau+1)^2 + e^{16D_p t} (18D_{\perp}\tau+8D_p\tau+3)^2 + 35(6D_{\perp}\tau+1)^2 \right] \\
g_{\perp\parallel}^{\parallel\parallel\parallel} &= \frac{e^{-4t(5D_{\perp}+4D_p)}}{11025(6D_{\perp}\tau+1)^2(6D_{\perp}\tau+4D_p\tau+1)^2} \left[ 98e^{4t(5D_{\perp}+4D_p)} (3600D_{\perp}^4\tau^4 + 240D_{\perp}^3\tau^3(20D_p\tau+11) + 8D_{\perp}^2\tau^2(200D_p^2\tau^2 + 325D_p\tau+86) \right. \\
&\quad + 4D_{\perp}\tau(140D_p^2\tau^2 + 114D_p\tau+19) + 48D_p^2\tau^2 + 26D_p\tau+3) - 10e^{2t(7D_{\perp}+8D_p)} (3528D_{\perp}^4\tau^4 + 84D_{\perp}^3\tau^3(56D_p\tau+29) \\
&\quad \left. + 2D_{\perp}^2\tau^2(784D_p^2\tau^2 + 896D_p\tau+205) + D_{\perp}\tau(112D_p^2\tau^2 - 96D_p\tau-1) - 96D_p^2\tau^2 - 44D_p\tau-3) \right. \\
&\quad \left. - 30e^{2t(7D_{\perp}+6D_p)} (3528D_{\perp}^4\tau^4 + 84D_{\perp}^3\tau^3(56D_p\tau+29) + 2D_{\perp}^2\tau^2(784D_p^2\tau^2 + 1316D_p\tau+205) + D_{\perp}\tau(672D_p^2\tau^2 + 488D_p\tau-1) \right. \\
&\quad \left. + 72D_p^2\tau^2 + 30D_p\tau-3) - 20e^{12D_p t} (6D_{\perp}\tau+2D_p\tau+1)^2 - e^{16D_p t} (18D_{\perp}\tau+8D_p\tau+3)^2 - 35(6D_{\perp}\tau+1)^2 \right]
\end{aligned}$$

$$\begin{aligned}
 g_{\parallel\parallel}^{\perp\perp} &= \frac{e^{-4t(5D_{\perp}+4D_p)}}{11025(6D_{\perp}\tau+1)^2(6D_{\perp}\tau+4D_p\tau+1)^2} \left[ 98e^{4t(5D_{\perp}+4D_p)} \left( 3600D_{\perp}^4\tau^4 + 240D_{\perp}^3\tau^3(20D_p\tau+11) + 8D_{\perp}^2\tau^2 \left( 200D_p^2\tau^2 + 325D_p\tau + 86 \right) \right. \right. \\
 &\quad \left. \left. + 4D_{\perp}\tau \left( 140D_p^2\tau^2 + 114D_p\tau + 19 \right) + 48D_p^2\tau^2 + 26D_p\tau + 3 \right) + 30e^{2t(7D_{\perp}+6D_p)} \left( 7056D_{\perp}^4\tau^4 + 84D_{\perp}^3\tau^3(112D_p\tau+67) \right. \right. \\
 &\quad \left. \left. + 4D_{\perp}^2\tau^2 \left( 784D_p^2\tau^2 + 1358D_p\tau + 349 \right) + D_{\perp}\tau \left( 1120D_p^2\tau^2 + 968D_p\tau + 127 \right) + 96D_p^2\tau^2 + 54D_p\tau + 3 \right) \right. \\
 &\quad \left. + 10e^{2t(7D_{\perp}+8D_p)} \left( 7056D_{\perp}^4\tau^4 + 84D_{\perp}^3\tau^3(112D_p\tau+67) + 4D_{\perp}^2\tau^2 \left( 784D_p^2\tau^2 + 1400D_p\tau + 349 \right) + D_{\perp}\tau \left( 1232D_p^2\tau^2 + 936D_p\tau + 127 \right) \right. \right. \\
 &\quad \left. \left. + 96D_p^2\tau^2 + 44D_p\tau + 3 \right) - 20e^{12D_p t} (6D_{\perp}\tau + 2D_p\tau + 1)^2 - e^{16D_p t} (18D_{\perp}\tau + 8D_p\tau + 3)^2 - 35(6D_{\perp}\tau + 1)^2 \right]
 \end{aligned}$$

$$\begin{aligned}
 g_{\perp\perp}^{\perp\perp} &= \frac{e^{-4t(5D_{\perp}+4D_p)}}{44100(6D_{\perp}\tau+1)^2(6D_{\perp}\tau+4D_p\tau+1)^2} \left[ 392e^{4t(5D_{\perp}+4D_p)} \left( 60D_{\perp}^2\tau^2 + 4D_{\perp}\tau(10D_p\tau+7) + 8D_p\tau + 3 \right)^2 \right. \\
 &\quad \left. - 240e^{2t(7D_{\perp}+6D_p)} \left( 42D_{\perp}^2\tau^2 + D_{\perp}\tau(28D_p\tau+25) + 6D_p\tau + 3 \right)^2 - 80e^{2t(7D_{\perp}+8D_p)} \left( 42D_{\perp}^2\tau^2 + D_{\perp}\tau(28D_p\tau+25) + 8D_p\tau + 3 \right)^2 \right. \\
 &\quad \left. + 60e^{12D_p t} (6D_{\perp}\tau + 2D_p\tau + 1)^2 + 3e^{16D_p t} (18D_{\perp}\tau + 8D_p\tau + 3)^2 + 105(6D_{\perp}\tau + 1)^2 \right]
 \end{aligned}$$

$$\begin{aligned}
 g_{\parallel\parallel}^{\perp\perp} &= \frac{1}{3175200} \left[ \frac{423360D_{\perp}^2\tau^2 e^{-6D_{\perp}t}}{(6D_{\perp}\tau+1)^2} + \frac{100800D_p^2\tau^2 e^{-4t(3D_{\perp}+D_p)}}{(6D_{\perp}\tau+1)^2(6D_{\perp}\tau+4D_p\tau+1)^2} + \frac{141120\tau^2(3D_{\perp}+2D_p)^2 e^{-6D_{\perp}t-4D_p t}}{(6D_{\perp}\tau+4D_p\tau+1)^2} \right. \\
 &\quad \left. + \frac{315e^{-20D_{\perp}t}(18D_{\perp}\tau+8D_p\tau+3)^2}{(6D_{\perp}\tau+1)^2(6D_{\perp}\tau+4D_p\tau+1)^2} + 9e^{-20D_{\perp}t} \left( \frac{1}{6D_{\perp}\tau+4D_p\tau+1} + \frac{2}{6D_{\perp}\tau+1} \right)^2 \right. \\
 &\quad \left. + 80e^{-6D_{\perp}t} \left( -\frac{12}{6D_{\perp}\tau+4D_p\tau+1} + \frac{11}{6D_{\perp}\tau+1} + 7 \right)^2 + \frac{8640e^{-6D_{\perp}t-4D_p t}(\tau(D_{\perp}(42D_{\perp}\tau+28D_p\tau+13)+2D_p)+1)^2}{(6D_{\perp}\tau+1)^2(6D_{\perp}\tau+4D_p\tau+1)^2} \right. \\
 &\quad \left. + \frac{11340e^{-4t(5D_{\perp}+4D_p)}}{(6D_{\perp}\tau+4D_p\tau+1)^2} + \frac{6480e^{-4t(5D_{\perp}+D_p)}(6D_{\perp}\tau+2D_p\tau+1)^2}{(6D_{\perp}\tau+1)^2(6D_{\perp}\tau+4D_p\tau+1)^2} + 784 \left( -\frac{3}{6D_{\perp}\tau+4D_p\tau+1} + \frac{1}{-6D_{\perp}\tau-1} + 10 \right)^2 \right]
 \end{aligned}$$

$$\begin{aligned}
g_{\perp\perp}^{\parallel\perp} = & \frac{1}{3175200} \left[ -\frac{423360D_{\perp}^2\tau^2e^{-6D_{\perp}t}}{(6D_{\perp}\tau+1)^2} - \frac{100800D_p^2\tau^2e^{-4t(3D_{\perp}+D_p)}}{(6D_{\perp}\tau+1)^2(6D_{\perp}\tau+4D_p\tau+1)^2} - \frac{141120\tau^2(3D_{\perp}+2D_p)^2e^{-6D_{\perp}t-4D_p t}}{(6D_{\perp}\tau+4D_p\tau+1)^2} \right. \\
& + \frac{315e^{-20D_{\perp}t}(18D_{\perp}\tau+8D_p\tau+3)^2}{(6D_{\perp}\tau+1)^2(6D_{\perp}\tau+4D_p\tau+1)^2} + 9e^{-20D_{\perp}t} \left( \frac{1}{6D_{\perp}\tau+4D_p\tau+1} + \frac{2}{6D_{\perp}\tau+1} \right)^2 \\
& + 80e^{-6D_{\perp}t} \left( -\frac{12}{6D_{\perp}\tau+4D_p\tau+1} + \frac{11}{6D_{\perp}\tau+1} + 7 \right)^2 + \frac{8640e^{-6D_{\perp}t-4D_p t}(\tau(D_{\perp}(42D_{\perp}\tau+28D_p\tau+13)+2D_p)+1)^2}{(6D_{\perp}\tau+1)^2(6D_{\perp}\tau+4D_p\tau+1)^2} \\
& \left. + \frac{11340e^{-4t(5D_{\perp}+4D_p)}}{(6D_{\perp}\tau+4D_p\tau+1)^2} + \frac{6480e^{-4t(5D_{\perp}+D_p)}(6D_{\perp}\tau+2D_p\tau+1)^2}{(6D_{\perp}\tau+1)^2(6D_{\perp}\tau+4D_p\tau+1)^2} + 784 \left( -\frac{3}{6D_{\perp}\tau+4D_p\tau+1} + \frac{1}{-6D_{\perp}\tau-1} + 10 \right)^2 \right]
\end{aligned}$$

# List of Figures

1.1	Categories of cellular membrane lipids . . . . .	5
1.2	Model view of cellular membrane with major matrix components . . . . .	7
1.3	Common membrane model systems . . . . .	9
1.4	Fluorescence microscopy methods for diffusion measurements . . . . .	13
2.1	Schematic of the Microtime 200 setup . . . . .	19
2.2	Exemplary TCSPC histogram of Atto655 . . . . .	20
2.3	Pulsed interleaved excitation . . . . .	22
2.4	DynaMIET scheme and calibration curve . . . . .	23
2.5	Theoretical dynaMIET correlation curves for spherical diffusion . . . . .	25
2.6	Complete rotational diffusion of a fluorophore within a vesicle bilayer . . . . .	26
2.7	Theoretical polarisation-resolved FCS curves for vesicle rotational diffusion . . . . .	29
2.8	Electroformation chamber for GUV assembly . . . . .	32
2.9	PEGylated surfaces employed in vesicle FCS experiments . . . . .	33
2.10	Single particle tracking in DEPC <sub>18</sub> GUVs . . . . .	36
2.11	Chemical structures of dSQ12S membrane dye and DEPC <sub>18</sub> . . . . .	37
2.12	Dual-colour surface control images of multilabelled SUVs . . . . .	38
2.13	Vesicle height on Biotin-MeO-PEG surface with Atto655 <sup>l</sup> labelling . . . . .	40
2.14	DynaMIET cross-correlation curves of Atto655 <sup>l</sup> -labelled vesicles . . . . .	41
2.15	Timetraces of Atto655 <sup>l</sup> -labelled vesicles from dynaMIET measurement . . . . .	41
2.16	Bleaching and off-state distributions of Atto647N <sup>l</sup> in PBS . . . . .	42
2.17	Off-state saturation of lipid-conjugated dyes . . . . .	43
2.18	Intensity distributions of lipid-conjugated dyes . . . . .	44
2.19	Vesicle size distributions . . . . .	46
2.20	2f-FCS experiment of vesicles extruded through 50 nm pore. . . . .	47
2.21	Polarisation-resolved FCS curves of $R_p = 15$ nm vesicles . . . . .	48
2.22	Lipid diffusion coefficient as a function of vesicle radius and temperature . . . . .	50
3.1	TrackNTrace input and visualiser GUI . . . . .	56
3.2	Defocused pattern fitting in TrackNTrace . . . . .	59

3.3	Examples of image filtering in TrackNTrace . . . . .	61
3.4	Wavelet filtering in TrackNTrace . . . . .	65
3.5	Simulated test structures for performance evaluation . . . . .	71
3.6	Simulation performance evaluation results . . . . .	72
3.7	dSTORM imaging of a mouse hippocampal neuron axon initial segment . .	73
3.8	Single particle tracking in black lipid membranes . . . . .	74
3.9	Single particle tracking in membrane-coated silica beads . . . . .	76
3.10	Results of on-/off-state analysis obtained by TNT . . . . .	77
3.11	Presumed diffusive states of RasG in <i>Dictyostelium discoideum</i> . . . . .	79
3.12	Gradient mixer with moving <i>Dictyostelium discoideum</i> cell . . . . .	80
3.13	MSD plots for positive and negative <i>D. d.</i> controls . . . . .	81
A.1	Normalised average intensity traces of lipid-conjugated dyes . . . . .	86
A.2	Polarisation-resolved FCS curves of $R_p = 25$ nm vesicles labelled with DiD .	87

# Bibliography

- [1] S. C. Stein and J. Thiart. 'TrackNTrace: A simple and extendable open-source framework for developing single-molecule localization and tracking algorithms'. *Scientific Reports* **6** (1) 2016.
- [2] F. Savić, T.-T. Kliesch, S. Verbeek, C. Bao, J. Thiart, A. Kros, B. Geil and A. Janshoff. 'Geometry of the Contact Zone between Fused Membrane-Coated Beads Mimicking Cell-Cell Fusion'. *Biophysical Journal* **110** (10) 2016, pp. 2216–2228.
- [3] S. J. Singer and G. L. Nicolson. 'The Fluid Mosaic Model of the Structure of Cell Membranes'. *Science* **175** (4023) 1972, pp. 720–731.
- [4] K. Jacobson, E. Sheets and R. Simson. 'Revisiting the fluid mosaic model of membranes'. *Science* **268** (5216) 1995, pp. 1441–1442.
- [5] M. Edidin. 'Timeline: Lipids on the frontier: a century of cell-membrane bilayers'. *Nature Reviews Molecular Cell Biology* **4** (5) 2003, pp. 414–418.
- [6] M. Bezanilla, A. S. Gladfelter, D. R. Kovar and W.-L. Lee. 'Cytoskeletal dynamics: A view from the membrane'. *The Journal of Cell Biology* **209** (3) 2015, pp. 329–337.
- [7] E. Gouaux and R. MacKinnon. 'Principles of Selective Ion Transport in Channels and Pumps'. *Science* **310** (5753) 2005, pp. 1461–1465.
- [8] Y. Fujiyoshi, K. Murata, K. Mitsuoka, T. Hirai, T. Walz, P. Agre, J. B. Heymann and A. Engel. 'Structural determinants of water permeation through aquaporin-1'. *Nature* **407** (6804) 2000, pp. 599–605.
- [9] I. Mellman and G. Warren. 'The Road Taken'. *Cell* **100** (1) 2000, pp. 99–112.
- [10] L. M. Mashburn and M. Whiteley. 'Membrane vesicles traffic signals and facilitate group activities in a prokaryote'. *Nature* **437** (7057) 2005, pp. 422–425.
- [11] C. Théry, M. Ostrowski and E. Segura. 'Membrane vesicles as conveyors of immune responses'. *Nature Reviews Immunology* **9** (8) 2009, pp. 581–593.
- [12] M. Fuhrmans, G. Marelli, Y. G. Smirnova and M. Müller. 'Mechanics of membrane fusion/pore formation'. *Chemistry and Physics of Lipids* **185** 2015, pp. 109–128.

- [13] K. Hashimoto and A. R. Panchenko. 'Mechanisms of protein oligomerization, the critical role of insertions and deletions in maintaining different oligomeric states'. *Proceedings of the National Academy of Sciences* **107** (47) 2010, pp. 20352–20357.
- [14] G. L. Nicolson. 'The Fluid-Mosaic Model of Membrane Structure: Still relevant to understanding the structure, function and dynamics of biological membranes after more than 40 years'. *Biochimica et Biophysica Acta (BBA) - Biomembranes* **1838** (6) 2014, pp. 1451–1466.
- [15] P. G. Saffman and M. Delbrück. 'Brownian motion in biological membranes'. *Proceedings of the National Academy of Sciences* **72** (8) 1975, pp. 3111–3113.
- [16] E. P. Petrov and P. Schwille. 'Translational Diffusion in Lipid Membranes beyond the Saffman-Delbrück Approximation'. *Biophysical Journal* **94** (5) 2008, pp. 375–377.
- [17] D. L. Daleke. 'Regulation of transbilayer plasma membrane phospholipid asymmetry'. *The Journal of Lipid Research* **44** (2) 2002, pp. 233–242.
- [18] D. Lingwood and K. Simons. 'Lipid Rafts As a Membrane-Organizing Principle'. *Science* **327** (5961) 2009, pp. 46–50.
- [19] D. O. Daley, M. Rapp, E. Granseth, K. Melén, D. Drew and G. Von Heijne. 'Global topology analysis of the Escherichia coli inner membrane proteome'. *Science* **308** (5726) 2005, pp. 1321–1323.
- [20] J. Zimmerberg and M. M. Kozlov. 'How proteins produce cellular membrane curvature'. *Nature Reviews Molecular Cell Biology* **7** (1) 2005, pp. 9–19.
- [21] A. Tian and T. Baumgart. 'Sorting of Lipids and Proteins in Membrane Curvature Gradients'. *Biophysical Journal* **96** (7) 2009, pp. 2676–2688.
- [22] Y. A. Domanov, S. Aimon, G. E. S. Toombes, M. Renner, F. Quemeneur, A. Triller, M. S. Turner and P. Bassereau. 'Mobility in geometrically confined membranes'. *Proceedings of the National Academy of Sciences* **108** (31) 2011, pp. 12605–12610.
- [23] L. Iversen, S. Mathiasen, J. B. Larsen and D. Stamou. 'Membrane curvature bends the laws of physics and chemistry'. *Nature Chemical Biology* **11** (11) 2015, pp. 822–825.
- [24] R. Jahn, T. Lang and T. C. Südhof. 'Membrane Fusion'. *Cell* **112** (4) 2003, pp. 519–533.
- [25] R. Jahn and R. H. Scheller. 'SNAREs – engines for membrane fusion'. *Nature Reviews Molecular Cell Biology* **7** (9) 2006, pp. 631–643.



- [26] J. Hsin, J. Gumbart, L. G. Trabuco, E. Villa, P. Qian, C. N. Hunter and K. Schulten. 'Protein-Induced Membrane Curvature Investigated through Molecular Dynamics Flexible Fitting'. *Biophysical Journal* **97** (1) 2009, pp. 321–329.
- [27] S. Vanni, H. Hirose, H. Barelli, B. Antony and R. Gautier. 'A sub-nanometre view of how membrane curvature and composition modulate lipid packing and protein recruitment'. *Nature Communications* **5** 2014, p. 4916.
- [28] B. Różycki and R. Lipowsky. 'Spontaneous curvature of bilayer membranes from molecular simulations: Asymmetric lipid densities and asymmetric adsorption'. *The Journal of Chemical Physics* **142** (5) 2015, p. 054101.
- [29] M. J. Rust, M. Bates and X. Zhuang. 'Sub-diffraction-limit imaging by stochastic optical reconstruction microscopy (STORM)'. *Nature Methods* **3** (10) 2006, pp. 793–796.
- [30] E. Betzig, G. H. Patterson, R. Sougrat, O. W. Lindwasser, S. Olenych, J. S. Bonifacino, M. W. Davidson, J. Lippincott-Schwartz and H. F. Hess. 'Imaging Intracellular Fluorescent Proteins at Nanometer Resolution'. *Science* **313** (5793) 2006, pp. 1642–1645.
- [31] S. W. Hell and J. Wichmann. 'Breaking the diffraction resolution limit by stimulated emission: stimulated-emission-depletion fluorescence microscopy'. *Optics Letters* **19** (11) 1994, p. 780.
- [32] P. Fox-Roberts, R. Marsh, K. Pfisterer, A. Jayo, M. Parsons and S. Cox. 'Local dimensionality determines imaging speed in localization microscopy'. *Nature Communications* **8** 2017, p. 13558.
- [33] J. A. Dix, J. M. Diamond and D. Kivelson. 'Translational Diffusion Coefficient and Partition Coefficient of a Spin-Labeled Solute in Lecithin Bilayer Membranes'. *Proceedings of the National Academy of Sciences* **71** (2) 1974, pp. 474–478.
- [34] G. Nicolson. 'Update of the 1972 Singer-Nicolson Fluid-Mosaic Model of Membrane Structure'. *Discoveries* 2013.
- [35] G. van Meer and A. I. P. M. de Kroon. 'Lipid map of the mammalian cell'. *Journal of Cell Science* **124** (1) 2010, pp. 5–8.
- [36] J. Zimmerberg and K. Gawrisch. 'The physical chemistry of biological membranes'. *Nature Chemical Biology* **2** (11) 2006, pp. 564–567.
- [37] D. Koller and K. Lohner. 'The role of spontaneous lipid curvature in the interaction of interfacially active peptides with membranes'. *Biochimica et Biophysica Acta (BBA) - Biomembranes* **1838** (9) 2014, pp. 2250–2259.

- [38] G. van Meer, D. R. Voelker and G. W. Feigenson. 'Membrane lipids: where they are and how they behave'. *Nature Reviews Molecular Cell Biology* **9** (2) 2008, pp. 112–124.
- [39] E. Fahy, S. Subramaniam, H. A. Brown, C. K. Glass, A. H. Merrill, R. C. Murphy, C. R. Raetz, D. W. Russell, Y. Seyama, W. Shaw, T. Shimizu, F. Spener, G. van Meer, M. S. VanNieuwenhze, S. H. White, J. L. Witztum and E. A. Dennis. 'A comprehensive classification system for lipids'. *The Journal of Lipid Research* **46** (5) 2005, pp. 839–862.
- [40] G. von Heijne and D. Rees. 'Membranes: reading between the lines'. *Current Opinion in Structural Biology* **18** (4) 2008, pp. 403–405.
- [41] P. Somerharju, J. A. Virtanen, K. H. Cheng and M. Hermansson. 'The superlattice model of lateral organization of membranes and its implications on membrane lipid homeostasis'. *Biochimica et Biophysica Acta (BBA) - Biomembranes* **1788** (1) 2009, pp. 12–23.
- [42] M. Carquin, L. D'Auria, H. Pollet, E. R. Bongarzone and D. Tyteca. 'Recent progress on lipid lateral heterogeneity in plasma membranes: From rafts to sub-micrometric domains'. *Progress in Lipid Research* **62** 2016, pp. 1–24.
- [43] R. Koynova and B. Tenchov. 'Transitions between lamellar and nonlamellar phases in membrane lipids and their physiological roles'. *OA Biochemistry* **1** (1) 2013.
- [44] W. Rawicz, K. Olbrich, T. McIntosh, D. Needham and E. Evans. 'Effect of Chain Length and Unsaturation on Elasticity of Lipid Bilayers'. *Biophysical Journal* **79** (1) 2000, pp. 328–339.
- [45] Y.-H. M. Chan and S. G. Boxer. 'Model membrane systems and their applications'. *Current Opinion in Chemical Biology* **11** (6) 2007, pp. 581–587.
- [46] M. Tanaka and E. Sackmann. 'Polymer-supported membranes as models of the cell surface'. *Nature* **437** (7059) 2005, pp. 656–663.
- [47] A. Sonnleitner, G. Schütz and T. Schmidt. 'Free Brownian Motion of Individual Lipid Molecules in Biomembranes'. *Biophysical Journal* **77** (5) 1999, pp. 2638–2642.
- [48] M. Kocun, T. D. Lazzara, C. Steinem and A. Janshoff. 'Preparation of Solvent-Free, Pore-Spanning Lipid Bilayers: Modeling the Low Tension of Plasma Membranes'. *Langmuir* **27** (12) 2011, pp. 7672–7680.
- [49] P. Méléard, L. A. Bagatolli and T. Pott. 'Giant Unilamellar Vesicle Electroformation'. *Methods in Enzymology*. Elsevier BV, 2009, pp. 161–176.

- [50] M. Dezi, A. D. Cicco, P. Bassereau and D. Levy. 'Detergent-mediated incorporation of transmembrane proteins in giant unilamellar vesicles with controlled physiological contents'. *Proceedings of the National Academy of Sciences* **110** (18) 2013, pp. 7276–7281.
- [51] M. M. Lapinski, A. Castro-Forero, A. J. Greiner, R. Y. Ofoli and G. J. Blanchard. 'Comparison of Liposomes Formed by Sonication and Extrusion: Rotational and Translational Diffusion of an Embedded Chromophore'. *Langmuir* **23** (23) 2007, pp. 11677–11683.
- [52] A. Einstein. 'Über die von der molekularkinetischen Theorie der Wärme geforderte Bewegung von in ruhenden Flüssigkeiten suspendierten Teilchen'. *Annalen der Physik* **322** (8) 1905, pp. 549–560.
- [53] S. Sadeghi, M. Müller and R. L. Vink. 'Raft Formation in Lipid Bilayers Coupled to Curvature'. *Biophysical Journal* **107** (7) 2014, pp. 1591–1600.
- [54] M. L. Henle and A. J. Levine. 'Hydrodynamics in curved membranes: The effect of geometry on particulate mobility'. *Physical Review E* **81** (1) 2010.
- [55] Y. Wu, M. Štefl, A. Olzyńska, M. Hof, G. Yahioğlu, P. Yip, D. R. Casey, O. Ces, J. Humpolčková and M. K. Kuimova. 'Molecular rheometry: direct determination of viscosity in Lo and Ld lipid phases via fluorescence lifetime imaging'. *Physical Chemistry Chemical Physics* **15** (36) 2013, p. 14986.
- [56] H. J. Risselada and S. J. Marrink. 'Curvature effects on lipid packing and dynamics in liposomes revealed by coarse grained molecular dynamics simulations'. *Physical Chemistry Chemical Physics* **11** (12) 2009, p. 2056.
- [57] N. Yoshii, T. Emoto and E. Okamura. 'Lateral diffusion of lipids separated from rotational and translational diffusion of a fluid large unilamellar vesicle'. *Colloids and Surfaces B: Biointerfaces* **106** 2013, pp. 22–27.
- [58] J. W. Lichtman and J.-A. Conchello. 'Fluorescence microscopy'. *Nature Methods* **2** (12) 2005, pp. 910–919.
- [59] U. Kubitscheck. *Fluorescence microscopy: from principles to biological applications*. Ed. by U. Kubitscheck. Wiley-Blackwell, 2013.
- [60] M. Sauer, J. Hofkens and J. Enderlein. *Handbook of fluorescence spectroscopy and imaging: from ensemble to single molecules*. Wiley-Blackwell, 2011.
- [61] E. B. Shera, N. K. Seitzinger, L. M. Davis, R. A. Keller and S. A. Soper. 'Detection of single fluorescent molecules'. *Chemical Physics Letters* **174** (6) 1990, pp. 553–557.

- [62] H. C. Ishikawa-Ankerhold, R. Ankerhold and G. P. C. Drummen. 'Advanced Fluorescence Microscopy Techniques – FRAP, FLIP, FLAP, FRET and FLIM'. *Molecules* **17** (12) 2012, pp. 4047–4132.
- [63] N. Chenouard, I. Smal, F. de Chaumont, M. Maška, I. F. Sbalzarini et al. 'Objective comparison of particle tracking methods'. *Nature Methods* **11** (3) 2014, pp. 281–289.
- [64] C. Manzo and M. F. Garcia-Parajo. 'A review of progress in single particle tracking: from methods to biophysical insights'. *Reports on Progress in Physics* **78** (12) 2015, p. 124601.
- [65] B. Johansson, F. Höök, D. Klenerman and P. Jönsson. 'Label-Free Measurements of the Diffusivity of Molecules in Lipid Membranes'. *ChemPhysChem* **15** (3) 2014, pp. 486–491.
- [66] D. Ernst, S. Hain and J. Köhler. 'Setup for single-particle orbit tracking: artifacts and corrections'. *Journal of the Optical Society of America A* **29** (7) 2012, p. 1277.
- [67] R. Metzler, J.-H. Jeon, A. G. Cherstvy and E. Barkai. 'Anomalous diffusion models and their properties: non-stationarity, non-ergodicity, and ageing at the centenary of single particle tracking'. *Physical Chemistry Chemical Physics* **16** (44) 2014, pp. 24128–24164.
- [68] J. Enderlein, I. Gregor, D. Patra, T. Dertinger and U. B. Kaupp. 'Performance of Fluorescence Correlation Spectroscopy for Measuring Diffusion and Concentration'. *ChemPhysChem* **6** (11) 2005, pp. 2324–2336.
- [69] S. T. Hess, S. Huang, A. A. Heikal and W. W. Webb. 'Biological and Chemical Applications of Fluorescence Correlation Spectroscopy: A Review'. *Biochemistry* **41** (3) 2002, pp. 697–705.
- [70] O. Krichevsky and G. Bonnet. 'Fluorescence correlation spectroscopy: the technique and its applications'. *Reports on Progress in Physics* **65** (2) 2002, pp. 251–297.
- [71] E. Haustein and P. Schwille. 'Fluorescence Correlation Spectroscopy: Novel Variations of an Established Technique'. *Annual Review of Biophysics and Biomolecular Structure* **36** (1) 2007, pp. 151–169.
- [72] R. Roy, S. Hohng and T. Ha. 'A practical guide to single-molecule FRET'. *Nature Methods* **5** (6) 2008, pp. 507–516.
- [73] H. Wallrabe and A. Periasamy. 'Imaging protein molecules using FRET and FLIM microscopy'. *Current Opinion in Biotechnology* **16** (1) 2005, pp. 19–27.

- [74] D. M. Jameson and J. A. Ross. 'Fluorescence Polarization/Anisotropy in Diagnostics and Imaging'. *Chemical Reviews* **110** (5) 2010, pp. 2685–2708.
- [75] T. Dertinger, V. Pacheco, I. von der Hocht, R. Hartmann, I. Gregor and J. Enderlein. 'Two-Focus Fluorescence Correlation Spectroscopy: A New Tool for Accurate and Absolute Diffusion Measurements'. *ChemPhysChem* **8** (3) 2007, pp. 433–443.
- [76] N. Petersen. 'Scanning fluorescence correlation spectroscopy. I. Theory and simulation of aggregation measurements'. *Biophysical Journal* **49** (4) 1986, pp. 809–815.
- [77] L. Kastrup, H. Blom, C. Eggeling and S. W. Hell. 'Fluorescence Fluctuation Spectroscopy in Subdiffraction Focal Volumes'. *Physical Review Letters* **94** (17) 2005.
- [78] R. R. Chance, A. Prock and R. Silbey. 'Molecular Fluorescence and Energy Transfer Near Interfaces'. *Advances in Chemical Physics*. John Wiley & Sons, Inc., 1978, pp. 1–65.
- [79] K. H. Drexhage. 'IV Interaction of Light with Monomolecular Dye Layers'. *Progress in Optics*. Vol. 12. 1974, pp. 163–232.
- [80] N. Karedla, A. I. Chizhik, I. Gregor, A. M. Chizhik, O. Schulz and J. Enderlein. 'Single-Molecule Metal-Induced Energy Transfer (smMIET): Resolving Nanometer Distances at the Single-Molecule Level'. *ChemPhysChem* **15** (4) 2014, pp. 705–711.
- [81] C. M. Pieper and J. Enderlein. 'Fluorescence correlation spectroscopy as a tool for measuring the rotational diffusion of macromolecules'. *Chemical Physics Letters* **516** (1-3) 2011, pp. 1–11.
- [82] S. Castorph, S. S. Henriques, M. Holt, D. Riedel, R. Jahn and T. Salditt. 'Synaptic vesicles studied by dynamic light scattering'. *The European Physical Journal E* **34** (6) 2011.
- [83] S. R. Aragón. 'Theory of dynamic light scattering from polydisperse systems'. *The Journal of Chemical Physics* **64** (6) 1976, p. 2395.
- [84] M. Collot, R. Kreder, A. L. Tatarets, L. D. Patsenker, Y. Mely and A. S. Klymchenko. 'Bright fluorogenic squaraines with tuned cell entry for selective imaging of plasma membrane vs. endoplasmic reticulum'. *Chemical Communications* **51** (96) 2015, pp. 17136–17139.
- [85] O. Vites, E.-L. Florin and R. Jahn. 'Docking of Liposomes to Planar Surfaces Mediated by trans-SNARE Complexes'. *Biophysical Journal* **95** (3) 2008, pp. 1295–1302.

- [86] E. Busseron, Y. Ruff, E. Moulin and N. Giuseppone. 'Supramolecular self-assemblies as functional nanomaterials'. *Nanoscale* **5** (16) 2013, p. 7098.
- [87] J. Diao, Y. Ishitsuka, H. Lee, C. Joo, Z. Su, S. Syed, Y.-K. Shin, T.-Y. Yoon and T. Ha. 'A single vesicle-vesicle fusion assay for in vitro studies of SNAREs and accessory proteins'. *Nature Protocols* **7** (6) 2012, pp. 921–934.
- [88] F. Roder, S. Waichman, D. Paterok, R. Schubert, C. Richter, B. Liedberg and J. Piehler. 'Reconstitution of Membrane Proteins into Polymer-Supported Membranes for Probing Diffusion and Interactions by Single Molecule Techniques'. *Analytical Chemistry* **83** (17) 2011, pp. 6792–6799.
- [89] D. Ruhlandt and J. Enderlein. *Metal-Induced Energy Transfer - MIET*. 2016. URL: <http://www.joerg-enderlein.de/Software.html> (visited on 18/04/2017).
- [90] N. Kahya and P. Schwille. 'How Phospholipid-Cholesterol Interactions Modulate Lipid Lateral Diffusion, as Revealed by Fluorescence Correlation Spectroscopy'. *Journal of Fluorescence* **16** (5) 2006, pp. 671–678.
- [91] A. Filippov, G. Orädd and G. Lindblom. 'Domain Formation in Model Membranes Studied by Pulsed-Field Gradient-NMR: The Role of Lipid Polyunsaturation'. *Biophysical Journal* **93** (9) 2007, pp. 3182–3190.
- [92] K. Weiß and J. Enderlein. 'Lipid Diffusion within Black Lipid Membranes Measured with Dual-Focus Fluorescence Correlation Spectroscopy'. *ChemPhysChem* **13** (4) 2012, pp. 990–1000.
- [93] F. Heinemann, V. Betaneli, F. A. Thomas and P. Schwille. 'Quantifying Lipid Diffusion by Fluorescence Correlation Spectroscopy: A Critical Treatise'. *Langmuir* **28** (37) 2012, pp. 13395–13404.
- [94] F. A. Thomas, I. Visco, Z. Petrášek, F. Heinemann and P. Schwille. 'Diffusion coefficients and dissociation constants of enhanced green fluorescent protein binding to free standing membranes'. *Data in Brief* **5** 2015, pp. 537–541.
- [95] B. Pignataro, C. Steinem, H.-J. Galla, H. Fuchs and A. Janshoff. 'Specific Adhesion of Vesicles Monitored by Scanning Force Microscopy and Quartz Crystal Microbalance'. *Biophysical Journal* **78** (1) 2000, pp. 487–498.
- [96] M. De Brabander, G. Geuens, R. Nuydens, M. Moeremans and J. De Mey. 'Probing microtubule-dependent intracellular motility with nanometre particle video ultramicroscopy (nanovid ultramicroscopy)'. *Cytobios* **43** (174S) 1985, pp. 273–283.

- [97] D. Sage, H. Kirshner, T. Pengo, N. Stuurman, J. Min, S. Manley and M. Unser. ‘Quantitative evaluation of software packages for single-molecule localization microscopy’. *Nature Methods* **12** (8) 2015, pp. 717–724.
- [98] D. Patra, I. Gregor, J. Enderlein and M. Sauer. ‘Defocused imaging of quantum-dot angular distribution of radiation’. *Applied Physics Letters* **87** (10) 2005, p. 101103.
- [99] S. M. Anthony and S. Granick. ‘Image Analysis with Rapid and Accurate Two-Dimensional Gaussian Fitting’. *Langmuir* **25** (14) 2009, pp. 8152–8160.
- [100] C. S. Smith, N. Joseph, B. Rieger and K. A. Lidke. ‘Fast, single-molecule localization that achieves theoretically minimum uncertainty’. *Nature Methods* **7** (5) 2010, pp. 373–375.
- [101] R. Parthasarathy. ‘Rapid, accurate particle tracking by calculation of radial symmetry centers’. *Nature Methods* **9** (7) 2012, pp. 724–726.
- [102] S. Agarwal, K. Mierle et al. *Ceres Solver*. 2010. URL: <http://ceres-solver.org> (visited on 20/04/2017).
- [103] K. Jaqaman, D. Loerke, M. Mettlen, H. Kuwata, S. Grinstein, S. L. Schmid and G. Danuser. ‘Robust single-particle tracking in live-cell time-lapse sequences’. *Nature Methods* **5** (8) 2008, pp. 695–702.
- [104] M. Hirsch, R. J. Wareham, M. L. Martin-Fernandez, M. P. Hobson and D. J. Rolfe. ‘A Stochastic Model for Electron Multiplication Charge-Coupled Devices – From Theory to Practice’. *PLoS ONE* **8** (1) 2013, e53671.
- [105] G. Danuser and M. Stricker. ‘Parametric model fitting: from inlier characterization to outlier detection’. *IEEE Transactions on Pattern Analysis and Machine Intelligence* **20** (3) 1998, pp. 263–280.
- [106] J. L. Blanco-Claraco. *nanoflann: a C++ header-only library for Nearest Neighbor (NN) search with KD-trees*. 2016. URL: <https://github.com/jlblancoc/nanoflann> (visited on 21/04/2017).
- [107] I. Izeddin, J. Boulanger, V. Racine, C. Specht, A. Kechkar, D. Nair, A. Triller, D. Choquet, M. Dahan and J. Sibarita. ‘Wavelet analysis for single molecule localization microscopy’. *Optics Express* **20** (3) 2012, p. 2081.
- [108] S. Wolter, A. Löschberger, T. Holm, S. Aufmkolk, M.-C. Dabauvalle, S. van de Linde and M. Sauer. ‘rapidSTORM: accurate, fast open-source software for localization microscopy’. *Nature Methods* **9** (11) 2012, pp. 1040–1041.
- [109] M. Ovesný, P. Křížek, J. Borkovec, Z. Švindrych and G. M. Hagen. ‘ThunderSTORM: a comprehensive ImageJ plug-in for PALM and STORM data analysis and super-resolution imaging’. *Bioinformatics* **30** (16) 2014, pp. 2389–2390.

- [110] C. S. Smith, S. Stallinga, K. A. Lidke, B. Rieger and D. Grunwald. 'Probability-based particle detection that enables threshold-free and robust in vivo single-molecule tracking'. *Molecular Biology of the Cell* **26** (22) 2015, pp. 4057–4062.
- [111] R. P. J. Nieuwenhuizen, K. A. Lidke, M. Bates, D. L. Puig, D. Grünwald, S. Stallinga and B. Rieger. 'Measuring image resolution in optical nanoscopy'. *Nature Methods* **10** (6) 2013, pp. 557–562.
- [112] M. Dannemeyer. 'A Detailed Study of Axon Initial Segment Maturation and Structural Organization by Fluorescence Microscopy'. PhD. University Göttingen, 2016. URL: <http://hdl.handle.net/11858/00-1735-0000-0028-86B4-6>.
- [113] K. Weiß, A. Neef, Q. Van, S. Kramer, I. Gregor and J. Enderlein. 'Quantifying the Diffusion of Membrane Proteins and Peptides in Black Lipid Membranes with 2-Focus Fluorescence Correlation Spectroscopy'. *Biophysical journal* **105** 2 2013, pp. 455–462.
- [114] X. Michalet. 'Mean square displacement analysis of single-particle trajectories with localization error: Brownian motion in an isotropic medium'. *Physical Review E* **82** (4) 2010, p. 041914.
- [115] K. Xu, G. Zhong and X. Zhuang. 'Actin, Spectrin, and Associated Proteins Form a Periodic Cytoskeletal Structure in Axons'. *Science* **339** (6118) 2012, pp. 452–456.
- [116] I. Sbalzarini and P. Koumoutsakos. 'Feature point tracking and trajectory analysis for video imaging in cell biology'. *Journal of Structural Biology* **151** (2) 2005, pp. 182–195.
- [117] S. Ghosh, A. M. Chizhik, N. Karedla, M. O. Dekaliuk, I. Gregor, H. Schuhmann, M. Seibt, K. Bodensiek, I. A. T. Schaap, O. Schulz, A. P. Demchenko, J. Enderlein and A. I. Chizhik. 'Photoluminescence of Carbon Nanodots: Dipole Emission Centers and Electron-Phonon Coupling'. *Nano Letters* **14** (10) 2014, pp. 5656–5661.
- [118] T. Dertinger, R. Colyer, G. Iyer, S. Weiss and J. Enderlein. 'Fast, background-free, 3D super-resolution optical fluctuation imaging (SOFI)'. *Proceedings of the National Academy of Sciences* **106** (52) 2009, pp. 22287–22292.
- [119] K. T. Shimizu, R. G. Neuhauser, C. A. Leatherdale, S. A. Empedocles, W. K. Woo and M. G. Bawendi. 'Blinking statistics in single semiconductor nanocrystal quantum dots'. *Physical Review B* **63** (20) 2001.
- [120] L. Eichinger, J. A. Pachebat, G. Glöckner, M.-A. Rajandream, R. Sucgang et al. 'The genome of the social amoeba *Dictyostelium discoideum*'. *Nature* **435** (7038) 2005, pp. 43–57.



- 
- [121] J. Kim, J. Borleis and P. Devreotes. 'Switching of Chemoattractant Receptors Programs Development and Morphogenesis in Dictyostelium: Receptor Subtypes Activate Common Responses at Different Agonist Concentrations'. *Developmental Biology* **197** (1) 1998, pp. 117–128.
- [122] P. J. Slator, C. W. Cairo and N. J. Burroughs. 'Detection of Diffusion Heterogeneity in Single Particle Tracking Trajectories Using a Hidden Markov Model with Measurement Noise Propagation'. *PLoS ONE* **10** (10) 2015, e0140759.
- [123] F. Persson, M. Lindén, C. Unoson and J. Elf. 'Extracting intracellular diffusive states and transition rates from single-molecule tracking data'. *Nature Methods* **10** (3) 2013, pp. 265–269.
- [124] A. Kortholt, I. Keizer-Gunnink, R. Kataria and P. J. M. V. Haastert. 'Ras activation and symmetry breaking during Dictyostelium chemotaxis'. *Journal of Cell Science* **126** (19) 2013, pp. 4502–4513.
- [125] K. Plak, I. Keizer-Gunnink, P. J. M. van Haastert and A. Kortholt. 'Rap1-dependent pathways coordinate cytokinesis in Dictyostelium'. *Molecular Biology of the Cell* **25** (25) 2014, pp. 4195–4204.
- [126] A. Kortholt, R. Kataria, I. Keizer-Gunnink, W. N. V. Egmond, A. Khanna and P. J. M. V. Haastert. 'Dictyostelium chemotaxis: essential Ras activation and accessory signalling pathways for amplification'. *EMBO reports* **12** (12) 2011, pp. 1273–1279.



# Acknowledgements

First, I want to thank Jörg Enderlein for... well, hiring me and giving me the chance to work on this project, obviously. But more than that, coming up with all these fascinating ideas while at the same time letting me and his other students have large freedom in how to pursue their projects, and not forcing his own mindset on others. This attitude created a relaxing and trusting working environment which I will fondly remember.

I would like to thank Claudia Steinem for all the insights and helpful advice given during the thesis committees and her group for all their support towards making the bilayer experiments happen. I am especially grateful to Jutta Gerber-Nolte, Ingo Mey, Ole Schütte, Martin Gleisner, and Jan Kuhlmann for teaching me the ropes of SUV and GUV synthesis and donating some of their precious Avanti lipids from time to time. I was very fortunate to have the SFB 803 watching my back during the last three years – it was a rewarding experience to work with all of you!

I am indebted to the many collaborators who made my experiments possible or lent their expensive equipment: I am grateful to Andrey Klymchenko for the squaraine dye he kindly gifted to me as well as Prof. Vana's group for letting me use their DLS setup. My thanks go out to Christoph Blum, Marco Tarantola, and his group for the hard work they poured into the Dictyostelium experiments. Last but not least, I would like to thank Alexey Chizhik for preparing the gold-coated coverslips.

My sincere thanks go out to the staff of the DPI and the SFB without whom I could not have gotten any work done. In particular, I would like to express my gratitude to Sabine Huhnold & Elke Zech, Nicole Rehbein & Ursula Hahn-Wörgötter as well as Dana Sachs for organising everything from conference travels to buying expensive microscope equipment and keeping the bureaucracy in check, Thomas Geiling for the speedy IT support, Stefanie Kramer & Anna Chizhik for keeping the chem lab running, and Karl Lautscham, Markus Schönekeß & Dieter Hille for their wonderful workshop contraptions.

Furthermore, I would like to thank all of my colleagues for their support. Special mention goes to Daja Ruhlandt, Narain Karedla, and Olaf Schulz for all their advice, encouragement, and continued friendship. Whether you picked me off the coffee room

table in the morning, spent the whole day agonising over how to properly optimise the microscope setup, or tried to shatter my eardrums with your irresistible laughter, I could always count on you. I also want to thank my ex-office mate Sebastian Isbaner (sorry for leaving you!) and new office neighbour Steffen Mühle for proof-reading the thesis in addition to Ingo Gregor for his patient answers to microscopy- and chemistry-related questions. Of course, I cannot move on without mentioning the incredible members of the coffee break society and the (presumably) positive effect our conversations had on my mental health. Thanks, guys and gals!

My undying gratitude goes out to Simon Christoph Stein. You have been a best friend, colleague, co-author, office mate, comrade in arms (albeit virtual ones), lost brother, and surrogate husband/wife. I will never know if I could have done it without you, but even if I did, it would certainly have been a hell of a lot less funny and carefree.

Zum Schluss noch ein liebes Dankeschön an meine Eltern Lena und Klaus und meine Schwester Hanne für die Gelegenheit, dieses Studium überhaupt unternehmen zu können und die vielen aufmunternden wie beruhigenden Worte in schwierigeren Zeiten. Danke, dass ihr mit stets ein Dach über dem Kopf bietet, in mehr als nur einer Hinsicht.

# Curriculum vitæ

## Jan Thiart

Date of birth: 19.12.1987  
Place of birth: Mettingen  
Nationality: German

## Academical Background

10.2008 – 08.2011	Bachelor of Science in Physics Thesis: <i>Optical-trap-based single-molecule assays of Kinesin-5 motor proteins</i> Georg-August-Universität, Göttingen
10.2011 – 10.2013	Master of Science <i>with distinction</i> in Physics Thesis: <i>Diffusion Coefficient Analysis with Single-Molecule Particle Tracking</i> Georg-August-Universität, Göttingen
01.2014 – present	Doctoral dissertation Thesis: <i>Probing Lipid Diffusion in Curved &amp; Planar Membranes with Fluorescence Microscopy</i> Georg-August-Universität, Göttingen

## Awards & stipends

2008 – 2013	Scholarship of the Studienstiftung des deutschen Volkes
2014	“Dr. Berliner – Dr. Ungewitter” award for excellent Master’s thesis

## Conferences

- |      |        |  |
|------|--------|--|
| 2014 | Poster | PicoQuant 20th International Workshop on Single Molecule Spectroscopy and Ultrasensitive Analysis in the Life Sciences, Berlin |
| 2016 | Talk   | Biophysics by the Sea 2016, Alcudia  |
|      | Talk   | International Symposium 2016 “Biological Dynamics from Microscopic to Mesoscopic Scales”, Grimma                               |

## Publications

- |      |  |
|------|--|
| 2016 | F. Savić, T.-T. Kliesch, S. Verbeek, C. Bao, J. Thiart, A. Kros, B. Geil and A. Janshoff. ‘Geometry of the Contact Zone between Fused Membrane-Coated Beads Mimicking Cell-Cell Fusion’. <i>Biophysical Journal</i> <b>110</b> (10), pp. 2216–2228 |
|      | S.C. Stein and J. Thiart. ‘TrackNTrace: A simple and extendable open-source framework for developing single-molecule localization and tracking algorithms’. <i>Scientific Reports</i> <b>6</b> (1).  |